

# Exploring the Mechanisms of 3D Direct Laser Writing by Multi-Photon Polymerization

Jonathan B. Müller

2015  
Dissertation







# Exploring the Mechanisms of Three-Dimensional Direct Laser Writing by Multi-Photon Polymerization

Zur Erlangung des akademischen Grades eines  
DOKTORS DER NATURWISSENSCHAFTEN

von der Fakultät für Physik des  
Karlsruher Instituts für Technologie (KIT)  
genehmigte

DISSERTATION

von

Dipl.-Phys. Jonathan Benedikt Müller  
geboren in Ravensburg

Tag der mündlichen Prüfung:	22. Mai 2015
Referent:	Prof. Dr. Martin Wegener
Korreferent:	Prof. Dr. Christopher Barner-Kowollik



# Contents

<b>Publications</b>	<b>3</b>
<b>Abbreviations and Symbols</b>	<b>5</b>
<b>1 Introduction</b>	<b>9</b>
<b>2 Direct Laser Writing (DLW)</b>	<b>13</b>
2.1 Experimental Setups . . . . .	13
2.2 Photo-Resists . . . . .	16
2.3 Super-Resolution DLW . . . . .	18
<b>3 Fundamentals</b>	<b>21</b>
3.1 Initiation through Multi-Photon Absorption . . . . .	21
3.1.1 Two-Photon Absorption . . . . .	22
3.1.2 Multi-Photon Ionization . . . . .	24
3.1.3 Radical Formation . . . . .	26
3.2 Photo-Polymerization . . . . .	29
3.2.1 Chain Growth . . . . .	30
3.2.2 Cross-Linking . . . . .	31
3.2.3 Reaction Kinetics and Temperature Dependence . . . . .	32
3.2.4 Oxygen Quenching . . . . .	34
3.3 Reaction Conditions . . . . .	35
3.3.1 Threshold Formation . . . . .	35
3.3.2 Local Confinement . . . . .	37
3.3.3 Monomer Conversion . . . . .	41
3.3.4 Heat Conduction . . . . .	44
3.3.5 Molecular Diffusion . . . . .	48
3.3.6 Post-Polymerization . . . . .	50
<b>4 In-situ Analysis Techniques</b>	<b>51</b>
4.1 Local Thermo-Probing . . . . .	52
4.1.1 Local Thermo-Probing with Fluorescent Photo-Resists . . . . .	58
4.2 Optical Polymerization Detection . . . . .	61

<b>5</b>	<b>Initiation Mechanisms</b>	<b>67</b>
5.1	Absorption Mechanisms . . . . .	67
5.1.1	... for Polymerization . . . . .	70
5.1.2	... for Overexposure . . . . .	73
5.1.3	Influence on the DLW Process . . . . .	75
5.2	Local Heating . . . . .	79
5.2.1	Local Heating of Fluorescent Photo-Resists . . . . .	84
5.3	Radical Generation . . . . .	87
5.3.1	Intermediate State Fluorescence . . . . .	88
5.3.2	Charge Transfer with Co-initiators . . . . .	89
<b>6</b>	<b>Polymerization Mechanisms</b>	<b>93</b>
6.1	Termination Reactions . . . . .	94
6.1.1	Quenching by Oxygen . . . . .	94
6.1.2	Quenching by Photo-Resist Additives . . . . .	101
6.2	Duration of the Polymerization Reaction . . . . .	103
6.2.1	Polymerization Regimes for Different Exposure Periods . . . . .	104
6.2.2	Comparison of Different Photo-Resist Compositions . . . . .	109
6.3	Numerical Modeling of the Reaction Kinetics . . . . .	114
<b>7</b>	<b>Parameter Studies Revisited</b>	<b>121</b>
7.1	Photo-Initiator Concentration . . . . .	122
7.2	Writing Velocity . . . . .	124
7.2.1	Proximity Effects . . . . .	125
7.3	Sample Temperature . . . . .	128
<b>8</b>	<b>Conclusions</b>	<b>133</b>
	<b>Bibliography</b>	<b>139</b>
	<b>Acknowledgments</b>	<b>153</b>



# Publications

## Book Chapter

Parts of this manuscript will be published as a chapter in a scientific textbook:

- J. B. Mueller, J. Fischer, and M. Wegener, *Reaction Mechanisms and In-situ Process Diagnostics*, in *Three-Dimensional Micro-Fabrication using Two-Photon Polymerization – Fundamentals, Technology, and Applications*, edited by T. Baldacchini. Elsevier (2015).

## Scientific Journals

Parts of the content of this thesis were published in peer-reviewed scientific journals:

- J. B. Mueller, J. Fischer, Y. J. Mange, T. Nann, and M. Wegener, *In-situ Local Temperature Measurement During Three-dimensional Direct Laser Writing*, Appl. Phys. Lett. **103** (12), 123107 (2013).
- J. Fischer, J. B. Mueller, J. Kaschke, T. J. A. Wolf, A.-N. Unterreiner, and M. Wegener, *Three-Dimensional Multi-Photon Direct Laser Writing with Variable Repetition Rate*, Opt. Express **21** (22), 26244 (2013).
- J. B. Mueller, J. Fischer, F. Mayer, M. Kadic, and M. Wegener, *Polymerization Kinetics in Three-Dimensional Direct Laser Writing*, Adv. Mater. **26** (38), 6566 (2014).
- J. Fischer, J. B. Mueller, A. S. Quick, J. Kaschke, C. Barner-Kowollik, and M. Wegener, *Exploring the Mechanisms in STED-Enhanced Direct Laser Writing*, Adv. Opt. Mater. **3** (2), 221 — 232 (2015).

## Talks and Presentations

Parts of the content of this thesis were presented at seminars, conferences and summer schools (own presentations only):

- J. B. Mueller, J. Fischer, Y. J. Mange, T. Nann, and M. Wegener, *Local In-Situ Temperature Measurement for Three-Dimensional Direct Laser Writing*, CLEO 2013, San Francisco, USA (June 2013).
- J. B. Mueller, J. Fischer, and M. Wegener, *In-Situ Measurement of the Intrinsic Polymerization Time During Three-Dimensional Direct Laser Writing*, CLEO 2014, San Jose, USA (June 2014).
- J. B. Mueller, *Identifying Mechanisms in Three-Dimensional Direct Laser Writing*, Institute Seminar at the Institute of Applied Physics, Karlsruhe, Germany (July 2014).
- M. Adams, J. B. Mueller, J. Fischer, and M. Wegener, *On The Influence of Atmospheric Oxygen on 2D and 3D Direct Laser Writing*, SPIE Photonics West 2015, San Francisco, USA (February 2015).

## Other Publications

Scientific publications of the author without direct relation to the content of this thesis:

- J.C. Halimeh, T. Ergin, J. Mueller, N. Stenger, and M. Wegener, *Photo-realistic Images of Carpet Cloaks*, Opt. Express **17** (22), 19328-19336 (2009).
- J. Müller, T. Ergin, N. Stenger, and M. Wegener, *IM BRENNPUNKT-Doppelt oder gar nicht sehen*, Physik Journal **10** (3), 16 (2011).
- J. Mueller and M. Wegener, *Polarizing Beam Splitter: A New Approach Based on Transformation Optics*, Summerschool: Nano-Optics for Enhancing Light-Matter Interactions on a Molecular Scale, Erice, Italy (July 2011).
- A. Wickberg, J.B. Mueller, Y.J. Mange, J. Fischer, T. Nann, and M. Wegener, *3D Micro-Printing of Temperature Sensors Based on Up-Conversion Luminescence*, Appl. Phys. Lett. **106** (13), 133103 (2015).

# Frequently Used Abbreviations and Symbols

## Chemical Substances

<b>photo-initiators</b>	DETC	7-Diethylamino-3-thenoylcoumarin
	Irgacure 369	2-Benzyl-2-dimethylamino-1-(4-morpholinophenyl)-butanone
	Irgacure 819	Bis(2,4,6-trimethylbenzoyl)-phenyl phosphine oxide
	ITX	Isopropyl thioxanthone
	TPO	Diphenyl(2,4,6-trimethylbenzoyl) phosphine oxide
<b>monomers</b>	PETA	Pentaerythritol triaacrylate
	PETTA	Pentaerythritol tetraacrylate
	DPEPA	Dipentaerythritol pentaacrylate
	TMPTA	Trimethylolpropane triacrylate
	TMPTMA	Trimethylolpropane trimethacrylate
	PEG-DA	Poly(ethylene glycol) diacrylate
	BA	Butyl acrylate
<b>photo-resist additives</b>	HQ	Hydroquinone
	MDEA	N-methyl diethanolamine
	MEHQ	Monomethyl ether hydroquinone
	NNDMA	N,N-dimethylaniline
	NPG	N-phenylglycine
	PTZ	Phenothiazine
	TEMPO	(2,2,6,6-Tetramethylpiperidin-1-yl) oxidanyl
	TED	Tetraethylthiuramdisulfid

## Symbols

<b>physical quantities</b>	$\sigma$	absorption cross-section
	$k_B$	Boltzmann constant
	$[X]$	concentration of species X
	$I$	light intensity
	$\lambda$	light wavelength
	$\hbar\omega$	photon energy
	$\Phi$	photon flux
	$n$	refractive index
	$T$	temperature
	$t$	time
<b>experimental parameters</b>	$t_{\text{exp}}$	exposure period
	$A_{\text{focus}}$	focus area
	NA	numerical aperture
	$t_p$	pulse duration
	$E_p$	pulse energy
	$R$	repetition rate
	$P$	power (for pulsed lasers: time-averaged)
	$d_{\text{voxel}}$	voxel diameter
	$v$	writing velocity
<b>empirical reaction parameters</b>	$N$	absorption nonlinearity
	$\tau_c$	cooling time constant
	$\tau_d$	diffusion time constant
	$\tau_{p, \text{intrinsic}}$	intrinsic polymerization duration
	$\tau_X$	lifetime of the intermediate state X
	$k$	reaction rate
	$P_{\text{th}}$	writing threshold laser power

## Abbreviations

1PA	one-photon absorbtion
2PA	two-photon absorbtion
3D	three-dimensional
AOM	acousto-optic modulator
cw	continuous wave
DLW	direct laser writing
ESA	excited state absorption
FWHM	full width at half maximum
FRET	Förster resonant energy transfer
ISC	inter-system crossing
MPI	multi-photon ionization
ppm	parts per million
STED	stimulated-emission depletion
$S_n$	$n$ -th singlet state
$T_n$	$n$ -th triplet state
TPP	two-photon polymerization
UCNP	up-converting nano-particle
UV	ultra-violett



# 1 Chapter 1

---

## Introduction

During the last decade, the technology for three-dimensional (3D) printing made huge steps towards its real world applicability. Various technological approaches passed the hurdle to the stage of commercially available printing systems, and hence, the idea of “creating arbitrary objects from scratch” inspired not only engineers, but also journalists and the public. While in industry, 3D printing is mostly seen as a cost-efficient and rapid technique for prototyping, the hype in the media was rather focused on the idea of the “materialization of thoughts” in a science fiction-like manner. For example, great interest was attained to a US-student printing a (yet very simple) gun,<sup>1</sup> which was satirically overdrawn in a German blog by sketching the philosophically impressive idea of a US-student printing a “self-reproducing 3D printer”.<sup>2</sup>

While most common 3D printing techniques offer a minimal resolution in the millimeter regime, this thesis deals with a technique mostly referred to as “Direct Laser Writing” (DLW) or “Two-Photon Polymerization” (TPP). So far, it is the only technological approach that offers resolutions down to the few-hundred nanometer range. At the same time, overall sizes of the printed structures can be as large as several millimeters in all three dimensions. In analogy to standard 2D printing, where the common term “pixel” indicates a 2D picture element, the term “voxel” is introduced in DLW for the smallest printable volume element in 3D. In that sense, as the overall structure size is 4 orders of magnitude larger than the resolution in all each three dimensions

---

<sup>1</sup> Meet The “Liberator”: Test-Firing The World’s First Fully 3D-Printed Gun.  
<http://www.forbes.com/sites/andygreenberg/2013/05/05/meet-the-liberator-test-firing-the-worlds-first-fully-3d-printed-gun/>, May 5, 2013, retrieved on January 13, 2015.

<sup>2</sup> US-Student druckt erstmals 3D-Drucker mit 3D-Drucker nach.  
<http://www.der-postillon.com/2013/05/us-student-druckt-erstmal-3d-drucker.html>, May 10, 2013, retrieved on January 13, 2015.

for DLW, one may talk about a Teravoxel technology. The method was first published in 1997 [1], and since then has been applied in various contexts in fields such as photonic crystals, integrated optics, microfluidics, bio-physics and micro-mechanics [2–9]. Since 2007, DLW printing systems are commercially available,<sup>3</sup> and hence, the number of users in academia has rapidly increased ever since. In addition, new applications in industry come into range these days as the writing speed could be increased tremendously by the introduction of a commercial system with galvanometric scanning mirrors in 2014 [10]. The high resolution of DLW is achieved by tightly focusing a femtosecond-pulsed writing laser into a liquid photo-resist. Exposure to these short, but very intense laser pulses leads to a (local) solidification of the previously liquid photo-resist by two-photon excitation and radical polymerization [1]. By moving the sample with respect to the laser spot, almost arbitrarily shaped structures can be fabricated. At the same time, the writing resolution is solely determined by the optical diffraction limit and, hence, comparable to the writing wavelength. While this thesis mainly deals with the reaction mechanisms of standard DLW, the project historically evolved from the research in our group on so-called super-resolution DLW approaches, which offer structuring resolutions below the optical diffraction limit [11, 12]. This technique is based on a similar approach as Stimulated Emission Depletion (STED) microscopy [13, 14], which was awarded with the 2014 Nobel price in Chemistry. However, it turns out that even for these super-resolution approaches, the DLW resolution is still limited – most likely not by optics, however, but by the photo-chemistry of the polymerization reaction.

Despite the enormous number of publications on the improvement of its resolution as well as possible applications, the DLW process itself absconded from a more quantitative description for a long time, and hence, also the origin of this supposedly photo-chemical resolution limit remained unclear. The main reason for this is the fact that the reaction conditions are very specific. Namely, the reaction does not occur continuously in macroscopic volumes (e.g., in a beaker glass), but it is induced by a short intense exposure in a small reaction volume only, which is surrounded by non-reacting photo-resist. Therefore, the influence of different chemical and physical mechanisms on the overall process, such as quenching by inhibiting chemical species or molecular diffusion, is different than one might expect at first sight. At the same time, due to the small structure size and the little amount of polymerized material, most analysis tools known, e.g., from polymer chemistry, are not applicable. For this reason,

---

<sup>3</sup> *Photonic Professional* series (Nanoscribe GmbH).



---

we performed a series of experiments in order to bring more light into this issue. These experiments and their results with regard to (mostly standard) DLW are described and discussed in this thesis.<sup>4</sup> Still keeping the discussion very general, such experiments can be distinguished into three different classes:

1. Variation of the exposure conditions (e.g., laser power, pulse repetition rate, laser wavelength, writing velocity, etc.).
2. Variation of the photo-resist composition (e.g., by changing photo-initiators, monomers, inhibitors, co-initiators, and the oxygen content).
3. In-situ process diagnostics (e.g., by optical spectroscopy).

The first two classes require full processing of the sample, including characterization by optical microscopy, or, in most cases, scanning electron microscopy. In these cases, certain figures of merit (e.g., writing threshold laser power or achievable line width and/or resolution) are introduced and investigated while varying the writing conditions. Conclusions can then be drawn by a comparison of the observed behavior to the expectations according to an analytical or numerical model. However, in many cases, any change in the writing parameters will influence several partial reactions and processes at the same time. For example, a change of the monomer species will also affect the optical properties of the photo-initiator as these properties are solvent-dependent. Therefore, the experiments from the first two classes are indirect in some sense and do not always yield clear, easy-to-interpret results. The methods of the third class, i.e., in-situ diagnosis techniques, offer a more direct access to the microscopic mechanisms as intermediate reaction stages can be accessed instead of the final result. During the work on this thesis, two new in-situ analysis techniques were developed by adapting approaches from literature, which aim at the measurement of the progress of the polymerization reaction and the detection of the local heating in the focal volume, respectively.

While the ultimate goal of this thesis – the overcoming of the resolution limitations for super-resolution DLW – could not be achieved, the applied methods still lead to a substantially deepened understanding of the DLW process in general as well as of possible limitations for super-resolution approaches.

---

<sup>4</sup> In order to give a complete overview over the current stage of this research topic, experiments which were primarily conducted by J. Fischer and F. Mayer are included into this manuscript as well. This is indicated in the sections where relevant. The experiments of F. Mayer were performed during and after his Bachelor thesis project, and were directly supervised by the author of this thesis. Where relevant, original sources are indicated.

## Outline

A short introduction to the DLW technique is given in **Chapter 2**. It includes a description of typical as well as of the actually used experimental schemes and photo-resists for direct laser writing. **Chapter 3** represents a resume of the fundamentals of DLW, organized in two theory sections that briefly recapitulate the relevant literature knowledge on the initiation through multi-photon absorption and on photo-polymerization. In a last section, the specific reaction conditions for DLW will be reviewed, including a simple model for 3D structuring as well as a discussion on temporal and non-local effects, which may (or may not) lead to deviations from that simple model.

In **Chapter 4**, the two newly developed spectroscopy techniques for measuring the local temperature change during the writing process and the progress of the polymerization reaction will be discussed. As these experiments are conceptually different from existing setups, the design of the experimental setting, the data processing and the interpretation of the results will be reviewed in detail. These considerations are separated from the experimental results concerning the mechanisms of DLW in order to keep the discussion of the latter as brief and clear as possible.

Representing the main part of this work, these experimental results will be presented in **Chapter 5** and **Chapter 6**, for experiments with a focus on the nature and the properties of both the initiation and the propagation of the photo-polymerization reaction, respectively. While the variation of the repetition rate and the detection of the local heating offer insights into the reaction pathways for standard DLW, a part of the presented experiments is specifically devoted to the mechanisms in the special case of STED-DLW. In Chapter 6, the reaction pathway of the actual polymerization is discussed. This includes the presumably most important finding of this work, namely the influence of oxygen and oxygen quenching on the writing process.

The overall discussion will be completed by a collection of effects that surprised or annoyed many DLW users in the past, such as the dependency of the writing threshold on the writing velocity or the sample temperature or line-start effects in **Chapter 7**. While these effects could not be explained by the simple threshold model discussed in Chapter 3, their origin becomes more clear after considering the results of Chapter 6.

To conclude, the presented results will be wrapped-up in **Chapter 8** by giving an overview of all relevant (and known) time scales of the different processes and a discussion thereof.

# 2

## Chapter 2

---

# Direct Laser Writing (DLW)

Before discussing the fundamentals of DLW in the following Chapter, the experimental settings which are underlying the experiments in this thesis will be presented and discussed. Thereby, the term “Direct Laser Writing” will be defined more precisely. At the same time, this chapter targets the clarification the scope of the presented results and their interpretations. After a description of the experimental setups which are used, an overview of the investigated photo-resists is given. In addition, the concept of super-resolution DLW is introduced very briefly as this approach will be referred to at various points throughout this thesis.

## 2.1 Experimental Setups

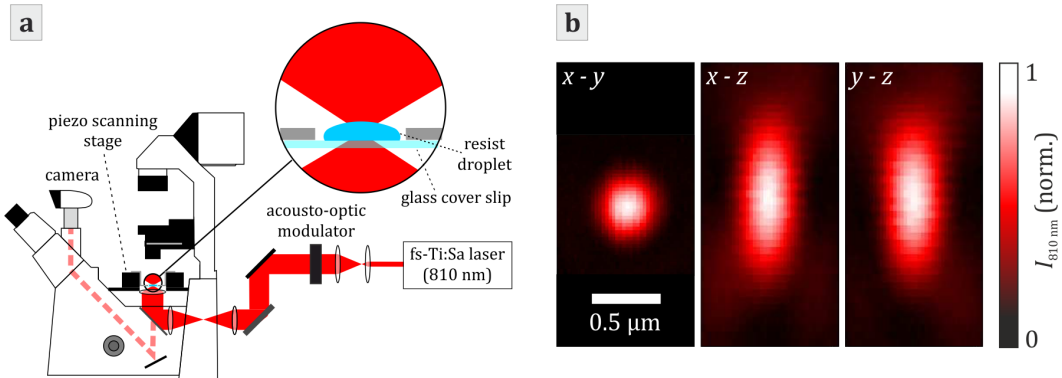
Many DLW systems are based on one very popular scheme (within this manuscript referred to as the “reference scheme”), which has been proven to yield excellent results in terms of structural quality and reproducibility. Namely, a high-repetition-rate fs-pulsed laser (e.g., 100 fs pulse duration at a rate of 80 MHz with approximately 800 nm center wavelength) is used under tight focusing conditions to expose a liquid photo-resist based on multifunctional acrylates. In addition to these core features, the practical usability is improved by several add-ons, which are considered of no importance with respect to the occurring reaction mechanisms. For example, the writing process can be observed directly by a microscope camera (requiring also a sample illumination) and an interface finder unit automatically detects the interface of substrate and photo-resist. Furthermore, a motorized coarse stage allows to displace the sample by more than the traveling distance of the high-precision piezo-electric stage which is used for the writing process itself (here: 100  $\mu\text{m}$  - 300  $\mu\text{m}$ ). The

whole setup is highly automatized to yield high reproducibility and throughput. A more detailed description of these features for the two setups can be found elsewhere ([15] and [16], respectively).

This reference scheme is relatively well investigated and the basis for both setups used within this thesis, which are referred to by the corresponding writing lasers. If not explicitly mentioned in the corresponding section, they are used in their standard configuration which is shortly described in this section.<sup>1</sup> Furthermore, the discussed reference scheme is largely similar to commercially available 3D-DLW systems (*Photonic Professional* series, *Nanoscribe*). As the Nanoscribe-System is often referenced within this thesis, it will also be briefly mentioned.

### MaiTai-Setup

For this setup, which is based on a commercial microscope corpus, the writing laser is a *MaiTai HP* Ti:sapphire oscillator (*Spectra Physics*) tuned to 810 nm center wavelength. The MaiTai-Setup is depicted in **Figure 2.1**.



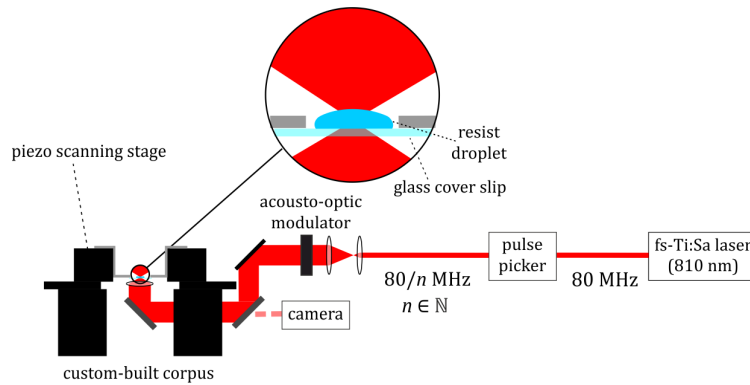
**Figure 2.1:** a) MaiTai-Setup.<sup>2</sup> The high-repetition-rate fs-pulsed Ti:sapphire oscillator is focused into the sample by a high numerical aperture objective lens through the corpus of a commercial microscope. The sample can be moved with respect to the laser focus by a piezo-electrical positioning stage in order to write 3D structures. b) Measured intensity distribution of the writing laser using the gold bead scanning technique.

<sup>1</sup> Both setups were originally designed and built by J. Fischer, partly with the help of J. Kaschke and the author. In order to perform the experiments described in this thesis, they were continuously adapted, improved and extended by the author.

<sup>1</sup> Graphics kindly provided by J. Fischer.

### Chameleon-Setup

For the Chameleon-Setup, the microscope corpus is replaced by a fully home-built setup in order to provide better mechanical stability. The writing laser (*Chameleon Ultra II, Coherent*) is tuned to 800 nm instead of 810 nm for practical reasons. In order to decrease the repetition rate if desired, a pulse picker (*Pulse Select HP-Ti:Sa, APE Berlin*) is used. The experimental setting is displayed in **Figure 2.2**.



**Figure 2.2:** Schematic drawing of the Chameleon Setup with a commercial pulse-picker in order to reduce the pulse repetition rate of the writing laser. As single pulses from the writing laser can be suppressed, divisors of 80 MHz can be set as repetition rates with typical pulse energies in the nJ-regime. The inverted microscope corpus is replaced by a custom-built platform in order to provide a mechanically more stable environment.

### Nanoscribe-System

In contrast to the two setups mentioned above, the commercial *Nanoscribe Photonics Professional* works with a frequency-doubled Erbium-doped fiber laser with a center wavelength of 780 nm and a similar specified pulse duration of less than 100 fs at a repetition rate of 80 MHz. As this is relatively close to the key features of the above-mentioned Ti:sapphire laser systems, we believe that results obtained on the basis of the home-built setups can largely be translated to experiments performed on these commercial systems.

### Focusing Conditions

For high resolution DLW, it is most favorable to use objective lenses with high numerical aperture  $NA = n \sin \alpha$ , with the refractive index of the immersion medium  $n$  and the half opening angle  $\alpha$ . Unless noted otherwise, all objective lenses used within this thesis are 100x oil immersion lenses with  $NA = 1.4$ , corresponding to a half opening angle of around  $70^\circ$ . The corresponding intensity distribution in the focus then has a lateral size of around 330 nm (full width at half maximum, FWHM) and an axial size of around 800 nm (FWHM) at the writing wavelength (800 nm) and can be characterized and optimized by scanning individual 100 nm-diameter gold beads through the focus while detecting the backscattered light (**Figure 2.1 b**) [15].

For typical writing laser powers of approximately 5 mW (corresponding to pulse energies of 0.05 nJ) at high pulse repetition rates, the resulting intensities reach  $10^{15} \text{ W/m}^2$  in the focus. At low repetition rates (e.g., 1 kHz with the Chameleon-Setup), these values can be higher by an order of magnitude or more.

## 2.2 Photo-Resists

The photo-resist family which has shown best performance with respect to the achievable writing resolution is based on the free radical polymerization of multifunctional acrylates. According to the naming conventions in the field of lithography, this is a “negative-tone” photo-resist, i.e., exposed volumina are polymerized and will remain as solid structures after the sample development step. A typical formulation consists of the commercially available monomers Pentaerythritol tri- or tetraacrylate (PETA and PETTA, respectively) with approximately 0.2 – 2% (wt.) of photo-initiator added. Experimentally, we found no significant difference between these two monomer species. Like all chemicals throughout this thesis, they were used as received without any further purification. This implies that the used photo-resists still contains 300 – 400 ppm of Mono methyl ether hydroquinone as inhibitor. As discussed in Section 6.1.2, this has no influence on the writing process. At some points of this thesis, the commercial *IP* photo-resists, (*Nanoscribe* GmbH) will be mentioned. These are based on multifunctional acrylates as well and have been developed to fulfill the specific needs of some DLW applications, e.g., by matching the refractive index of the photo-resist to the substrate.

In practice, it turned out that almost any common UV photo-initiator for radical polymerization can be used for DLW and gives reasonable results. Within this thesis, we mostly restrict the discussion to the very popular photo-initiators 2-Benzyl-2-dimethylamino-1-(4-morpholinophenyl)-butanone-1 (Irgacure 369), Bis(2,4,6-trimethylbenzoyl)-phenylphosphineoxide (Irgacure 819), which is a little more efficient, 7-Diethylamino-3-thenoylcoumarin (DETC), and Isopropyl thioxanthone (ITX). A clear emphasis is put on the investigation pathway for DETC-based photo-resists for two reasons: First, we found that the reaction pathway is different and more complex as compared to the commercial standard photo-initiators, and second, DETC and some close relatives are the only photo-initiators known so far that feature stimulated emission depletion as a depletion channel for STED-DLW [17–23] (see next section). While for many photo-initiators, a concentration of around 1% (wt.) is a good starting point to yield good results, only 0.25% (wt.) are used for DETC due to its lower solubility in the monomer compared to the other initiators on the one hand, and its superior efficiency for radical generation on the other hand.

After exposure, the samples must be washed with solvents in order to remove the liquid resist. A typical procedure starts with a 15 minutes immersion in a bath of isopropanol, followed by washing with acetone and de-ionized water and dry-blowing with nitrogen or air.

While all experiments in this thesis refer to the above-mentioned class of acrylate-based photo-resists, a whole variety of other photo-resist systems has been successfully used for 3D-DLW as well. These include other negative tone photo-resists systems, which are based on free radical polymerization as well, such as anorganic-organic hybrid photo-resists (*Ormocore, micro resist technology* GmbH) [24], Zirconium–silicon based sol–gel photopolymers [25], polymerization reactions based on Thiol-ene chemistry [26], and the fabrication of Poly(dimethylsiloxane) elastomers [27].

However, other reaction mechanisms for negative tone photo-resists have been investigated in combination with DLW as well. E.g., the photo-polymerization reaction of the commercial photo-resist *SU-8 (MicroChem)* is initiated by the photoactivation of a photoacid generator which starts a cationic chain growth mechanism [28]. Furthermore, positive tone resists have been used, where an Indene carboxylic acid is formed during exposure so that they become soluble in aqueous alkaline solutions (*AZ 9260, MicroChemicals GmbH*) [29]. Also, it has been shown that metal structures can be written directly through multi-photon-induced metal-ion reduction [30].

Obviously, not all of the results from this thesis can be directly transferred to these and other lithography schemes. Even for the acrylate based resists, the direct transfer of the claimed mechanisms within this thesis requires some precaution if other writing laser systems are being used which differ substantially from the standard scheme in terms of the repetition rate, the pulse duration or the laser wavelength (e.g., [31,32], [33], and [8,34–43]). However, the aim of this manuscript is to give the reader an idea on how essential process mechanisms could be discriminated in these cases as well.

### 2.3 Super-Resolution DLW

While this thesis targets the investigation of standard DLW, special attention is given to the DLW mechanisms for such photo-resist systems that can also be used for STED-DLW. Therefore, a brief introduction to the working principle of STED in microscopy and also in lithography is given in this section. Originally, the concept of the optical resolution limit [44, 45] as well as the ways to overcome it have been discussed in the context of microscopy [13, 46–48]. While some of these approaches are based on the detection of single fluorophores at a time and, hence, not readily transferable to DLW, the concept of STED-enhanced laser scanning microscopy can in principle be taken over from microscopy, where it allows for resolutions down to a few nanometers [49]. This is clearly beyond the above-mentioned diffraction limit (Section 3.3.2), which states that the resolution is always roughly equal to the illumination light wavelength in the immersion medium.

In order to profit from the STED resolution enhancement in microscopy, a second depletion laser beam with a different wavelength and a different mode profile de-excites the fluorophores in the outer region of the voxel by stimulated emission. Therefore, the beam profile of the depletion laser must be chosen such that it provides a local minimum with zero intensity at the maximum position of the excitation laser. Depending on whether the resolution improvement should be effective in 2D or 3D, typically either a doughnut-shaped focus or a so-called “bottle-beam” focus is chosen. The latter does not only provide a minimum in lateral direction, but it also possesses two maxima along the beam axis, so that the effective resolution can be improved in axial direction as well. As the molecules in regions with effective depletion will not contribute to the image, the resulting resolution is improved.



In an ideal case, the depletion laser is used at very high intensity, so that the depletion effect saturates everywhere except for the intensity zero spot in the center of the depletion focus and, hence, the detection region corresponding to one pixel can be arbitrarily small. However, a resolution in the few-nanometer regime can only be achieved when efficient and stable (non-bleaching) fluorophores such as vacancy centers in diamond are being used [49].

As a similar improvement would be highly desirable for optical lithography as well, many attempts have been made to adapt this mechanism to laser lithography [17, 21, 50–52]. Even though Abbe’s limit is not applicable here a priori, similar considerations can be made and yield results which are consistent with experiments (Section 3.3.2) [11]. However, these approaches are experimentally challenging as any depletion pathway must not only suppress fluorescence, as in microscopy, but the generation of free radicals. Hence, the suppression is typically not limited by bleaching, but by accidental radical generation through photo-dissociation by the depletion laser. In principle, this can also be achieved by STED, however, other depletion channels triggered by excited state absorption seem to play a role as well [18–23, 51, 53, 54]. A different approach is based on the activation of inhibiting species by a different laser wavelength that prevent the formation of an insoluble cross-linked polymer network [50, 52, 55–57].



# 3

## Chapter 3

---

# Fundamentals

In this chapter, the fundamentals of DLW will be discussed in more detail. Except for the considerations on heat conduction and molecular diffusion (Section 3.3.4 and Section 3.3.5), the chapter is mostly a wrap-up of relevant knowledge from literature with respect to the reference scheme described in the previous chapter. Hence, some parts may be skipped by readers already familiar with DLW.

Typically, the polymerization reaction can be split into two (relatively) independent steps. Namely, starting radicals are formed from the photo-initiator in a first step, followed by the actual polymerization reaction as the second step. Along these lines, this chapter is divided into three parts. First, possible initiation mechanisms for radical photo-polymerization reactions such as they occur during DLW are discussed. In the second section, literature knowledge on the actual polymerization reaction is recapitulated, followed by a discussion of the actual reaction conditions for DLW and possible effects of the locally and temporally confined reaction in the third part.

### 3.1 Initiation through Multi-Photon Absorption

For DLW, a super-linear photo-resist response is required to provide three-dimensional structuring. In most cases, this nonlinear behavior originates from a nonlinear absorption mechanism such as multi-photon absorption. The used laser source and the photo-initiator must then be selected such that the corresponding one-photon absorption coefficients are negligible at the writing wavelength, and multi-photon absorption becomes the dominant absorption pathway. From a different point of view, one may argue that free radicals are formed from the excited photo-initiator molecules by chemical bond breaking,

and hence, as typical bond dissociation energies are in the order of 3 eV or more [58], the energy of at least two infrared photons is required (e.g.,  $\hbar\omega = 1.55$  eV for  $\lambda = 800$  nm). If the energy deposited during the primary multi-photon absorption process is not sufficient for the bond breaking reaction, an additional secondary absorption step (excited state absorption) may be necessary.

A graphical overview of possible reaction pathways for radical generation by multi-photon absorption is given in **Figure 3.1**. In the following sections, the different pathways will be discussed in more detail. The experimental discrimination of these different excitation mechanisms represents a large portion of this thesis and will be discussed in great detail (Section 4.1, Section 5, and Section 5.2).

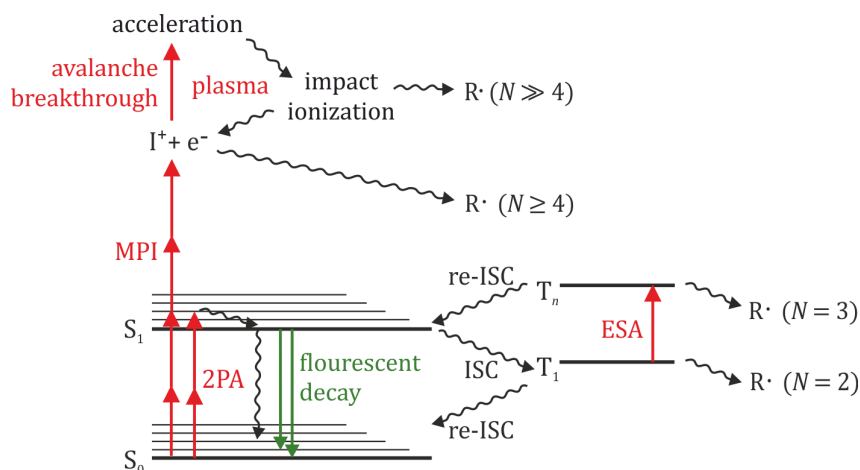
#### 3.1.1 Two-Photon Absorption

According to the “standard model” of direct laser writing, the dominant multi-photon absorption pathway for sensitized photo-resists (i.e., resists including dedicated photo-initiators) is two-photon absorption (2PA) [1]. This mechanism has first been described by Maria Göppert-Mayer in 1931 [59] and is based on the simultaneous absorption of two photons, leading to the direct excitation of a molecule without the existence of an intermediate state. The excitation probability is hence proportional to the squared optical intensity. In contrast, for a “normal” one-photon absorption process (1PA), the excitation probability would be directly proportional to the optical intensity.

In order to see whether two-photon absorption could actually yield a reasonable number of starting radicals, let us consider some simple estimates. The commonly used photo-initiator Irgacure 819 has a peak 2PA cross-section of  $\sigma_{2\text{PA, peak}} = 5$  GM (1 GM =  $10^{-50}$  cm<sup>-4</sup>/s/photon/molecule) [60]. Assuming that the shape of the two-photon absorption spectrum is similar to that of the one-photon absorption spectrum [60] at half the wavelength, we estimate the 2PA cross-section at 800 nm wavelength to be [16]

$$\sigma_{2\text{PA, 800 nm}} = \frac{\sigma_{1\text{PA, 400 nm}}}{\sigma_{1\text{PA, peak}}} \cdot \sigma_{2\text{PA, peak}} = 0.375 \text{ GM.} \quad (3.1)$$

The probability for one photo-initiator molecule to be excited under DLW conditions (i.e., by two-photon absorption) during one laser pulse can then be



**Figure 3.1:** Reaction schemes for different pathways for radical formation by multi-photon absorption. In the standard model based on two-photon absorption (2PA), the photo-initiator molecule is excited by two-photon excitation from the electronic singlet ground state ( $S_0$ ) to the excited singlet manifold ( $S_1$ ). From there, it relaxes to the lowest vibrational  $S_1$  state, undergoes intersystem-crossing (ISC) to the lowest triplet state and from there forms radicals. However, in the case of long-living triplet states (e.g., if the triplet lies lower than the dissociate state or if there is a potential barrier), excited state absorption from the triplet may be necessary to generate radicals. If the two-photon process is unlikely (e.g., no photo-initiator present), multi-photon ionization (MPI) may occur (in this example through the absorption four photons), which is potentially followed by avalanche breakthrough. In both cases, radicals are presumably generated by thermal or non-thermal energy transfer and subsequent molecule dissociation. In addition, parasitic side reactions such as de-excitation by spontaneous photo-emission or non-radiative decay as well as reverse intersystem-crossing (re-ISC) may influence the radical formation [23].

estimated as

$$p_{\text{abs}} = 0.5 t_p \sigma_{2\text{PA}} \Phi^2 = 0.0089\% \quad (3.2)$$

with the photon flux  $\Phi = E_p / (t_p A_{\text{focus}} \hbar\omega)$ , the pulse duration  $t_p = 200$  fs, the excitation pulse energy at the writing threshold  $E_p \approx 0.03$  nJ, the lateral area of the laser focus  $A_{\text{focus}} = \pi (165 \text{ nm})^2$  (assuming a top hat beam profile with the same diameter of 330 nm as the laser focus), and the photon energy  $\hbar\omega$  [16]. Obviously, the resulting probability is much smaller than one and hence, the process is far from the saturation regime. At first glance, it may seem by far too small to lead to radical formation from a substantial fraction of the photo-initiator molecules. However, for a writing velocity of  $v = 100 \mu\text{m/s}$  and at a repetition rate of  $R = 80$  MHz, every molecule is exposed to 264.000 pulses during a typical exposure period of  $t_{\text{exp}} = 3$  ms, resulting in around 23 excitation events in total per molecule (assuming immediate decay back to the ground-state). Hence, for decent radical generation quantum efficiencies in the order of a few percent, a substantial fraction of the photo-initiator molecules generates radicals after the exposure.

#### 3.1.2 Multi-Photon Ionization

Yet another proposed model for radical formation is based on multi-photon ionization (MPI), potentially followed by avalanche ionization due to the high absorptivity of charged particles [31]. Similarly to the electronic two-photon excitation discussed in the previous section, MPI is triggered by a multi-photon absorption event. However, the electron shell is not excited to an excited bound state, but to an unbound state where one (or more) electrons are separated from the molecule. Therefore, also the monomer itself can be photo-ionized, while for an efficient radical generation process through two-photon excitation, photo-initiator molecules with selected optical properties are necessarily required. A photo-initiator is hence not necessarily needed for MPI.

For short pulse durations in the 100 fs-regime, the ionization rate is dominated by the direct MPI [61]. If the applied pulse durations are larger, the latter primarily acts as seeding mechanism for the electron avalanche generation. However, in both cases, we expect this route to require initiation by MPI and, hence, large pulse energies. The generation of radicals may then occur in a non-resonant reaction via photo-thermal dissociation of photo-initiator or monomer molecules. For many organic molecules, typical intensities for this process to be efficient are in the order of  $10^{13} - 10^{14} \text{ W/m}^2$ , corresponding to pulse energies of some nanojoules under typical exposure conditions and for pulse durations in the 100 fs-regime [62]. However, these pulse energies are

larger by two orders of magnitude compared to the pulse energies required for two-photon absorption. Hence, this photo-physical reaction pathway is expected to dominate the overall reaction only if the number of writing laser pulses hitting one voxel is low and, therefore, the required pulse energies are high, or if the photo-chemical pathway is excluded due to the absence of a photo-initiator.

One might also expect that at the relatively high electric field strengths in the case of low repetition rate DLW, the ionization process could better be described as a tunnel ionization rather than by a multi-photon process. In that case, the ionization process could be seen as the quantum-mechanical tunneling of an electron through a potential barrier, induced by the molecular binding potential, in combination with an external, static electric field. It has been argued that this description is largely valid for  $\gamma_K < 0.5$  [63], with  $\gamma_K = \omega \frac{\sqrt{2m_e V}}{eE}$  being the so-called Keldysh parameter with the angular frequency of the incoming wave  $\omega$ , the electron mass  $m_e$ , the electron charge  $e$ , the electric field strength  $E$ , and the ionization potential  $V$  [64]. For the maximum applied pulse energy within this thesis ( $E_p = 4$  nJ, at a pulse duration of 200 fs) and a typical ionization potential of 8 eV (see below), we calculate a Keldysh parameter of  $\gamma_K \approx 2.5$ . For more typical parameters for DLW with high repetition rates and in sensitized resists ( $E_p = 0.03$  nJ), we get  $\gamma_K \approx 30$ . Therefore, the above-mentioned description of the ionization as a multi-photon process seems more appropriate for DLW.

#### Comparison

In order to compare the efficiencies of the processes for different writing schemes, the energy levels of the involved states can be calculated numerically for several molecules contained in the examined photo-resists (**Table 3.1**) [22]. For two-photon absorption, the relevant states are the ground state and the first excited state of the electronic singlet manifold ( $S_0$  and  $S_1$ , respectively). For multi-photon ionization, the excited state corresponds to the lowest ionized state (i.e., obeying one unbound electron). As can be seen, typically 6-7 photons are required for multi-photon ionization. In analogy to Equation (3.2), one can calculate the probability for an excitation event to occur during one laser pulse according to

$$p_{\text{abs}} = 0.5 t_p \sigma_{\text{NPA}} \Phi^N \quad (3.3)$$

for an  $N$ -photon absorption process. While for 2PA, the probability for a molecule to be excited can be estimated as discussed, the correspond-

**Table 3.1:** Calculated transition energies for the  $S_0$ - $S_1$  transition and photo-ionization for a typical photo-initiator and monomer. The corresponding number of near-infrared photons (wavelength 800 nm) is also given for convenience.

	$S_0$ - $S_1$ energy	$S_0$ - $S_1$ photon number	ionization energy	ionization photon number
<b>PETA</b>	4.8 eV	3.1	10.7 eV	6.9
<b>Irgacure 369</b>	3.9 eV	2.5	7.9 eV	5.1
<b>Irgacure 819</b>	3.3 eV	2.1	8.7 eV	5.6
<b>DETC</b>	3.1 eV	2	7.9 eV	5.1

ing cross-sections  $\sigma_{NPA}$  for photo-ionization are largely unknown. For the experimentally determined threshold pulse energy of  $E_p = 1.5$  nJ at a repetition rate of  $R = 100$  kHz [16], we find that a cross-section of  $\sigma_{6PA} \approx 10^{-179} \text{ cm}^{12}\text{s}^{-5}$  leads to one MPI event per photo-initiator molecule, leaving all other parameters as in the 2PA case. This is at least in the order of magnitude one would expect [65]. At the same time, the molecule will be excited only five times through 2PA (compared to 23 excitation events at the writing threshold for  $R = 80$  MHz), indicating that a different mechanism like MPI may indeed be dominating at these low repetition rates.

### 3.1.3 Radical Formation

The initial excitation step for radical generation has been discussed in the last sections. However, in order to yield starting radicals for the second step of the photo-polymerization reaction, namely, the polymerization reaction itself, the photo-initiator has to undergo a photo-cleavage reaction.

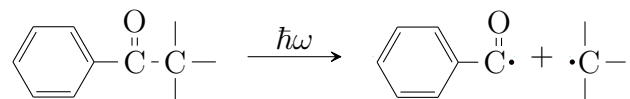
In most cases described in the literature, radical formation is based on UV-excitation, i.e., the photo-initiator molecules are generated in a one-photon absorption process. Here, the subsequent radical generation step is relatively well investigated and will be briefly described in the following. However, it is not very clear at the moment, to which extent this knowledge can be applied to the multi-photon absorption cases. More precisely, while for the (electronic)



two-photon excitation, the photo-initiator is still assumed to be excited to the first singlet state as for 1PA, a different reaction pathway seems more likely in the case of photo-ionization.

### Norrish type I

After the optical excitation of the photo-initiator from its electronic singlet ground state ( $S_0$ ) to the first excited singlet manifold ( $S_1$ ), it relaxes vibrationally to the lowest  $S_1$ -state and from there undergoes inter-system crossing (ISC) to the lowest triplet state ( $T_1$ ). Commercial photo-initiators such as Irgacure 819 and Irgacure 369 are Norrish type I initiators, which means that they undergo a homolytic C-C bond scission from the triplet state (photo-induced  $\alpha$ -cleavage). It has been shown that for this class of molecules, this reaction path is very efficient [66,67]. Many initiators in this class are aromatic carbonyl compounds, which typically generate two radical fragments upon light exposure (**Figure 3.2**). In many cases, a benzoyl radical represents the main initiating species for radical polymerization. However, both generated radicals may participate in the polymerization reaction. Depending on their specific properties, each of them may initiate or terminate the polymerization reaction (Section 3.2.1). Hence, the initiation efficiency of the generated radicals represents an essential property of good photo-initiators.

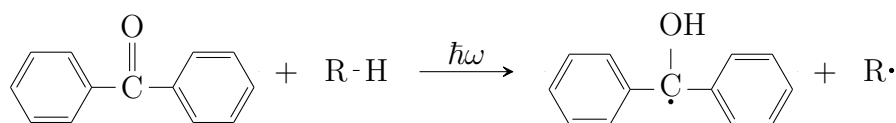


**Figure 3.2:** Radical generation by photo-dissociation for an aromatic carbonyl compound [68].

### Norrish type II

DLW is also possible when using Norrish type II initiators. These typically undergo an hydrogen atom transfer reaction with an additional co-initiator molecule in order to yield radicals. One typical example of this kind is benzophenone (**Figure 3.3**).

The photo-sensitizing molecules of this class which have successfully been used for DLW include DETC and ITX. Interestingly, these are also the photo-initiators for which a resolution improvement could be demonstrated using



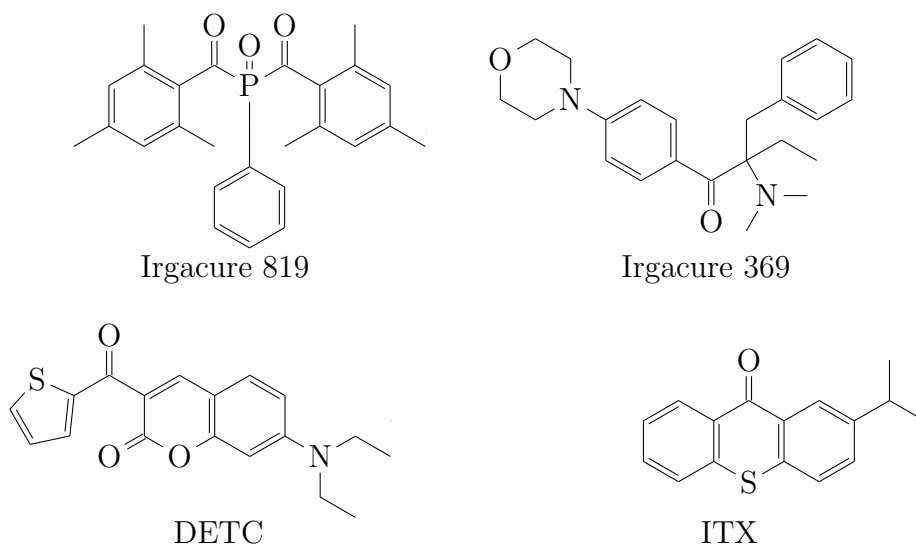
**Figure 3.3:** Radical generation by hydrogen atom transfer with a co-initiator molecule R – H for benzophenone [68].

the STED-DLW approach [17, 53]. As will be discussed in Section 5.3.1 and Section 5.3.2, the experimental results hint that in the absence of a co-initiator, radical generation occurs through an excited state absorption process, leading to an effective third order absorption behavior (Section 5.1). Indeed, it has been shown that both molecules DETC and ITX feature triplet-triplet absorption ( $T_1$ - $T_n$ ) which could – depending on the applied wavelength and thereby the energy level and nature of the excited state  $T_n$  – lead to either radical formation or reverse intersystem-crossing [20]. Please note that within this thesis, these species will be referred to as Norrish type II photo-initiators even when used without a co-initiator, for the reason that the mechanism is different from the commercial Norrish type I photo-initiators as it includes an additional absorption step.

When validating the performance of specific photo-initiators, it is essential to keep in mind that in many cases, radical-radical recombination of generated radical pairs is very likely. Therefore, the overall initiation efficiency is the result of a non-trivial interplay of the probability for a photo-initiator molecule to generate radicals under the specific illumination conditions and the probability for these radicals to either recombine or initiate chain growth. Obviously, the probabilities for these bi-molecular reactions depend on the concentrations of the corresponding reagents. Such radical-radical recombination mechanisms would lead to a reduced initiation efficiency if the radical generation rate is large, which, however, is not observed in the case of DLW as discussed later on (Section 5.1).

In order to allow for a qualitative comparison of the results, most experiments within this thesis have been performed with either of the the four photo-initiators Irgacure 819, Irgacure 369, DETC, and ITX (**Figure 3.4**). However, especially for the class of commercial Norrish type I photo-initiators, several other chemical species have been tested in a non-systematic way during this thesis as well, including Diphenyl(2,4,6-trimethylbenzoyl)phosphine oxid (TPO), 2-(4-Methylbenzyl)-2-dimethylamino-1-(4-morpholinophenyl)-1-butanone (Irgacure 379) and 2,2-Dimethoxy-1,2-diphenyl-1-ethanone (Irgacure 651). All of these

yield similar structuring results, indicating that the mechanistical details of the photo-chemical initiation mechanism (e.g., radical fragments with different initiation efficiencies) do not play a dominant role for the overall structuring quality.



**Figure 3.4:** Structural formula of the commonly used photo-initiators Irgacure 819, Irgacure 369 (both Norrish type I), DETC, and ITX (both Norrish type II). Please note that for DLW, also DETC and ITX are mostly used without an additional co-initiator species, requiring an additional excited state absorption process.

## 3.2 Photo-Polymerization

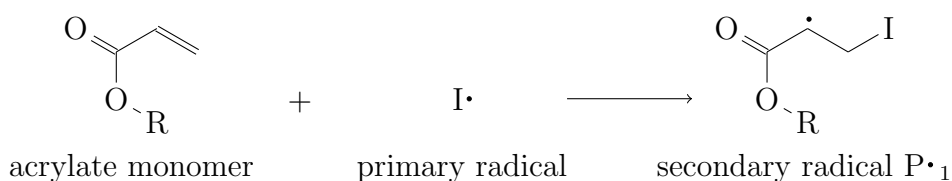
In the second reaction step, the actual solidification of the (previously liquid) photo-resist occurs by polymerization of the monomer. In order to introduce the corresponding terminology, the chemical model of polymerization by chain growth will be briefly introduced in the following section.<sup>1</sup>

<sup>1</sup> Nomenclature and representation are taken and adapted from [68] and [69].

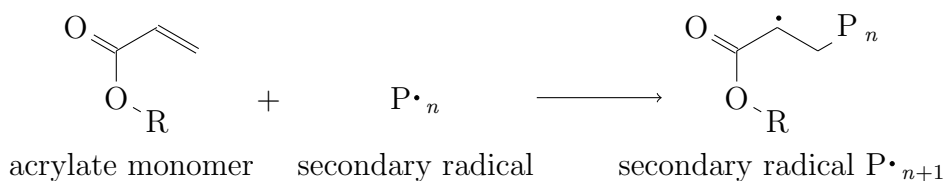
### 3.2.1 Chain Growth

Radical polymerization can be described by a three-step reaction pathway which follows the formation of primary radicals as described in the previous section. In the case of unsaturated acrylates as monomer units (which have been used as monomers throughout this thesis), the corresponding chemical reactions can be depicted as follows:

1. **Chain initiation:** Formation of a secondary chain radical (secondary radical)



2. **Chain propagation:** Addition of monomer units (chain growth)



3. **Chain termination:** Stop of chain growth by

- a) **Radical-radical recombination**



- b) **Disproportionation** (hydrogen atom transfer)



- c) **Inhibition** of the propagating chain through chain transfer



In the case of termination by disproportionation, one hydrogen atom is transferred from the hydrogen donor radical to the acceptor radical. Thereby, the donor radical is transformed to an unsaturated polymer chain (ending with a C=C double bond), while the acceptor polymer chain is saturated (only C-C single bonds).

In addition to the bi-radical termination mechanisms, the growth of a radical chain can also be terminated by a bi-molecular reaction with an additional species X (e.g., monomer, polymer, solvent, initiator or an additive). While some additives, so-called inhibitors, are known to form stable radicals  $X\cdot$  with a low tendency to initiate further chain growth reactions, others may yield radicals  $X\cdot$  that start a new chain growth reactions as well, depending on the specific properties of the formed radical species.

An example for the first, inhibiting case is the formation of a peroxy radical in a bi-molecular reaction with molecular oxygen:



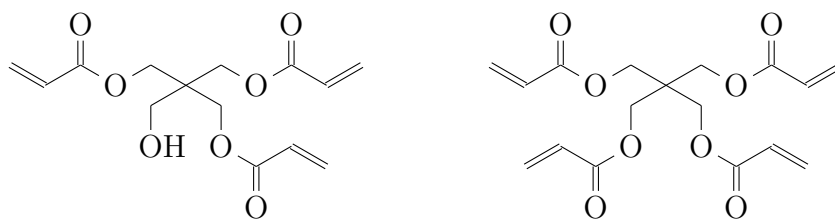
The resulting peroxy radical is known to not reinitiate polymerization efficiently [70]. In contrast, it may very well terminate chain radicals by disproportionation or recombination.

On the contrary, for example thyl radicals, which can easily be generated by hydrogen abstraction from a carbon-bonded sulfhydryl group (thiol), will very efficiently reinitiate propagating chains, so that thiol-based free radical polymerization is very insensitive to oxygen inhibition [71]. As will be discussed later on, this reaction mechanism is crucial for the understanding of the polymerization kinetics in the case of DLW.

Apart from the linear chain-growth mechanism, multiple other reactions may occur. As discussed in the following section (Section 3.2.2), multi-functional acrylates are used for DLW in many cases, so that instead of linear chains, highly crosslinked networks are formed. However, also mono-functional acrylates may form branched polymer chains by so-called back-biting reactions, where the radical is transferred from the end of the chain to a middle position by an intramolecular hydrogen transfer reaction. In addition, side reactions such as  $\beta$ -scission of chain radicals may interfere with the chain growth mechanism.

### 3.2.2 Cross-Linking

As monomers, multifunctional acrylates like the above-mentioned PETA have been shown to give the best results for DLW so far, at least when measured by the achievable resolution. These molecules have three or more functional acrylate groups, each one allowing the molecule to be part of a polymer chain (**Figure 3.5**). Therefore, they are often used as “cross-linkers” in commercial monomer mixtures to form dense polymer networks. However, for DLW, they are often used without additional mono- or bi-functional monomers.



**Figure 3.5:**  
Pentaerythritol tri- and tetraacrylate (PETA and PETTA, respectively).

As each molecule has more than one functional group, one should now take the relative concentration of reacted functional acrylate groups as a measure for the monomer conversion rather than the number of consumed monomer molecules during the polymerization. Also, the reaction kinetics are more complex as compared to the monofunctional analogues introduced in the previous section. At low conversions, propagation will be dominated by incorporation of monomer molecules that still contain only pendant double bonds. With increasing conversion, propagation steps involving pendant acrylate moieties on the same or another macromolecule become more pronounced (intramolecular and intermolecular attack, respectively), leading to rapid crosslinking. Typically, this leads to inhomogeneous networks (formation of so-called “micro-gels”) and also to “trapped” radicals that are sterically hindered from further reactions by their position in the network. Hence, a situation where most monomer molecules are bound to the network is already reached at moderate conversions, with the unreacted functional groups being covalently incorporated into the network. For this reason, gelation and solidification occurs at relatively low conversions well below 100% already, and fully cured networks are hard to achieve. Typically, the formed networks are chemically stable, i.e., they cannot easily be dissolved or removed, for example by the usage of organic solvents.

### 3.2.3 Reaction Kinetics and Temperature Dependence

As indicated in the preceding section, radical-radical termination is always a bi-molecular process. Therefore, it is typically diffusion-limited, i.e., the overall reaction rate is dominated by the probability for the two reaction partners to “meet” [68]. As the same is true for chain propagation, the overall reaction kinetics of polymerization reactions are largely dominated by the diffusivity of the reacting molecules, and hence, also the viscosity of their surrounding. Obviously, the latter undergoes drastic changes during the polymerization

reaction, especially when cross-linked network are formed. Therefore, also the reaction rates are far from being constant with respect to the progress of the overall reaction. Please note that this argument requires that the reagents are very reactive. While this in general is true for acrylates, which have a large propagation coefficient, this precondition and hence the whole statement will not always hold for monomers with different functional groups such as styrene or methacrylates, where the chemical reaction coefficients are comparatively small. In these cases, the overall reaction typically is chemically limited at least at low and moderate conversions, when pending monomer units still are available in large concentration.

In the case of UV photo-polymerization, one can assume that the rate of radical generation is relatively small, so that an quasi-static equilibrium of radical generation and radical termination is reached, with the overall reaction rate being limited by the radical generation. This regime is well investigated through experiments on the reaction kinetics and their theoretical modeling [70, 72–77]. In the same literature, the so-called auto-acceleration is discussed as the most prominent effect of the diffusion-dominated reactivity: With increasing conversion, the mobility of radical chains is suppressed by their increasing molecular weight as compared to unbound monomer units. Therefore, bi-radical termination is less probable compared to the propagation reaction as the latter is then dominated by the relatively large mobility of the unbound (and hence, still small) monomer units. Another effect that has been referred to in the literature on DLW (and which is based on the same assumptions) is the square-root dependence of the polymerization velocity on the initial rate of radical formation – a behavior that can be observed if the reaction reaches a steady state in that the rates of initiation and bi-molecular termination of chains are equal [55, 70, 78].

Also, the reported temperature dependence of the polymerization rate and the final conversions can be explained by the above-mentioned mechanisms: The viscosity of typical fluids such as PETA can be described empirically by an Arrhenius model. As already said, the reaction rate for polymerization typically is diffusion-dominated. Hence, at least for moderate temperature increases up to a few tens of Kelvin, Arrhenius-like behavior is observed for the polymerization and both, polymerization rate and monomer conversion increase with increasing temperature [79].

This being said, it should be noted that in the case of DLW, typical exposure periods are shorter by orders of magnitude compared to typical other applications of photo-polymerization. More precisely, they range from roughly 10  $\mu\text{s}$  to 10 ms, corresponding to writing velocities of 1 cm/s to 10  $\mu\text{m/s}$ . In contrast, several seconds or even minutes are oftentimes used for UV photo-polymerization. For this reason, it is highly questionable whether the above-mentioned assumption of the overall reaction speed being limited by the (low) radical generation rate and the resulting conclusions are applicable for DLW situations as well. In addition, mass transfer through molecular diffusion may influence the reaction due to the small reaction volume. These effects will be discussed in more detail in Section 3.3.5.

#### 3.2.4 Oxygen Quenching

Another important reaction parameter for polymerization is quenching, and most prominently, quenching by atmospheric oxygen [68, 70, 72, 80–82]. Oxygen acts as a polymerization inhibitor in two ways: On the one hand, it quenches the triplet state of photo-initiator molecules, which leads to significant contributions mostly for Type II-initiators with long-living triplet states. On the other hand, and this is presumably the more important mechanism, it inhibits the polymerization reaction by forming relatively stable radicals (that do not, or only hardly, contribute to the polymerization). In many cases, polymerization even starts only once all the oxygen is consumed as the oxygen inhibition rate can be far larger than the rate of polymerization. The reason is that molecular oxygen is highly reactive and also more mobile than the monomers and photo-initiators used due to its relatively small size. As a result, a short time period of low polymerization rate is observed at the beginning of the photo-polymerization reaction in films (inhibition period) in which all oxygen throughout the photo-resist film is consumed [70, 72].

Please note that also the film thickness plays a crucial role for the influence of oxygen: As typical oxygen concentrations are in the order of  $10^{-3}\text{ M} - 10^{-4}\text{ M}$  in typical organic media, the concentration in air is as high as  $10^{-2}\text{ M}$ . Hence, in the vicinity of the interface of the photo-resist and air, additional oxygen will diffuse into the photo-resist as it is consumed according to Le Châtelier's principle. Therefore, inhibition by oxygen diffusion will lead to a reduced monomer conversion.

Hence, a prominent dark reaction (i.e., an ongoing reaction for as long as some 100 ms after the light exposure is stopped) can only be observed in thick films or under oxygen-reduced atmosphere. In these cases, any present



oxygen is already consumed in an early stage of the reaction, and, as oxygen diffusion is suppressed, the reaction is only stopped by termination via radical recombination or radical disproportionation [72].

## 3.3 Reaction Conditions

After the relatively general discussion on homogeneous and “slow” photopolymerization reactions in the preceding sections, we will now focus on the specific reaction conditions of DLW, namely, the small excitation volume and the short, but intense illumination. Various aspects and results of these reaction parameters will be presented in the following. We will start by a short introduction and discussion of the commonly used threshold-model for multi-photon polymerization.

### 3.3.1 Threshold Formation

For simplicity, it is often assumed that solidification by polymerization is a threshold reaction: In order for a polymer structure to withstand the washing process during the sample development step, a certain degree of crosslinking is required. During the early reaction phase, the conversion is still low and forming clusters are still small and therefore soluble. With ongoing reaction, these clusters grow and may also connect to each other. According to percolation theory, such a model leads to a certain threshold value for the monomer conversion for which the average size of polymer clusters diverges [83]. Once this is the case, macroscopic clusters are formed that precipitate from the liquid photo-resist and thereby form solid structures. Obviously, this is a statistical process that will also depend on spatial fluctuations due to the inhomogeneity of the sample.

In such a threshold model, different exposure conditions can be regarded as similar if the number of generated radicals is identical, leading to the same conversion in the corresponding region. Mathematically, this behavior can be described by an absorbed exposure dose  $D$  that scales according to

$$D \propto t_{\text{exp}} R E_{\text{p}}^N \quad (3.4)$$

with the exposure period  $t_{\text{exp}}$ , the laser repetition rate  $R$ , the laser pulse energy  $E_{\text{p}}$  and the nonlinearity of the absorption process  $N$ . In the case of a direct

absorption process, the nonlinearity  $N$  will be given by the number of absorbed photons per event. In order to determine  $N$ , one can, for example, measure the threshold pulse energy  $E_{p,\text{threshold}}$  which is required for the polymerization to start. As can be seen by transforming Equation (3.4) to

$$\log(E_{p,\text{threshold}}) = -N \log(t_{\text{exp}} R / D_{\text{threshold}}) + c \quad (3.5)$$

with an unknown constant  $c$ , the exponent  $N$  can be determined in a log-log plot of the threshold pulse energy  $E_{p,\text{threshold}}$  as a function of the exposure period  $t_{\text{exp}}$  or the laser repetition rate  $R$ .

In practice, one often observes a soft, gel-like transition state of the photo-resist before solid and freestanding structures are formed. In this transition state, the photo-resist is solid and sticks to the substrate or to harder structures, but it suffers from pronounced shrinkage and a lack of mechanical stability. Nevertheless, the simple threshold model can still be helpful for the analysis of experiments if the analysis of the samples is done in a consistent way by comparing similar structures [16].

At this stage, we want to point the reader to the fact that, at least in this simple, yet popular model, it is not possible to draw conclusions on the radical formation mechanism from measuring the line width as a function of the laser intensity [16]: Suppose a generic absorption process with the absorbed dose  $D(I)$  (e.g., for two-photon absorption,  $D(I) \propto I^2$  with the laser intensity  $I \propto E_p$ ). The spatial laser intensity profile (for simplicity in one dimension  $x$ ) is described by  $I(x) = I_0 f(x)$  with the maximum intensity  $I_0$ . For polymerization to occur, it is required that  $D \geq D_{\text{threshold}}$ . As long as  $D(I)$  is monotonically increasing in  $I$  (which certainly is the case for all mechanisms discussed in the literature), we can simplify the condition for polymerization to  $I \geq I_{\text{threshold}}$ . The shape of a written line will then be solely determined by the inequality  $I_0 f(x) \geq I_{\text{threshold}}$ . Therefore, it will depend on the spatial intensity profile  $f(x)$ , while the absorption mechanism (which only enters into the function  $D(I)$ ) has no influence. Hence, a comparison of different line shapes or line widths provides information about the focusing conditions of the writing laser, but it cannot be used to draw conclusions on the underlying absorption mechanism as long as the simple threshold model is applied.

### 3.3.2 Local Confinement

As the whole point of DLW is about highly resolved three-dimensional structuring, let us now discuss briefly how the feature dimensions can be estimated for such inhomogeneous photo-polymerization reactions. In microscopy, the resolution of an optical system is defined as the minimum lateral distance between two different lines (or points)  $a_{xy}$ , which can still be perceived as two distinct objects. The lateral resolution  $a_{xy}$  of an (ideal) microscope can be calculated using Abbe's famous formula

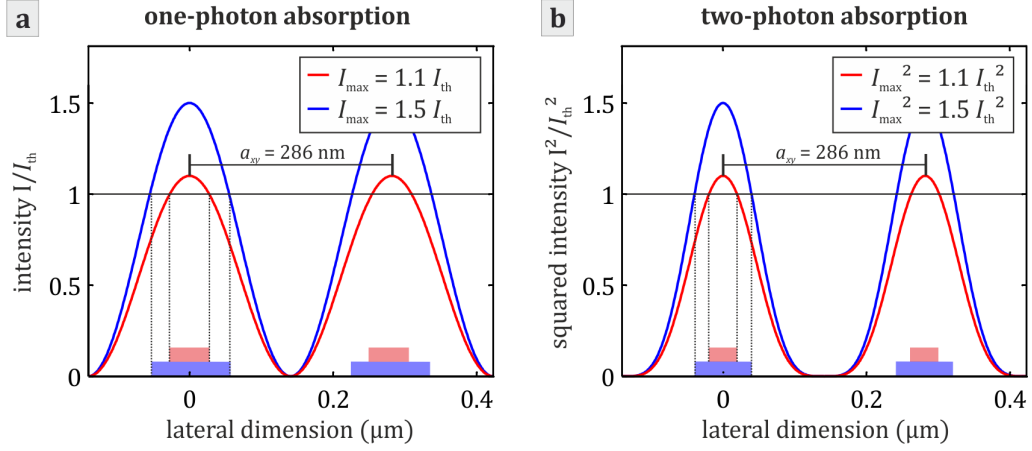
$$a_{xy} \geq \frac{\lambda}{2 \text{NA}} \quad (3.6)$$

with the wavelength  $\lambda$  and the numerical aperture NA, which is defined as  $\text{NA} = n \sin \alpha$  with the refractive index of the immersion medium  $n$  and the half opening angle of the objective lens  $\alpha$  in order to simplify the expression. The formula originates from the assumption that a regular grid can only be resolved if two distinct diffraction orders can be collected by the apparatus [44]. Intuitively, one may argue that from the information of the relative angle of two distinct diffraction orders, the line distance can be calculated. In a similar (yet more complex) argument, the resolution to the third dimension  $a_z$  can be calculated as [11, 84, 85]

$$a_z \geq \frac{\lambda}{n - \sqrt{n^2 - \text{NA}^2}}. \quad (3.7)$$

Translated to lithography, this argumentation corresponds to a simultaneous exposure of the sample by a light pattern. In that case, the resolution limit according to Equations (3.6) and (3.7) gives  $a_{xy} \geq 286 \text{ nm}$  and  $a_z \geq 862 \text{ nm}$  for the experimental parameters of our reference scheme ( $\lambda = 800 \text{ nm}$ ,  $\text{NA} = 1.4$ ,  $n = 1.52$ ). At this point, it should be noted that Abbe's resolution limit does not give any limit on the achievable line width or feature size. As outlined in **Figure 3.6**, in the Abbe limit, the minimum linewidth solely depends on the ability to set the light intensity very close to the writing threshold. In practice, this is typically limited by the laser stability and, more importantly, by the fact that most photo-resists do not show perfectly digital threshold behavior, so that, as pointed out in the previous section, the threshold is "smeared out".

For DLW with multi-photon excitation, the response of the photo-resist is highly nonlinear. Under the assumption of two-photon absorption (but still



**Figure 3.6:** Schematic representation of the lateral resolution and linewidth according to **Abbe’s diffraction limit** for a) one- and b) two-photon absorption. The intensity is given by the sinusoidal interference pattern resulting from two standing waves with a relative angle corresponding to the numerical aperture of the used objective lens. The period of the intensity peaks can be calculated using Abbe’s formula (Equation (3.6)). The feature size is given by the region for which the intensity is larger than some threshold value, i.e.,  $I > I_{th}$ . Therefore, the feature size or line width (broad bars) strongly depends on the writing threshold. In contrast, the distance between two features or lines is solely given by the period of the exposure pattern. In the case of two-photon absorption, the intensity pattern is squared, resulting in thinner features, but still with the same resolution for the given reasoning.

neglecting the nonlinearity of the chemical response), the photo-resist response is proportional to the squared intensity, which leads to a reduced feature size (for comparable intensities). However, the resolution is not altered as can be seen from **Figure 3.6 b**.

While so far, we only talked about simultaneous illumination, DLW is a highly serial process. In that case, the above-mentioned argument cannot be applied as it is mainly based on interference considerations. To resolve this issue, Sparrow’s criterion can be applied [45]. It states that two lines can still be distinguished as long as there is a local minimum in-between these lines in the intensity distribution. Translating this statement from spectroscopy to lithography, it means that the response of the photo-resist caused by the shifted point-spread functions must still have a local minimum.

In the simplest case of a linear response (as in fluorescence microscopy), the response is proportional to the sum of the two point-spread functions. As the par-axial approximation is not valid in the case of high-NA objective lenses, one has to calculate the point-spread function of the optical system numerically or measure it in the experiment. In our case, the (complex) vector field distribution was calculated using a vector Debye approach following [86]. As a reasonable approximation, the focal intensity pattern can be described as a Gaussian distribution with a full width at half maximum of  $\text{FWHM}_{xy} = 322 \text{ nm}$  and  $\text{FWHM}_z = 786 \text{ nm}$ , taking once again the numerical values for our reference DLW scheme. For this data set, the critical distances according to the Sparrow-criterion can be calculated as  $a_{xy} = 290 \text{ nm}$  and  $a_{xy} = 725 \text{ nm}$  (**Figure 3.7**), which is in reasonable agreement with the Abbe formula [11].

In the case of two-photon absorption, the sum of the squared intensities must be considered, yielding  $a_{xy} = 200 \text{ nm}$  and  $a_{xy} = 500 \text{ nm}$ . I.e., as a rough estimate for a two-photon resolution limit, one can take the values from the Abbe formula and divide them by a factor of  $\sqrt{2}$ . More generally, one could define a generalized, approximate multi-photon resolution limit [11] including the nonlinearity  $N$  of the absorption mechanisms:

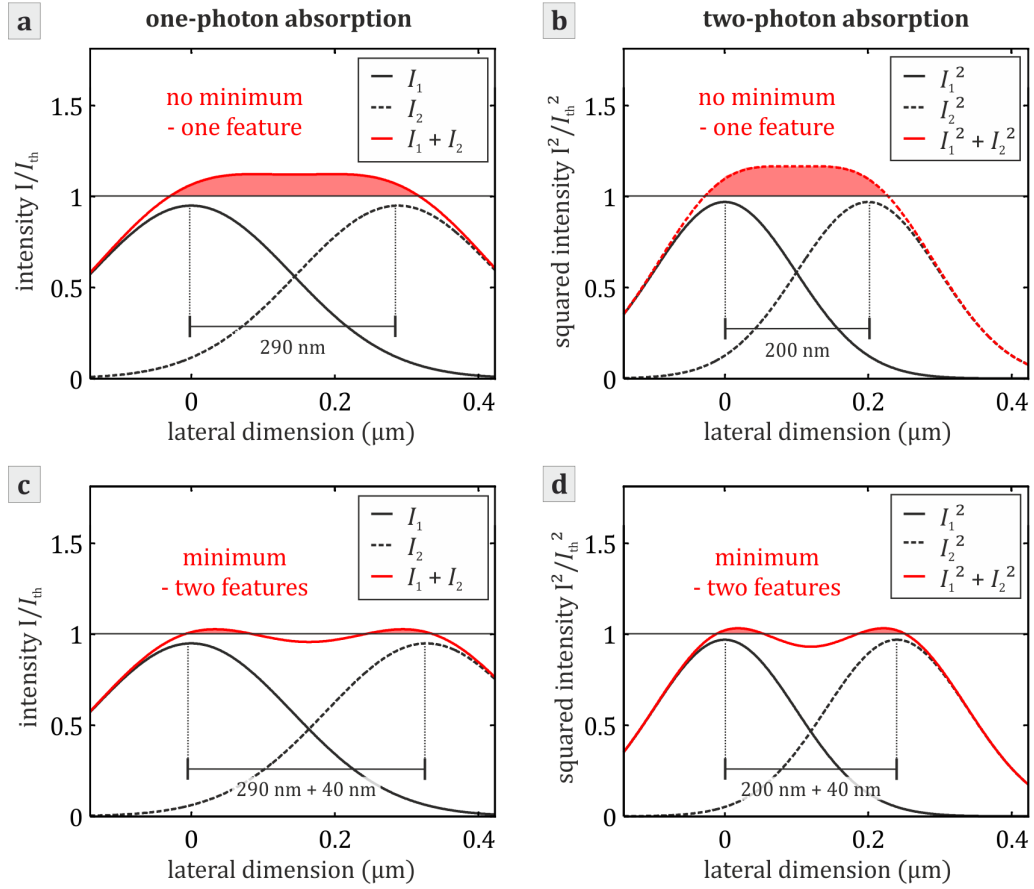
$$a_{xy} \geq \frac{1}{\sqrt{N}} \frac{\lambda}{2 \text{NA}} \quad (3.8)$$

and

$$a_z \geq \frac{1}{\sqrt{N}} \frac{\lambda}{n - \sqrt{n^2 - \text{NA}^2}}. \quad (3.9)$$

If one includes the threshold behavior resulting from the polymerization reaction, the discussion gets slightly more subtle. As long as the resist “remembers” previous below-threshold exposures, the “chemical response” of the photo-resist simply sums up and the above-mentioned argument still holds. If, however, the photo-resist “forgets” previous exposures (e.g., due to radical recombination or diffusion effects), two time-shifted exposures will not accumulate and hence, the response can be described as threshold-like behavior. In that case, the resolution of a writing process would not be limited optically.

However, in practice, it seems that photo-resists do not “forget” their exposure. Possibly, the reason is that the diffusivity of the oligomers formed during a first exposure is low on the relevant timescales, so that already formed macromolecules will not diffuse out of the focal volume and continue growing during further exposures.



**Figure 3.7:** In case of the **Sparrow criterion** for the achievable resolution, we assume two subsequent exposures with a lateral intensity distribution corresponding to a Gaussian distribution  $I_1$  with a full width at half maximum of 322 nm. The intensity pattern  $I_2$  corresponds to a focus shifted with respect to  $I_1$  by **a)**  $a_{xy} = 290$  nm, **b)**  $a_{xy} + 40$  nm = 330 nm, **c)**  $a_{xy} = 200$  nm, and **d)**  $a_{xy} + 40$  nm = 200 nm, where  $a_{xy}$  is the calculated Sparrow limit for one-photon absorption (**a, c**) and two-photon absorption (**b, d**). In the case of two-photon absorption, the sum of the squared intensities must be considered as the illumination of the different patterns occurs subsequently. In that case, two-photon absorption does lead to an improved resolution with  $a_{xy} = 200$  nm being the critical distance for the existence of a local minimum. As can be seen, the accumulated intensity of the patterns  $I_1$  and  $I_2$  shifted by  $a_{xy}$  results in a single (broad) maximum, yielding one single feature (**a, b**). If the shift is larger than the corresponding  $a_{xy}$  (depicted:  $a_{xy} + 40$  nm), two distinct features can be observed (**c, d**). For illustration, the maximum intensity of a single exposure pattern is chosen to be  $I_{\text{max}} = 0.95 I_{\text{th}}$  in all cases.

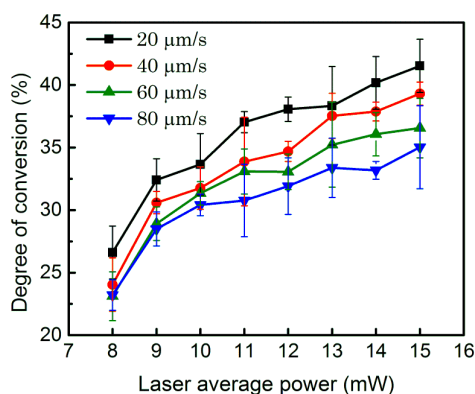
For DLW, a lot of attention has been attributed to the improvement of the writing resolution by using STED-DLW or similar approaches [17, 21, 50, 51, 56] or by moving towards shorter writing laser wavelengths [32, 36–39, 87]. However, improving the writing resolution as such is not the primary aim of this thesis. Nevertheless, one essential requirement for a highly predictable and reproducible writing process is a local photo-resist response to the illumination, which is indicated by a lithography resolution close to the optical limits. Therefore, the writing resolution will often be referenced to as a figure of merit for the DLW process quality within this work.

### 3.3.3 Monomer Conversion

One important parameter for polymerization reactions is the monomer conversion, i.e. the fraction of bound functional groups as compared to the overall number of functional groups. Typically, it is found that a certain threshold conversion leads to a fall-out of the corresponding macromolecular clusters (polymers), which leads to a pronounced threshold behavior as described in the previous section.

In polymer chemistry, various methods have been demonstrated to measure the monomer conversion as a function of the reaction time in the case of bulk reactions. Examples are photo-calorimetric measurements [74], or real-time Fourier-transform infrared spectroscopy [70]. In the case of DLW, however, the reaction occurs only locally, so that methods with high spatial resolution are required. The methods of choice are therefore mostly based on Raman micro-spectroscopy [88–91], i.e., the detection of inelastic light scattering by the vibrational resonances of carbon double bonds. During the polymer formation, the double bonds (C=C) within the functional acrylate groups are homolytically opened and converted to single bonds (C-C), so that the relative height of the corresponding Raman peak (C=C) is lowered during polymerization with respect to the unchanged carbonyl peak (C=O), which serves as a reference [91]. Therefore, the local conversion within the detection region of the Raman microscope can be directly calculated from the corresponding spectra.

For the acrylate-based commercial photo-resist *IP-L 780* (*Nanoscribe*), final conversions of approximately 25%–40% are reached (**Figure 3.8**) [91]. However, other authors report by far higher values for non-commercial resists based on a mixture of two tri-acrylates (60%–75%, **Figure 3.9**) [89] and for



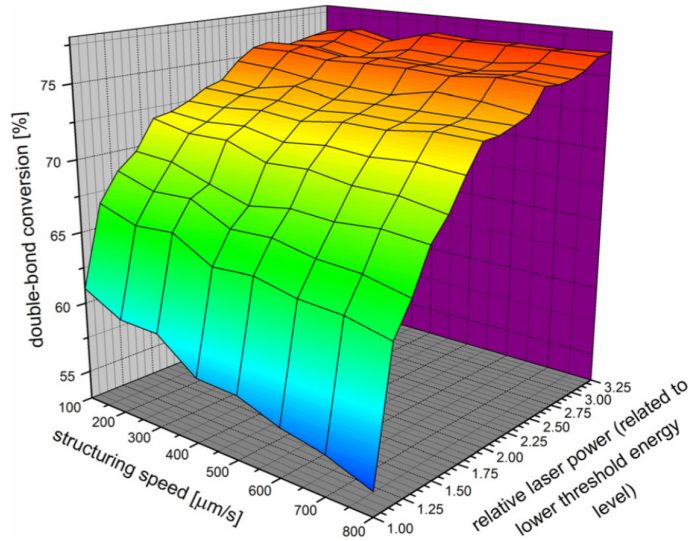
**Figure 3.8:** Degree of conversion calculated from the Raman spectra for blocks written at different writing laser powers and with different writing velocities in the commercial (acrylate-based) photo-resist *IP-L 780* (*Nanoscribe*). Reproduced from [91]. ©2014 Optical Society of America.

organic-inorganic hybrid resists (35 % -75 %) [90]. At this stage, it is not totally clear whether these studies can be directly compared as both, the photo-resist and the instrumentation differ for all of the above-mentioned experiments. Also, a comparative study on this topic including a larger set of different photo-resists and writing conditions is still missing, so that it is unclear to which extent these results are representative for DLW.

In all cases, the gel-point of the photo-resist is at approximately 25-50 % conversion. For photo-resists based on multifunctional acrylates as used in [91], this corresponds to roughly one reacted acrylate group per monomer molecule on average. As one would expect, the conversion increases with higher laser power or, correspondingly, lower writing velocities and saturates towards high writing powers. A quantitative data analysis reveals that at high writing velocities ( $\gtrsim 50 \mu\text{m/s}$ ), a similar exposure dose according to Equation (3.4) leads to the same monomer conversion [91]. At lower writing velocities, however, some saturation effects lower the efficiency of the polymerization reaction and lead to lower conversions than expected [91]. Hence, a simple relation of exposure dose to monomer conversion for the different writing velocities and covering the full range of conversion cannot be found.

Also, in all cases, the final degree of conversion achieved is far below 100 %. This can be attributed to the fact that only multi-functional monomers are being used, so that sterical hindering and lacking mobility of dangling acrylate groups hinder the progress of the polymerization at a relatively early stage





**Figure 3.9:** Degree of conversion calculated from the Raman spectra for woodpile photonic crystal benchmark structures written at different writing laser powers and with different writing velocities in a triacrylate-based photo-resist. Reproduced from [89]. ©2011, AIP Publishing LLC.

already. This may have several negative effects. First of all, the final structures may lack stability as the degree of cross-linking is non-ideal. Second, there may be remaining monomer molecules present after the polymerization reaction due to the incomplete reaction and partly also due to polymer swelling (i.e., incorporation of unbound molecules into the network after the actual polymerization process). These unbound monomer molecules will consequently be washed out by the developing agent, leading to an effective volume reduction of the written structures. However, one should keep in mind that the density of polyacrylate networks is higher than the density of the corresponding monomers. This leads to a volume shrinkage in the order of a few percent during polymerization as well [92], even if the above-mentioned effects can be eliminated.

In order to tackle these issues of structure stability and volume shrinkage, it seems most promising to increase the mobility of the functional groups through a reduction in the photo-resist viscosity, either by mixing the photo-resist with solvents or by adding “smaller” monomers which have only one or two functional groups. Within this thesis, some attempts were made to improve the DLW process based on these approaches by investigating selected other monomers and solvents. Unfortunately, none of them were successful in the

sense of an improved structure quality. However, further investigations may lead to promising results, especially when systematic material screenings can be combined with analysis techniques such as the Raman microspectroscopy approach introduced in this section.

#### 3.3.4 Heat Conduction

So far, we have always assumed a strictly local response of the photo-resist. However, as typical feature sizes in DLW are in the order of 100 nm, non-local effects such as heat conduction and chemical diffusion may play an important role for the DLW process. Therefore, these will be discussed in the following two sections.

For many laser machining processes, it has turned out that thermal effects like local heating and heat conduction have an essential influence on the resulting machining quality [93]. For the special case of DLW, the situation is not quite clear, as two-photon absorption is a photo-chemical rather than a photo-thermal process and hence, not necessarily goes along with sample heating. However, heating may still occur as a parasitic effect, either by the energy deposited in the 2PA step, the exothermal polymerization reaction, or, most prominently, by parasitic absorption processes such as a (presumably weak) one-photon absorption of any of the photo-resist components (without necessarily yielding any reactive species). As especially for the latter, the magnitude of this effect is hard to estimate, the measurement of the actual local heating represents one of the major topics of this thesis.

However, on the involved time scales for DLW, cooling effects must be considered to estimate the actual temperature changes for a given amount of deposited energy. Therefore, we want to provide the reader with a rough estimate on the characteristic length and time scales of cooling effects in a typical DLW settings, starting with a short discussion on the heat flow from the voxel to the surrounding. This will hopefully give some hints to determine under which conditions heating may or may not play a role for the processing behavior. In order to do so, we introduce the characteristic cooling time

$$\tau_c = \frac{\rho c_p l_c^2}{4\kappa} \quad (3.10)$$

for a given length scale of the cooling zone  $l_c$  [94]. These two quantities are connected by the mass density  $\rho$ , the specific heat  $c_p$ , and the heat

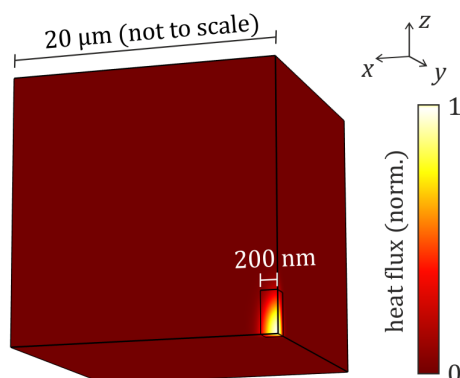
conductivity  $\kappa$ . This simple relation can easily be derived from Fourier's heat-conduction law. It gives a good estimate for the typical distance covered by the heat flow within a certain time and vice versa [93]. For typical monomers, the prefactor can be estimated from literature values as  $\frac{\rho c_p}{\kappa} \approx 10^7 \text{ m/s.}^2$  As we will discuss in the next section, a very similar argument can be applied for Fick's diffusion of chemical species.

For the application to DLW, several different time scales must be considered. For high repetition rate writing lasers ( $R = 80 \text{ MHz}$ ), the time span between two pulses is 12.5 ns, with a pulse duration of around 200 fs at the sample position. Setting the 12.5 ns as the cooling time  $\tau_c$ , we find a characteristic cooling length of  $l_c = 70 \text{ nm}$ , which is less than a typical focus radius (165 nm). Hence, heat deposited by subsequent pulses will largely accumulate. However, typical exposure periods are in the order of milliseconds, so that at the end of the exposure, heat flow from the exposed region to the surrounding leads to a substantial broadening of the thermal profile (e.g.,  $l_c = 20 \mu\text{m}$  for  $\tau_c = t_{\text{exp}} = 1 \text{ ms}$ ). In this case, heat conduction obviously leads to a saturation of the maximum temperature increase. In order to find the on-set time of conductive cooling, we apply a rather rough approximation. Namely, we expect that cooling sets in when the cooling length  $l_c$  for the given exposure period is larger than the radius of the focus (165 nm). At this point, heat flow to the surrounding comes into play and local heating is largely suppressed. In our example, this is the case after roughly 100 ns or 8 laser pulses.

We find that this simple estimate is in good qualitative agreement with a more sophisticated three-dimensional model using COMSOL Multiphysics (**Figure 3.10**). In that model, we numerically solved the heat conduction equation in space and time, assuming a time-dependent, Gaussian-like intensity distribution as heat source with geometric parameters corresponding to the actual experimental situation (**Figure 3.11**). Once again, heat conduction leads to a substantial broadening as compared to the heat flux distribution after a typical exposure period of some milliseconds (**Figure 3.11 a, b**). As argued before, the peak temperature does not change significantly anymore after these exposure periods. At the same time, hardly any cooling occurs

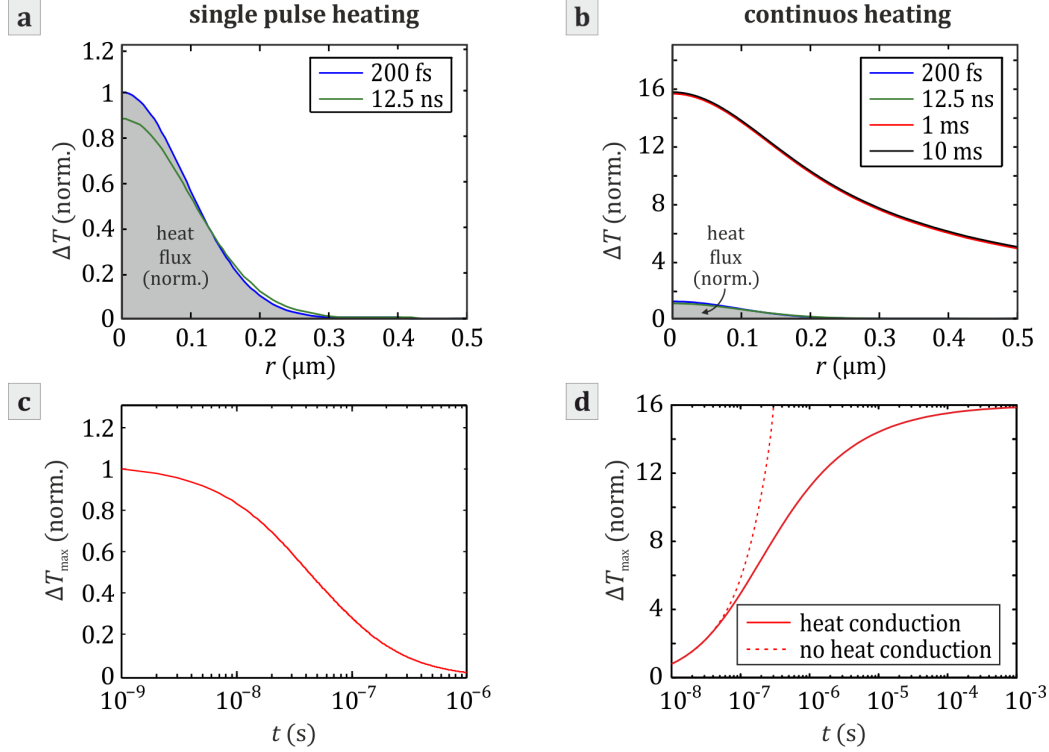
---

<sup>2</sup> Values for styrene monomer (<http://www.styrenemonomer.org/2.2.html>, retrieved on March 24, 2015). Very similar values are expected for other organic liquids and, in particular, monomers.



**Figure 3.10:** Graphical representation of the modelling geometry of the COMSOL model for the estimation of heat conduction effects. The time-dependent heat source is modelled as a Gaussian distribution with parameters corresponding to the focus spot of the writing laser ( $\text{FWHM}_{xy} = 330 \text{ nm}$ ,  $\text{FWHM}_z = 2.5 \times \text{FWHM}_{xy}$ ). For symmetry reasons, only one eighth of the full geometry is modeled, with symmetry boundary conditions on the inner boundaries and thermal insulation boundary conditions of the outer boundaries. The relevant material parameters are set according to the above-mentioned estimation for typical monomers ( $\frac{\rho c_c}{\kappa} = 10^7 \text{ m/s}$ ).

between the end of a single pulse exposure (200 fs) and the arrival of the next pulse after 12.5 ns (corresponding to  $R = 80 \text{ MHz}$ ), which means that on this time-scale, the thermal impact of subsequent pulses indeed largely accumulates. In order to better characterize these two regimes, we display the peak temperature as a function of time in the cases of either heating by one single pulse (**Figure 3.11 c**) or by a continuous heat source (**Figure 3.11 d**). This corresponds to a situation where the voxel is heated by a large number of pulses, so that the heat source can be treated as quasi-continuous. If no conductive cooling occurs, deposited heat simply accumulates. However, with the heat conduction “switched on”, the peak temperature in the center of the laser focus starts to saturate after around 100 ns. After 1 ms (a typical exposure period), the peak temperature is increased to a value which is roughly 15 times higher than the average temperature increase due to a single pulse, even though a total number of 264.000 pulses impinges onto that specific spot. In the other case of heating by one single pulse, one can see that the peak temperature indeed decays to even a bit less than 37% (1/e) of the original value within roughly 100 ns, indicating that this is the relevant time-scale for



**Figure 3.11:** Calculated temperature distribution at selected instants in time (**a**, **b**) and calculated peak temperatures as a function of time (**c**, **d**). The incoming heat flux is indicated by the gray areas. As the absolute magnitude of the temperature change is unknown, all curves are normalized to the temperature change due to one single pulse. **a)** Conductive broadening of the temperature distribution after one single pulse, directly after the end of the exposure and at the beginning of the subsequent pulse. **b)** Conductive broadening of the temperature distribution for a continuous heat source after typical exposure periods. **c)** Peak temperature change after a single pulse exposure. The peak temperature significantly drops after 100 ns, which is similar to the corresponding estimated cooling time scale  $\tau_c = 70$  ns for  $l_c = 165$  nm. For high repetition rates, heat deposited by subsequent pulses will accumulate, while at low repetition rates, the temperature increase is dominated by the peaks of the pulse-to-pulse temperature oscillations. **d)** Peak temperature change in the case of a continuous heat source. Heat conduction starts after approximately 100 ns, leading to a reduced maximum temperature.

conductive cooling to occur. However, if the exposure period is longer than these 100 ns, then the resulting temperature profile broadens as well, and hence, also the cooling time increases.

Translating these findings to the DLW process, this means that the overall thermal behavior as a function of the applied repetition rate can be described within two regimes: At high repetition rates, the temperature increase is dominated by heat accumulation, whereas at low repetition rates, heating and cooling due to single pulses dominate. Obviously, at least in this simple model, the maximum peak temperature does not at all depend on the repetition rate in the single-pulse dominated regime.

The transition repetition rate between the two regimes can be estimated from the given data by an argument slightly different to the above-mentioned time-scale for the on-set of heat conduction. Namely, it occurs when the accumulated temperature increase after the full exposure period in the continuous case and the (temporal) peak temperature after a single pulse (both expressed in terms of the average temperature increase during one pulse) are the same: In our example, the accumulated temperature increase for typical exposure periods of 1 ms is approximately 16 times larger than the temperature change due to one single pulse (**Figure 3.11 d**). If in between two pulses, the peak temperature decreases by the same factor, the accumulated temperature increase at the end of the exposure is just as large as the peak temperature due to one single pulse. In this example, this is the case for a pulse-to-pulse period of 500 ns (**Figure 3.11 c**), corresponding to a repetition rate of 2 MHz. Along these lines, repetition rates above 2 MHz are considered as “high” repetition rates throughout this manuscript, while by “low” repetition rates, values smaller than 2 MHz are referred to.

#### 3.3.5 Molecular Diffusion

As the conditions in DLW are highly inhomogeneous in space (and also in time), diffusion may not only play a role by limiting certain reaction velocities as described in Chapter 3.2.1. It may also influence the writing process by introducing non-local effects through the diffusion of chemical species from the reaction volume to the surrounding and vice versa. Diffusion in this sense (e.g., diffusion of starting radicals) has been expected to be responsible for different effects like the still limited resolution in super-resolution DLW schemes [17, 57]. In analogy to our discussion on cooling by heat conduction, we start by calculating some characteristic figures to estimate under which

conditions diffusion effects should be considered. From Fick’s law of diffusion, we find that a characteristic diffusion time  $\tau_d = D / 4 l_d^2$  can be calculated as a function of the length scale of interest  $l_d$  for a species with diffusivity  $D$ . For diffusion in liquids,  $D$  can be calculated by the Stokes-Einstein Equation  $D = k_B T / (6 \pi \eta R_0)$  with the Boltzmann constant  $k_B$ , the temperature  $T$ , the dynamic viscosity  $\eta$ , and the hydrodynamic radius of the diffusing species  $R_0$ . Typical monomers for DLW are relatively viscous, e.g.,  $\eta \approx 1$  Pa/s for PETA at room temperature.<sup>3</sup> Unfortunately, the hydrodynamic radii of typical molecules in “unconventional solvents” as PETA are not easy to determine. As a presumably rather rough estimate, we shall use the physical radius of the corresponding molecules.

For diffusion to play a role for the overall process, the diffusion length has to be in the order of the voxel radius, i.e.,  $l_D \gtrsim 150$  nm. For molecular oxygen ( $R_0 \approx 66$  pm), this corresponds to a diffusion time of  $\tau_d \approx 2$  ms, so that in the case of longer exposures, oxygen can diffuse into the reaction volume from the surrounding and thereby prevent polymerization. A detailed analysis of the resulting effects of this behavior will be given in Section 6.1.1.

When considering diffusion of larger molecules like the monomer or the photo-initiator (molar mass  $M \approx 300$  g/mol), values of several hundred picometers are assumed for the hydrodynamic radius (e.g.,  $R_0 = 750$  pm, which is the radius of a sphere covering the same volume as one PETA molecule). In that case, the diffusion times are even larger, i.e.,  $\tau_d \approx 20$  ms for PETA. As we will see in Section 6.2, this is longer than typical polymerization durations even in the case of long exposures. Hence, diffusion of these species is unlikely to result in a significant contribution to the overall process as the reaction duration is too short for diffusion of these molecules to occur. For growing polymer clusters, the values for  $\tau_d$  become even larger while at the same time, the solvent viscosity increases with the ongoing polymerization. Therefore, diffusion of the relatively large photo-initiator and monomer molecules can be neglected at all later stages of the reaction in most cases. An example where photo-initiator does actually play a role due to the extremely small writing velocity will be given in Section 7.

---

<sup>3</sup> Many thanks to Dr. Michael Kempf and Prof. Manfred Wilhelm (Institute for Technical Chemistry and Polymer Chemistry, Karlsruhe Institute of Technology) for the measurement data and discussions on this issue.

### 3.3.6 Post-Polymerization

In most schemes for two-photon polymerization, the reaction pathway can be understood as a two-step reaction, with initiation as the first step and polymerization as the second. For this reason, we have discussed these steps independently in the previous sections. Even though this is a common and in many cases justified assumption, there are cases in which the two steps can interfere. More specifically, if a voxel is exposed to the writing laser for a period that is similar to or even longer than the polymerization duration, the two reaction steps occur simultaneously and may interact. For this reason, in cases with long exposure periods (or, equivalently, for slow writing velocities), these kinds of inter-dependencies must be considered. For example, the optical properties of the photo-initiator may change due to the change in solvent viscosity during polymerization as these are in general solvent-dependent.

As will be discussed in Section 6.2, typical polymerization durations are in the order of a millisecond or even less. Hence, to be on the safe side to avoid any such interactions, one would have to use exposure periods much smaller than the “intrinsic” polymerization duration. This would correspond to exposure periods as short as approximately 100  $\mu\text{s}$ , or, correspondingly, velocities in the range of some millimeters per second.

However, in practice, clear indications of such interplay of initiation and polymerization are only found for writing speeds of less than 50  $\mu\text{m/s}$  in the form of saturation effects as discussed later on. We therefore consider the assumption that initiation and polymerization can indeed be regarded as separate and independent steps to be satisfied for the presented experiments. In the following, this assumption will be referred to as the “post-polymerization” assumption.



# 4

## Chapter 4

---

# In-situ Analysis Techniques

As outlined in the previous chapter, the reaction conditions during DLW are different as compared to most literature on photo-polymerization. While theoretical considerations on different reaction pathways and parts thereof are included in various publications, they often lack experimental justification [31, 83, 95]. One reason therefore is that the photo-chemical reaction pathway is quite complex in the case of DLW, while the number of observables is relatively small (e.g., writing threshold and writing resolution). In contrast, the number of experimental parameters that can be varied in order to study their influence on the DLW process is large (e.g., writing speed and thereby exposure period, laser repetition rate, laser wavelength, sample temperature, or photo-resist composition). However, for some of these, the interpretation of the results is not very straight-forward, with the main reason that they influence not only one single reaction step. For example, if the exposure period is varied, one can in principle adjust the laser power such that the overall amount of generated radicals is kept constant to allow for conclusions on the radical generation mechanism. Yet, at the same time, also the rate of radical generation changes and thereby, the overall polymerization dynamics may be different if, for example, oxygen diffusion is taken into account.

We took two experimental routes to solve this issue. Namely, we varied such experimental parameters that selectively influence only one reaction step, and we introduced in-situ characterization techniques that provide observables other than the written structures as such. Obviously, for the in-situ characterization, the DLW setups had to be extended in different ways. In the following, we describe the experimental setting for these in-situ analysis techniques. The actual results as well as their interpretation will be discussed in the subsequent chapters.

## 4.1 Local Thermo-Probing

While the determination of the nonlinearity of the absorption process that leads to radical generation and thereby polymerization can be determined by a variation of the repetition rate of the writing laser, such experiments will not give any hints on possible other (parasitic) absorption mechanisms that may occur in parallel. However, these may still influence the writing process, for example by sample heating. It has been argued in the past that the structuring quality of DLW might be largely influenced by thermal effects and local sample heating [31, 96] (which indeed is the case in a large number of industrial laser-based machining processes such as laser cutting or laser ablation [93]). In order to decide whether this statement is true (and, therefore, thermal effects deserve further attention), it is necessary to determine the actual degree of sample heating.

Unfortunately, the dominant heat sources in the case of DLW are largely unknown. The experimental determination of absorption cross-sections for multi-photon absorption processes is experimentally challenging and yields rather an order of magnitude estimate than precise and reliable numbers [60]. In addition, at the applied high intensities, excited state absorption processes are likely to occur. For these reasons, an estimation of the local heating is hardly possible. At the same time, the standard methods for temperature measurements are not applicable as they typically lack spatial resolution or interfere with the writing process.

We therefore adapt a new technique based on the detection of the fluorescence of upconverting nanoparticles (UCNPs). These particles are mixed into the photo-resist and can be excited independently of the writing process by 980 nm wavelength continuous wave (cw) irradiation. Their luminescence spectrum in the visible region shows temperature dependent features which then can be used as a measure for the local temperature within the luminescence detection region. The use of particles which feature efficient up-conversion is advantageous in that the excitation wavelength is far from any absorption bands of the photo-resist ingredients, while the luminescence can be detected without much experimental effort. The used  $\text{NaYF}_4 : \text{Yb}^{3+}(20\%), \text{Er}^{3+}(2\%)$  nanoparticles are the most efficient up-converters known so far [97]. They have been used for various applications mostly from biophysics and bio-imaging, including the measurement of the local temperature inside a cancer cell [98–101].

The high efficiency of these particles originates from the fact that the up-conversion is not based on “direct” two-photon absorption, but on energy-transfer up-conversion [102,103]. More precisely, the  $\text{Yb}^{3+}$ -ions absorb 980 nm cw irradiation through an electronic one-photon excitation process within the  $4f$ -orbitals [104]. As this process should be quantum-mechanically forbidden for single ions and only is enabled through host-lattice interactions, typical lifetimes of these inter-mediate states can range up to 100  $\mu\text{s}$  [105]. Therefore, the energy of several excitation events of these “sensitizer”-ions can be transferred efficiently to an “activator”-ion ( $\text{Er}^{3+}$ ), which will then fluoresce through several optical transitions in the visible and infrared region (**Figure 4.1**). Please note that the measured spectrum is expected to react to temperature changes much faster than the above-mentioned 100  $\mu\text{s}$  as the underlying non-radiative processes are assumed to be relatively fast.

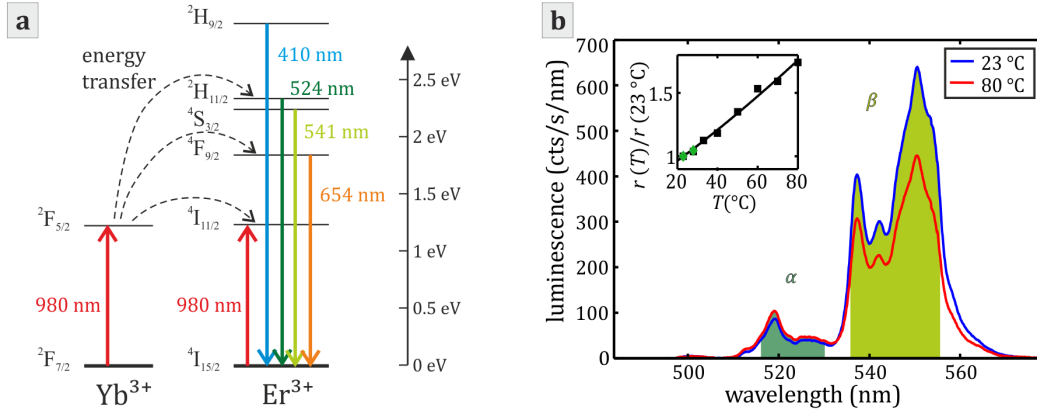
In order to interpret the measured spectra, the ratio  $r = I_{525\text{ nm}} / I_{550\text{ nm}}$  of the integrated intensities of the two peaks around 525 nm and 550 nm is recorded as a function of the sample temperature using a temperature-controlled sample holder (**Figure 4.1 b**, inset). We find that  $r(T)$  can be fitted by a Boltzmann factor, corresponding to the interpretation of a thermal occupation of the underlying states:

$$r_{\text{fit}}(T) = r(T_0) \exp\left(\frac{-\Delta E_{\text{fit}}}{k_{\text{B}}(T_0 - T)}\right). \quad (4.1)$$

The energy difference  $\Delta E_{\text{fit}} = 0.089\text{ eV}$  obtained by this fit is in good agreement with literature data [100] and also corresponds well to the spectral separation of the two peaks ( $\approx 0.1\text{ eV}$ ). Therefore, we expect that the temperature calibration is also valid outside the temperature range we use for the calibration, which is limited to a maximum temperature of 80° C for technical reasons.

The UCNPs were synthesized using a previously described, but slightly adapted method [37,94].<sup>1</sup> Namely, a mixture of rare earth trifluoroacetates (0.3338 g (0.78 mmol)  $\text{Y}(\text{CF}_3\text{COO})_3$ , 0.1024 g (0.20 mmol)  $\text{Yb}(\text{CF}_3\text{COO})_3$ , and 0.0102 g (0.02 mmol)  $\text{Er}(\text{CF}_3\text{COO})_3$ ), synthesized according to [107]) is inserted into a three-necked flask which already contains a mixture of 3.12 ml oleic acid (10 mmol), 3.29 ml oleylamine (10 mmol), 6.4 ml 1-octadecene (20 mmol) along with 0.136 g (1 mmol) of  $\text{Na}(\text{CF}_3\text{COO})$ . After heating to 100° C under vacuum for 30 minutes for the removal of any traces of water and oxygen, the solution is

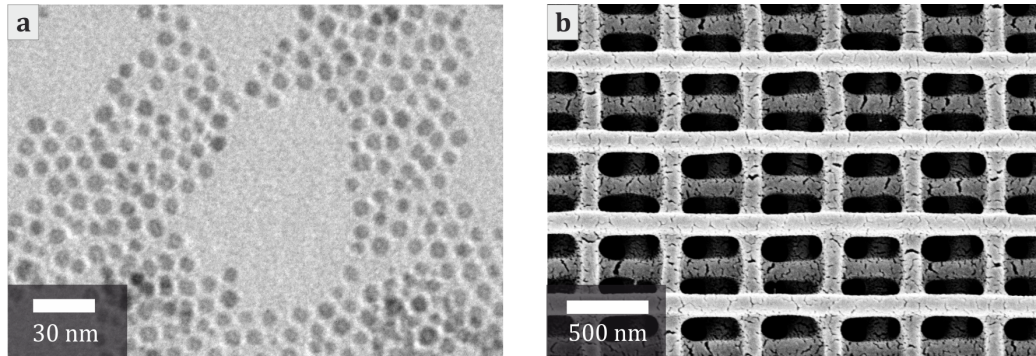
<sup>1</sup> Particle synthesis and analysis through transmission electron microscopy by Y. Mange and T. Nann.



**Figure 4.1:** **a)** Energy levels of NaYF<sub>4</sub> : Yb<sup>3+</sup>, Er<sup>3+</sup>, including the most important transitions [106]. The detected fluorescence peaks for the temperature measurement stem from the <sup>2</sup>H<sub>11/2</sub> - and <sup>4</sup>S<sub>3/2</sub> - states, which are presumably thermally occupied. Red and green arrows indicate possible transitions that are associated with excitation and fluorescence, respectively. **b)** Fluorescence spectra of the particles at different sample temperatures. While the peak centered around 550 nm decreases with increased temperature, the 525 nm – peak gets larger. The ratio of the two peaks, which does not depend on the overall measured fluorescence intensity, can therefore be used as a measure for the local temperature within the detection region. Inset: Normalized ratio of the two luminescence peaks at different temperatures, measured using an oil immersion objective lens (green) and an air objective lens (black) to avoid thermal conduction through the immersion medium. The fit according to Equation (4.1) (black line) serves as a calibration curve for the actual in-situ temperature measurements. Figure reproduced from [94]. ©2013, AIP Publishing LLC.

further heated to 310 °C at a heating rate of 20 °C/min and maintained under Argon atmosphere for 60 minutes before cooling down to room temperature. Typically, the UCNPs were precipitated and washed by repeatedly adding ethanol ( $\approx 10$  ml) followed by centrifugation. Finally, the particles were re-dispersed in chloroform or toluene and added to a readily mixed photo-resist. The solvent was removed by vaporization at room temperature.

The resulting UCNPs have a diameter of approximately 10 nm (**Figure 4.2 a**). As the 980 nm excitation laser is not absorbed by the photo-resist itself, it does not influence the DLW process as such. To demonstrate this, woodpile

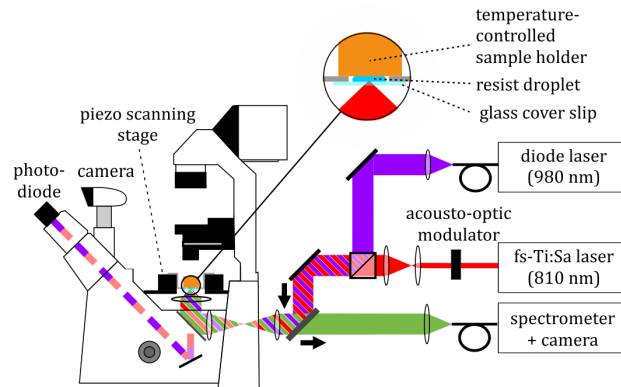


**Figure 4.2:** **a)** Transmission electron micrograph of a typical sample of UCNPs. The particles were dispersed in chloroform before they were spin-coated onto a substrate. **b)** Woodpile photonic crystal structure (rod distance 500 nm) written into a photo-resist containing the nanoparticles. No indications of an influence of the UCNPs onto the DLW process can be observed (e.g., reduced structure quality due to particle agglomerations). Figure reproduced from [94]. ©2013, AIP Publishing LLC.

photonic crystals with a rod distance of 500 nm were written as benchmark structure (**Figure 4.2 b**). On the other hand, the particle luminescence is not influenced by the writing process either as it originates from crystalline doping sites and hence, we expect a negligible influence of the properties of the surrounding medium such as the refractive index, which obviously change upon polymerization.

In order to perform the corresponding measurements, the MaiTai-Setup was adapted accordingly by including a fiber-coupled 980 nm wavelength laser (*Laser Components GmbH*, 300 mW) for the excitation of the UCNPs and a fiber-coupled spectrometer (*HR460, Jobin Yvon*) with a liquid-nitrogen-cooled silicon CCD camera (*LN/CCD 1340/100-EB/1, Princeton Instruments*) (**Figure 4.3**). To obtain a resolution-limited temperature profile and suppress any background, the luminescence is collected in a confocal scheme with the single-mode fiber acting as pinhole.

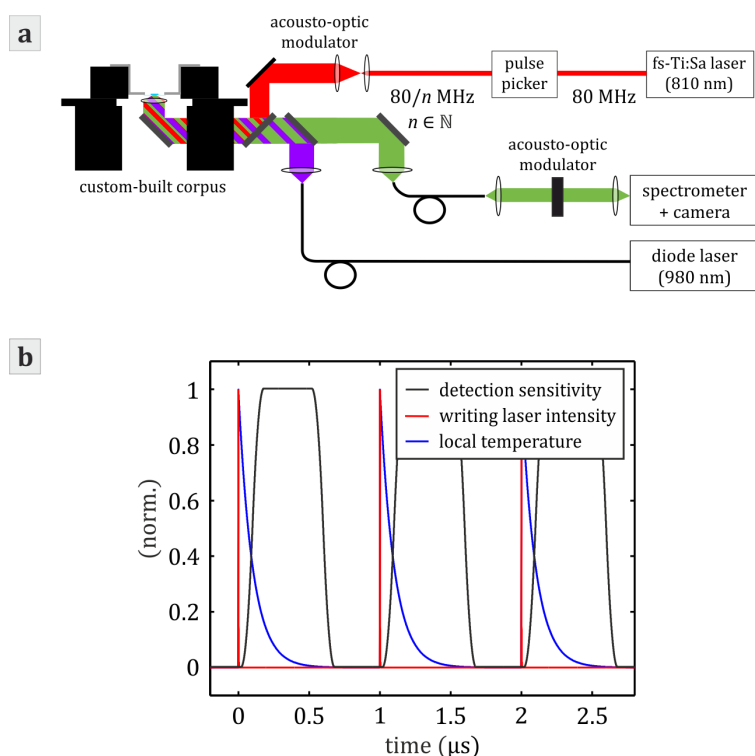
Both, the excitation laser and the detection volume can be characterized by the gold bead scanning method (Section 2) and indeed are found to be diffraction limited. The detection region therefore has a lateral size of approximately 220 nm and an axial extent of around 700 nm (both FWHM), which is smaller



**Figure 4.3:** Extended DLW setup for the temperature measurement. A cw diode laser (wavelength 980 nm) serves as the excitation laser for the UCNPs, but does not influence the DLW process. The luminescence is collected in a confocal scheme by coupling it into a single-mode fiber. Figure reproduced from [94]. ©2013, AIP Publishing LLC.

than the writing laser focus. By the same method, the foci of writing laser, excitation laser and the detection region are co-aligned. For the measurements of the spatial temperature profile, the writing laser is shifted with respect to the excitation laser, with the latter still being co-aligned with the detection region.

Experimentally, we found that different absorption mechanisms appear to be dominating for high and low repetition rates (Section 5.1). Hence, it is of interest to also measure the local sample heating as a function of the writing laser repetition rate. In order to do so, the Chameleon-Setup was adapted in a similar way (**Figure 4.4 a**). As a typical time constant for heat conduction on the relevant spatial scale is in the order of 100 ns (Section 3.3.4), the local temperature increase can be expected to show oscillatory behavior for repetition rates lower than 10 MHz. In order to measure the maximal rather than the average heating (or at least a value close to it), time-gated measurements were performed in these cases. I.e., the fluorescence was chopped by an additional acousto-optic modulator between the fiber out-coupling and the spectrometer entrance slit. As a disadvantage of this approach, the detection bandwidth is limited to approximately 510 nm–550 nm due to the wavelength-dependent diffraction angle of the acousto-optic modulator. Therefore, the subtraction of typical background signals, which are spectrally broad and relatively flat,



**Figure 4.4:** a) Extended DLW setup for the temperature measurement with variable repetition rate. The detector signal can be time-gated and triggered by the writing laser in order to perform time-gated fluorescence measurements. b) Typical time dependence of the writing laser intensity, the sensitivity of the time-gated fluorescence detection and the local temperature (all normalized) for a selected repetition rate (1 MHz).

is somewhat more difficult (e.g., background luminescence going along with monomer explosions in the case of overexposure). However, the detection window can be time-shifted with respect to the writing laser pulse, so that the (very quickly decaying) background signals are suppressed by the time-gating as well.

The “open” time-gate is set to its minimum duration of 500 ns, which originates from the effective rise- and fall times of the used modulator. The time-gating is triggered by the writing laser, starting with a shift of approximately 100 ns after each writing laser pulse for all repetition rates of 1 MHz and below (**Figure 4.4 b**) and “smeared out” by the rise- and fall time constants of the acousto-optic modulator (nominally approximately 80 ns at the given focusing

conditions). For 1 MHz and lower repetition rates, the width and time-shift of the detection window can be kept constant, so that the averaging time stays the same. However, the overall count number of the luminescence detection is proportional to the repetition rate, so that the overall measurement time must be adapted accordingly to keep the accuracy of the temperature measurement constant.

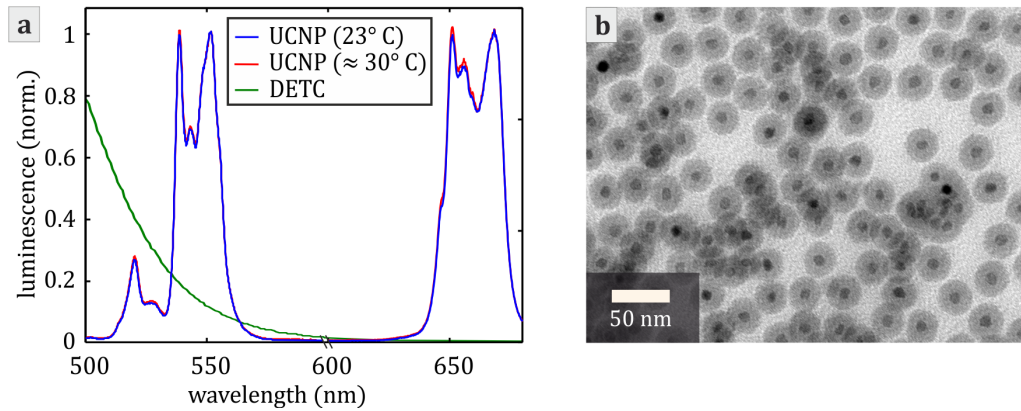
Unfortunately, the value for the characteristic cooling time (100 ns) is still smaller than the temporal width of the detection window (**Figure 4.4**). Hence, any measured temperature will always correspond to a time-averaged value, with a peak temperature which is somewhat larger than the displayed value. In principle, the magnitude of the correction factor can be estimated for the typical data displayed, yielding a factor of around 10 by which the peak temperature is larger than the measured average value. However, this value is very sensitive to the actual temporal shape and position of the detection window and, more importantly, we will see that the temperature profile can be much wider than this theoretical value in the case of monomer explosions (**Figure 5.6**). Hence, the correction factor will be reduced in this situation and cannot be calculated easily. Therefore, the displayed data always correspond to time-averaged temperatures instead of peak temperatures.

To measure the local temperature change during DLW, spectra taken under different writing conditions are compared to spectra, where the sample is kept at room temperature. More precisely, the local temperature in the detection volume is calculated from the ratio  $r$  of these spectra and the calibration curve (inset of **Figure 4.1 b**, Section 5.2).

### 4.1.1 Local Thermo-Probing with Fluorescent Photo-Resists

Some of the photo-resists which have been studied extensively in the literature are based on fluorescent photo-initiators like DETC. For these photo-initiators, the measurement of the local temperature based on the luminescence of the nanoparticles is more challenging, as the subset of peaks for which the UCNP spectra show the largest temperature dependence is spectrally overlapping with the DETC fluorescence (**Figure 4.5 a**). Also, it would be interesting to extend the approach to investigate possible heating induced by the depletion laser in STED-DLW, which is in the green wavelength regime as well (typically,  $\lambda = 532$  nm). In order to solve this issue, several approaches may be considered:





**Figure 4.5:** **a)** UCNP spectra at different sample temperatures. For both spectral regions ( $< 600$  nm and  $> 600$  nm), the spectra are normalized to the long-wavelength peaks around 550 nm and 660 nm, respectively. The short-wavelength peaks of each group are increased at the higher temperature in both cases and can therefore in principle be used to measure the temperature. For comparison, a DETC luminescence spectrum is displayed as well (normalized to its peak at 420 nm). Please note that the absolute height of the UCNP peaks is similar in both spectral regions, while the DETC fluorescence is larger by three or more orders of magnitude under typical exposure conditions close to the DLW writing threshold. **b)** Transmission electron micrograph of exemplary UCNPs with a silica shell to prevent the FRET-effect in photo-resists containing DETC. The particles were dispersed in chloroform before spin-coating onto the substrate.

### Background subtraction and spectral filtering

In principle, it should be possible to eliminate both, the DETC fluorescence and the depletion laser signal by proper background subtraction. However, this turned out to be highly nontrivial, as the absolute count rates of the luminescence are smaller than the background signals by 4-5 orders of magnitude or more, and both are strongly wavelength dependent in the wavelength regime which is traditionally used for temperature measurements with these UCNPs (520 nm – 550 nm). Hence, due to background fluctuations, the signal-to-background ratio is too small to allow for temperature measurements with the required precision.

### Time-gating

Using the time-gating approach presented in the previous section, the fluorescence and the depletion laser can be largely suppressed using the same setting as shown in **Figure 4.4**, while still detecting the UCNP luminescence in between the writing laser pulses. Experimentally, a reasonable suppression of the DETC luminescence and the depletion laser signal is possible at repetition rates of up to 1 MHz due to the limited switching times of the acousto-optic modulator. The maximum contrast of the latter also limits background suppression, in this case to a suppression ratio of approximately  $1 : 10^3$ .

Unfortunately, this approach turned out to have further limitations. Namely, due to the spectral overlapping, the UCNPs induce DETC fluorescence themselves, most likely via Förster resonant energy transfer (FRET), which can not be subtracted as a background due to its slightly different spectral shape as compared to the two-photon induced DETC luminescence. Moreover, the depletion laser slightly changes the UCNP luminescence as well (most likely by excited state absorption), so that these spectra cannot be taken as indicators for the local temperature.

### Core-shell UCNPs

The FRET-effect can be suppressed by using UCNPs with a rare-earth doped core and a silica shell, which acts as an inactive spacer layer. The UCNP cores were synthesized as previously explained and coated by a 10 nm thick silica shell along the lines of the process described in [108].<sup>2</sup> However, for particles with sufficiently thick silica shell (10 nm – 20 nm), also the overall magnitude of the fluorescence is drastically reduced at similar volume filling fractions of the UCNPs in the photo-resist, and therefore, once again, the signal-to-background ratio is insufficient for a reasonable temperature measurement.

### Choosing the UCNP fluorescence band

So far, temperature measurements on the basis of the UCNP luminescence were based on the green fluorescence band, where the background through the DETC fluorescence is obviously large. However, also the relative magnitude of the two peaks in the red spectral region shows a (albeit smaller) temperature dependence (**Figure 4.5 a**), and hence, this fluorescence band can be used for the luminescence detection as well. As in the latter case, we observe a small, but still perturbing FRET-effect for the nanoparticles without shell (i.e., a

---

<sup>2</sup> Particle synthesis and analysis through transmission electron microscopy by J. Mange and T. Nann.

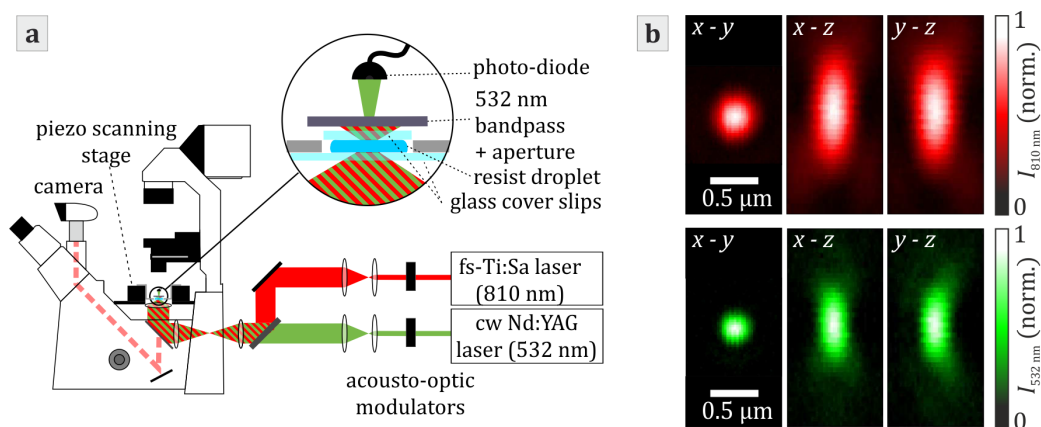
background luminescence by the DETC in the red spectral region, which is induced by the presence of excited UCNPs).

Hence, a combination of all of the approaches mentioned above was used for the measurement presented in Section 5.2.1. I.e., the measurement was performed with UCNPs with a silica shell (**Figure 4.5 b**) in combination with the time-gating approach and the measurement the red UCNP fluorescence band. Furthermore, we are interested in possible thermal effects due to the depletion laser in STED-DLW. Therefore, an additional frequency-doubled fiber master-oscillator power-amplifier laser was coaligned with the writing laser, emitting at 532 nm wavelength (*LDH-P-FA-530XL, Picoquant*). The beam diameter of this depletion laser is reduced to yield a Gaussian focus with a diameter of 400 nm (FWHM). Thereby, the depletion laser intensity is relatively homogeneous within the reaction volume to keep the interpretation simple.

Despite this experimental effort, the results should be interpreted with care. In the case of a non-fluorescent photo-initiator, we indeed measured a temperature change due to monomer explosions in the overexposure regime as will be discussed in Section 5.2. This is taken as an indicator that the temperature measurement indeed works, even though no significant heating is detected below the overexposure threshold. However, in the case of DETC, the spectrum is dominated by a substantial increase and broadening of the 670 nm-peak in the case of monomer explosions. This increase cannot be explained by a thermal occupation of the underlying states in the sense of an underlying distribution corresponding to a Boltzmann-factor behavior, with the simple reason that it would correspond to cooling instead of heating. The results of these experiments will be presented and discussed in Section 5.2.1.

## 4.2 Optical Polymerization Detection

As already discussed, it is sometimes argued that polymerization would occur primarily after the exposure (post-polymerization) due to the exposure being very short (typically in the millisecond regime) [16, 57, 94]. In order to verify this post-polymerization assumption (Section 3.3.6), it is necessary to resolve the kinetics of the polymerization process. However, as discussed, the standard methods lack the necessary spatial or temporal resolution to detect the polymerization in small volumes and on the (interesting) timescale of milliseconds or less. For this reason, an indirect method has recently been presented that allows for detecting the refractive-index change resulting from



**Figure 4.6:** a) Extended DLW setup for the measurement of the progress of the polymerization reaction. The forward scattered light of an additional continuous wave probe laser through the sample is collected with a photo-diode and taken as time-dependent signal. b) Measured cuts of the foci of the writing laser (top row) and the probe laser (bottom row). Reproduced from [110]. ©2014 Wiley VCH.

the polymerization [109]. Even though this method is not sensitive to specific chemical changes, it allows to estimate the overall reaction progress and the reaction duration under different excitation conditions. It is based on the fact that the voxel formation leads to a local change in refractive index and, hence, to a change in transmission of a probe laser. Thereby, the ongoing polymerization reaction can be detected with good spatial and temporal resolution. In this section, the method as such as well as its working principle will be described in detail.

While in the original publication [109], the writing laser was at the same time used as probe laser, we use a different probe laser (532 nm wavelength, cw) in order to be able to measure also when the writing laser is switched off [110]. The corresponding setup also includes a photo-diode to detect forward-scattered light with a well-defined, relatively small solid angle (**Figure 4.6**). In order to yield a maximal signal, the foci of the probe laser and the writing laser have to be co-aligned carefully using the gold-bead scanning technique.

The refractive index of typical uncured monomers like PETA and PETTA is around  $n_0 \approx 1.49$ .<sup>3</sup> In the case of film curing, it increases by approximately 2% during polymerization [111]. Even though the latter value may be slightly different in the case of DLW due to a different monomer conversion, a refractive index change is clearly visible in the microscope camera of the DLW setup. Hence, the formation of a solid voxel also results in scattering of the probe laser light. Typically, the detector signal  $I$  decreases by approximately 1% during voxel formation, corresponding to a relative scattering signal of  $S = (I/I_0 - 1) = -0.01$ . Corresponding experiments for a large set of different photo-resists are presented in Section 6.2.

The physical origin of this scattering signal is not trivial, though. First, the illumination conditions are far away from plane waves or a simple Gaussian plane wave as one would expect in paraxial optics due to the high numerical aperture objective lens. In particular, the numerical calculations of the scattered field shown below reveal that the phase is not at all constant on the downstream side of the focus. Therefore, the probe focus itself cannot easily be described by a Gaussian beam.

Second, the size of the forming polymer voxel is roughly on the same length scale as the probe wavelength. Therefore, in a strict sense, neither the approximation of geometrical optics is valid, nor is it the opposite approximation of a small (point-like) scatterer. In order to determine the qualitative behavior, one may still be tempted to rely on these two extremal cases. In the case of geometrical optics, one would interpret the polymer voxel as a lens. However, this interpretation is misleading as the voxel position is in the focal plane of the objective lens. Hence, in the (thin) lens picture, it should not lead to any alteration of the probe beam. As in the experiment, we do see such an alteration, the effect therefore originates from the deviations from the thin lens approximation. On the contrary side, a small and isotropic scatterer emits spherical waves regardless of its refractive index and independent on the direction of the incoming wave by which it is excited.

As a last point, one should note that the opening angle of the detector is small compared to the numerical aperture of the illumination, which is the inverse of what is typically used for scattering experiments (plane-wave excitation and wide-angle detection). If the scatterer was excited by a plane wave propagating in axial direction, the detector signal would always decrease due to light being scattered away from the axis, corresponding to a negative scattering signal  $S$

---

<sup>3</sup> For readily mixed photo-resists including a photo-initiator in typical concentrations, the refractive index may be slightly increased ( $\approx 1\%$ ) compared to the pure monomer [111].

in our convention. However, as already mentioned, our probe beam has a large incidence angle while the detection angle is small. Therefore, off-axis spatial frequency components of the incident light will contribute to the scattering signal onto the detector, even though without a scatterer, they would not contribute to the detector signal.

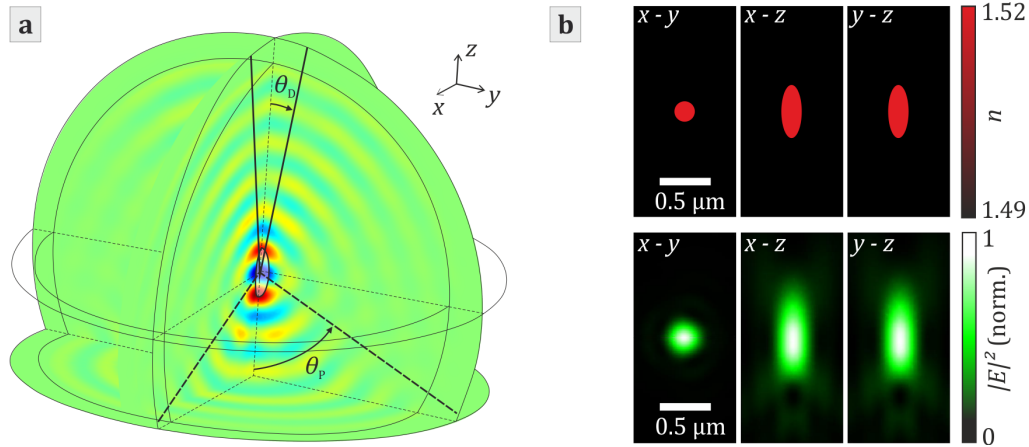
In the end, all of these contributions will interfere with the original field and the sign of the measured signal will depend on the relative phase of the scattered wave. More precisely, if the refractive index of the voxel is larger than the surrounding, its polarizability will be positive, whereas if the refractive index is smaller, it will get negative. As this change in sign corresponds to a  $\pi$ -phase shift, the scattered signal is supposed to also change its sign. We also tried to perform experiments in a “pseudo dark-field” configuration, where the central part of the photo diode is blocked and only light scattered under larger angles will be detected. In that case, positive rather than negative scattering signals are observed. However, the overall signal-to-background ratio is decreased in that case. This observation points out the fact that, if the solid angle for the detection is chosen too large, partial signals may cancel due to the spatial integration.

#### Numerical Calculation of the Scattering Signal

We tested our understanding of the origin of the scattered signal by performing numerical calculations of the experimental setting on the basis of the fully vectorial field equations. The scattering field is calculated through the Electromagnetic Module in *COMSOL Multiphysics*<sup>®</sup> (BiCGStab solver, maximum mesh element size: probe wavelength/6, approximately  $6 \cdot 10^6$  degrees of freedom).<sup>4</sup> The model includes an ellipsoidal voxel with refractive index  $n$ , lateral diameter  $d$  and axial length  $h = 2.6d$ , embedded in an environment with the refractive index  $n_0 = 1.49$  (**Figure 4.7 a**). The probe beam is modelled as a circularly polarized focus with a numerical aperture of  $NA = 1.4$  using a vector Debye approach following [86]. The resulting complex vectorial field distribution is fed to the *COMSOL* model as a boundary condition on the input plane ( $z = -1 \mu\text{m}$ ) of the model geometry (**Figure 4.7 b**). In order to avoid back-scattered partial waves, the remaining boundaries of the modeling volume are implemented as Perfectly Matched Layers.

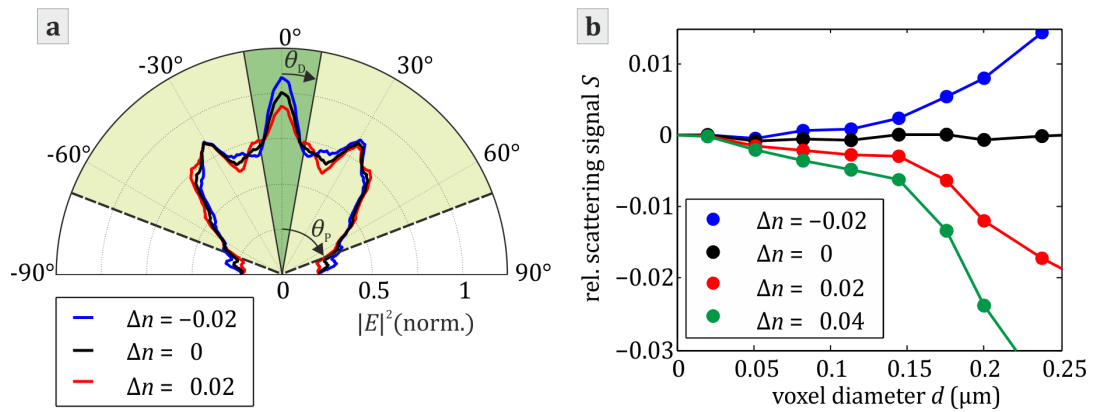
---

<sup>4</sup> Numerical modelling by M. Kadic.



**Figure 4.7:** **a)** Geometry of the numerical model together with the modulus of the electric field vector. The nominal opening angle of the probe beam ( $\theta_P = 69^\circ$ ) and the detector ( $\theta_D = 10^\circ$ ) are drawn as well for better orientation. A typical voxel ( $\Delta n = 0.02$ ,  $d = 200$  nm) is positioned in the center of the focus. **b)** Refractive index distribution of the same typical voxel (top row) and calculated intensity of the probe beam in the reference case (bottom row). Reproduced from [110]. ©2014 Wiley VCH.

The modeling geometry is presented in **Figure 4.7 a** together with a typical calculated electric field distribution. The calculated intensity distribution (**Figure 4.7 b**) of the obtained focus in the numerical model in the reference case (no voxel) is in good agreement with the experimental situation (**Figure 4.6**). As discussed in the previous section, the interference of the probe beam with the scattered field leads to a decreased intensity in forward direction if the refractive index of the voxel is higher than within the surrounding (and vice versa). For off-axis directions however, the intensity is increased at the same time as described in the previous section (**Figure 4.8 a**). In order to calculate the scattered signal corresponding to the experimentally measured value, the squared electric field on the boundary of the modeling volume is associated with the far field and integrated over the solid angle covered by the detector in the experiment (**Figure 4.8 b**). While in the ideal case, the reference signal without a voxel ( $n = n_0$ ) should be strictly zero, we observe a small scatter on the calculated data due to meshing artefacts.



**Figure 4.8:** **a)** Scattered field distribution (squared electric field on the boundary of the computation volume) as a function of the scattering angle. The shaded areas indicate the solid angles of the detector and the probe beam ( $\theta_D$  and  $\theta_P$ , respectively). **b)** Calculated scattering signal  $S$  (integrated scattered field over the detector solid angle). For a typical voxel diameter and refractive index ( $\Delta n = 0.02$ ,  $d = 200$  nm), we calculate a scattering signal in the order of  $S = -0.01$ , which corresponds to characteristic experimental values. Reproduced from [110]. ©2014 Wiley VCH.



# 5 Chapter 5

---

## 5 Initiation Mechanisms

As discussed in Section 3.3.6, photo-polymerization can often be discussed as a reaction with two independent steps. Within this chapter, experiments will be discussed that allow for conclusions concerning the first reaction step in the context of DLW, namely the initiation of starting radicals.

### 5.1 Absorption Mechanisms

One parameter study that turns out to be particularly insightful is the variation of the laser repetition rate, as it gives a relatively direct insight into the mechanism of radical generation. Namely, as the polymerization reaction is typically slow compared to relevant pulse repetition rates, it will only depend on the “average” rate of radical generation. Therefore, one can determine the nonlinearity of the optical absorption process involved in the radical generation mechanism by comparing the polymerization threshold power to the repetition rate according to Equation (3.5). Two-photon absorption is often referred to as the dominant absorption mechanism for multi-photon polymerization in the literature. However, we find that different mechanisms may dominate the radical generation for the different DLW schemes, depending on the experimental conditions (i.e., laser wavelength, pulse duration and repetition rate, and photo-initiator species). Hence, for choosing appropriate laser sources, photo-resists or when working on super-resolution DLW schemes, knowledge of the actual mechanism and reaction pathway is essential.

Experimentally, the easiest approach to access the absorption nonlinearity would be to vary the exposure period. However, this may not only influence radical formation, but also the polymerization reaction itself, if the polymerization sets

on already during the exposure, and hence, radical formation and polymerization cannot be considered as temporally separated processes anymore. In other words, the post-polymerization assumption may then not be justified, which indeed is the case, as we will discuss in Section 6.1.1. Still, such experiments have been done in the past [39]. As discussed by these authors, the interpretation and modeling of their results with respect to the absorption mechanisms is not straightforward. Yet, it turned out that the variation of exposure dose and writing velocity can lead to valuable insights into the kinetics of the polymerization reaction once the initiation mechanism is clarified. The corresponding experiments will therefore be discussed in Section 6.1.1 and Section 7.2, respectively.

In principle, one could also change the threshold dose by varying the photo-resist composition, i.e., by changing the concentration of photo-initiator or some inhibiting species. However, once again, this may lead to qualitatively different reaction conditions for the polymerization reaction and, hence, results that are non-trivial to interpret. The corresponding experiments are presented in Section 7.1.

For these reasons, the variation of the laser repetition rate turns out to be the most insightful experiment. While, in principle, the reaction conditions for the polymerization may depend on the number of pulses that impinge on a certain area during the exposure period, the time between two subsequent pulses usually is small compared to both the exposure period and the polymerization duration. In the case of the maximum repetition rate (80 MHz), one voxel is typically exposed to approximately 26,400 pulses (exposure period  $t_{\text{exp}} = 3.3$  ms, corresponding to  $v = 100$   $\mu\text{m/s}$  and  $x = 330$  nm). As discussed in Section 6.2, the (measured) “intrinsic” polymerization duration for short exposures is in the order of 0.3 milliseconds. Hence, the radical generation can still be assumed to be quasi-constant with respect to the polymerization reaction for repetition rates that are larger than 3 kHz.

Experimentally, the variation of the repetition rate is preferentially done by using a so-called “pulse-picker” in combination with a Titanium:sapphire oscillator (80 MHz) with a pulse energy that is large enough to still write at low repetition rates (Chameleon-Setup, Section 2.1). In this case, other process parameters such as the excitation wavelength, mode profile and the pulse duration do not change, allowing for high comparability of the results. The division ratio can be varied over many orders of magnitude, so that any repetition rate according to  $R = 80 \text{ MHz}/n$  with  $n \in \mathbb{N}$  can be set. In

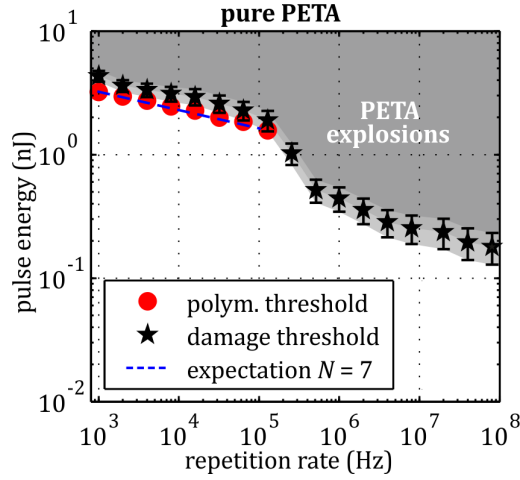
practice, a lower limit for the repetition rate is given by the laser power that is initially available, which for the described experimental setting allows to write structures for repetition rates down to the kHz-regime. However, this still means that the repetition rate can be varied by factors of  $10^4$  or  $10^5$ , so that an interpretation of the logarithmic Equation (3.5) indeed is meaningful. The pulse picker achieves a maximum suppression of the pulse energy down to 0.2% of the initial value.<sup>1</sup> Therefore, at a repetition rate of 1 kHz, the accumulated average power of the 80.000 “suppressed” pulses would still be larger by a factor of 160 as compared to the average power of the “desired” pulses. As this could possibly favor parasitic (one-photon) absorption channels, the pulse energy is further diminished using the acousto-optical modulator in the writing setup at these very low repetition rates.

A similar experiment has been performed in the past by another group, using picosecond lasers with tunable pulse duration (8 ps – 25 ps) and repetition rate (0.2 MHz – 1 MHz) [32]. However, these numerical values are a priori quite different from typical experimental settings as described within this thesis and, more importantly, they offer only a narrow variation window, which, at least in case of super-linear processes, may not be very indicative. According to the authors of this publication, it is furthermore assumed that the photo-resist can be treated as a semi-conductor in terms of its absorption behavior, with the size of the band-gap corresponding to the  $S_0$ - $S_1$  energy difference [31, 32]. As the latter is an electronic excitation of the bound electrons of a single molecule rather than an optical interband excitation, we consider this description and the authors’ conclusions to be highly questionable.

In order to measure the polymerization threshold in our experiments, lines are written with a writing velocity of 100  $\mu\text{m/s}$ . The polymerization threshold is then defined as the lowest writing laser average power (or pulse energy), for which written structures withstand the washing process during sample development (15 minutes in isopropanol followed by rinsing with acetone and de-ionized water), judged by a light-microscope image in dark-field mode. Even though this transition is not perfectly step-like, one can compare structures that look similar as long as the experimental setting (e.g., illumination and imaging parameters) are not changed.

---

<sup>1</sup> For pulses directly before or after a “desired” pulse, the suppression is slightly worse (1.2%).



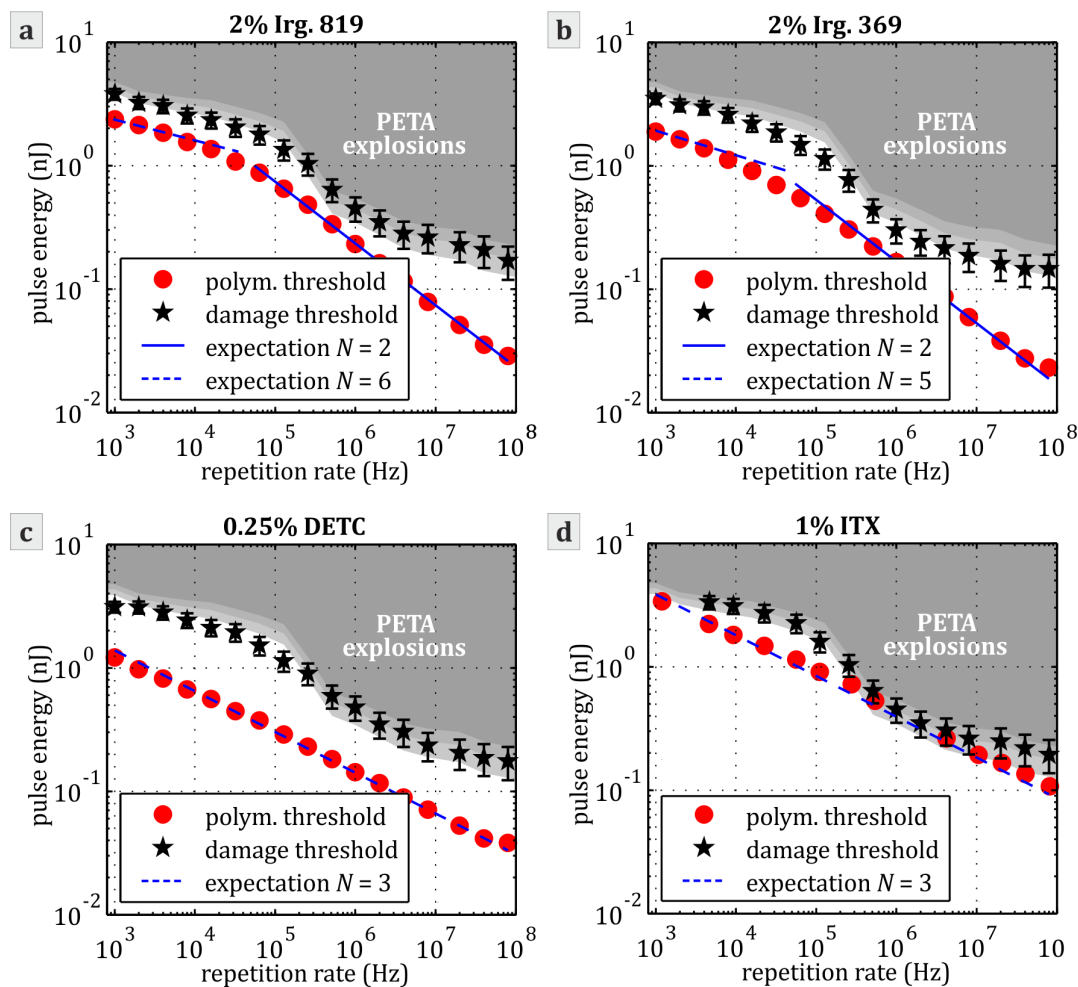
**Figure 5.1:** Threshold pulse energies for polymerization as well as for overexposure for the pure monomer PETA. As the micro-explosions indicating overexposure do not occur deterministically, a typical statistical error is indicated. As a guide to the eye, straight lines with slopes corresponding to the estimated nonlinearity for MPI ( $N = 7$ ) is depicted where writing is possible and, hence, MPI appears plausible.

We studied five different photo-resists based on PETA containing either no photo-initiator, 2% (wt.) of either of the commercial photo-initiators Irgacure 369 and Irgacure 819, 0.25% (wt.) of DETC, or 1% (wt.) of ITX. The experimental results are summarized in **Figure 5.1** and **Figure 5.2**.<sup>2</sup> The threshold for structural damage through micro-explosions is indicated in addition to the polymerization threshold pulse energy. In order for the result to be meaningful, the repetition rate is varied over five orders of magnitude.

### 5.1.1 Absorption Mechanisms for Polymerization

In the classical model of two-photon absorption ( $N = 2$ ), one would expect the data points to follow straight lines with slope  $-1/N = -1/2$  according to Equation (3.5). This indeed seems to be the case for the Irgacure photo-initiators for relatively high repetition rates (**Figure 5.2**, top row). For a repetition rate  $R \lesssim 100$  kHz, however, a different mechanism with an effective nonlinearity that is clearly higher than 2 dominates the overall behavior and overcomes

<sup>2</sup> Experiments partly conducted by J. Fischer and published in [16].



**Figure 5.2:** Threshold pulse energies for polymerization as well as for overexposure for photo-resists that contain the monomer PETA as well as **a)** 2% (wt.) of Irgacure 819, **b)** 2% (wt.) of Irgacure 369, **c)** 0.25% (wt.) of DETC, and **d)** 1% (wt.) of ITX as photo-initiator. The shadowed areas mark the overexposure threshold for the pure monomer in all panels for better comparison. As a guide to the eye, straight lines with slopes corresponding to the estimated nonlinearities for TPA ( $N = 2$ ), MPI ( $N = 5$  and  $N = 6$ ), and TPA followed by excited-state absorption ( $N = 3$ ) are depicted where these processes appear plausible.

the two-photon absorption process. Interestingly, DLW is also possible within the pure photo-resist without any photo-initiator if low repetition rates are applied ( $R \lesssim 100$  kHz), albeit at higher pulse energies (**Figure 5.1**). As the monomer absorption at half the excitation wavelength is virtually zero, two-photon absorption does not occur at all in this case. The nonlinearity is even larger than with a commercial photo-initiator at the corresponding repetition rates. For DETC and ITX, in contrast, the nonlinearity seems to follow  $N = 3$  throughout the examined regime (**Figure 5.2**, bottom row).

While the interpretation of the  $N = 2$  – regime along the lines of the often-cited two-photon absorption mechanism is relatively straightforward, this is not the case for the observed regimes with higher nonlinearity. As discussed in Section 3.1, radical generation may as well be triggered by multi-photon ionization (potentially followed by avalanche generation) or two-photon excitation followed by an additional excited-state absorption step. In the first case, the nonlinearity can be estimated by the computed ionization energies of the corresponding molecules (Section 3.1.2). Even if plasma formation through avalanche generation is included, one can expect the observed nonlinearity to be determined by the initial ionization step, which is still necessary as the seeding mechanism. The corresponding photon numbers as well as their integer equivalents for PETA, Irgacure 369 and 819, and DETC are recapitulated in Table 5.1 and displayed in **Figure 5.1** and **Figure 5.2** for comparison. To our understanding, the possibility to induce polymerization without any photo-initiator indicates that the corresponding absorption process is not very selective in the sense that it requires specific chemical properties of the initiating species, which is consistent with photo-ionization.

In the second case ( $N = 3$ ), one may speculate that an additional excited-state absorption process in addition to 2PA is required. However, the effective nonlinearity will then only be altered by this second step, if this process does not saturate at the given pulse energies. Only then does the effective nonlinearity correspond to the overall number of absorbed photons. As discussed in Section 3.1.3, radical generation from Norrish type II photo-initiators such as DETC and ITX most likely requires such an excited-state absorption process to trigger the radical formation from the triplet state if no co-initiator is present. As such absorption processes from the triplet state (e.g.,  $T_1 - T_n$ ) may be triggered by one 800 nm-photon in this case [20], it seems plausible that the observed effective nonlinearity of  $N = 3$  occurs indeed due to a two-step absorption reaction pathway.

	<b>S<sub>0</sub>-S<sub>1</sub></b> photon number	<b>ionization</b> photon number	<b>high <i>R</i></b> $\gtrsim 100$ kHz	<b>low <i>R</i></b> $\lesssim 50$ kHz
<b>PETA</b>	3.1	6.9	-	6
<b>Irg. 369</b>	2.5	5.1	2	5
<b>Irg. 819</b>	2.1	5.6	2	6
<b>DETC</b>	2	5.1	3	3
<b>ITX</b>		5.1	3	3

**Table 5.1:** Calculated photon numbers for absorption through the S<sub>0</sub>-S<sub>1</sub> transition and photo-ionization (Section 3.1.2, [16]) and the nonlinearity  $N$  indicated with the experimental data (**Figure 5.2**). While the peak intensity of the S<sub>0</sub>-S<sub>1</sub> transition is typically observed at wavelengths smaller than half the excitation wavelength (and, hence, the corresponding photon number is larger than two), these absorption peaks are relatively broad and therefore still non-zero at this wavelength. Also, the computations for both cases do not include solvent effects, which could possibly lead to red-shifted spectra. Please note that ITX is not contained in the computational study in [16], and hence, calculated photon numbers are not available.

While we consider the above-mentioned interpretations to be the most plausible ones, other process pathways can be imagined as well (see also Section 3.1). In order to distinguish these mechanisms more clearly, additional experiments have to be performed. For DETC, we conducted optical fluorescence spectroscopy experiments (Section 5.3.1), which reveal that indeed, the S<sub>0</sub> - S<sub>1</sub> can be triggered by two-photon absorption ( $N = 2$ , compared to  $N = 3$  for DLW). Furthermore, we measured the actual local heating in order to see whether photo-thermal processes are involved in the DLW pathway that possibly lead to unwanted side effects such as changes in the photo-chemical properties (Section 5.2). In addition, other effects such as saturation of the absorbing species or interaction of excited states (such as avalanche formation in the case of MPI) may influence the observed nonlinearity and alter it from the “pure” nonlinearity of the absorption process itself.

### 5.1.2 Absorption Mechanisms for Overexposure

In contrast to the polymerization threshold, the threshold for the occurrence of micro-explosions is not very well-defined. Also, we find that it is very similar for all photo-resists, both qualitatively and quantitatively (**Figure 5.2**). To our

understanding, this indicates that the overexposure mechanism is essentially the same in all cases. While for low repetition rates, we find the same nonlinearity as for writing in pure PETA, there is a relatively large step at frequencies around 250 kHz, where the overexposure threshold decreases tremendously towards high repetition rates. For larger repetition rates, the nonlinearity is once again increased, however, going along with increasing statistical scatter.

This behavior can partly be understood if over-exposure damage is assumed to be a thermal process. In that case, heat conduction leads to cooling of the writing volume between two subsequent pulses at low repetition rates. In contrast, at repetition rates in the MHz-regime, heat deposited by subsequent pulses accumulates, resulting in a lowered damage threshold pulse energy (Section 3.3.4). While this in principal explains the step-like behavior at medium frequencies ( $\approx 100 - 500$  kHz), we expect this transition to occur at repetition rates more in the 2 MHz-range from our numerical calculations (Section 3.3.4). The reason for this discrepancy is not perfectly clear at the current stage. One possible cause could be the fact that during our DLW experiments, lines are written instead of isolated dots, and hence, heat from adjacent voxels partly accumulates. In other words, the effective “thermally relevant” exposure period is enlarged due to conductive cooling. While this effect in principal points into the right direction, a numerical modeling is computationally demanding and hence, out of the scope of this work.

Also, from such a model, we would expect to see no repetition rate dependency of the overexposure threshold at all for low repetition rates, where the peak temperature is largely given by the temperature increase due to one single pulse. The fact that in the experiment, we do see such an effect clearly indicates that “something” other than heat “survives” from one pulse to the next even in the few kHz-regime. A first candidate is obviously the solid polymer, which is formed even without photo-initiator at these repetition rates. As the solidification already occurs as a consequence of very few pulses, it may influence the thermal and photo-chemical material parameters and thereby lead to a reduction of the threshold value for thermal damage.

As will be discussed in Section 5.2, we can show experimentally that overexposure indeed goes along with a pronounced local heating of up to several hundred Kelvin, leading to the evaporation of the monomer (micro-explosions). However, it is not completely clear at this stage whether these thermal effects are a cause or rather a consequence of the overexposure.



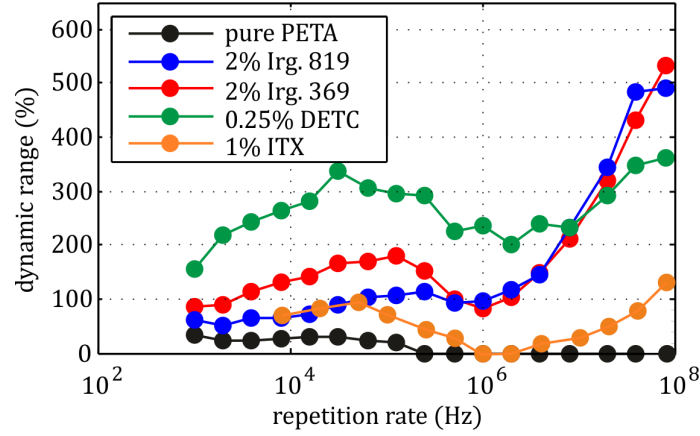
Interestingly, we find that the nonlinearity of the micro-explosion threshold is the same as for polymerization in the pure monomer at low repetition rates. This suggests that the underlying mechanisms could be the same as well, with a prominent candidate being multi-photon ionization (MPI) as discussed in Section 3.1.2. Alternatively, additional absorption mechanisms could be enabled by the polymerization reaction itself, e.g., through the generation of absorbing species during the reaction. In both cases, the interpretation would be as follows: MPI generates radicals, but also leads to sample heating in the one or the other way. At low repetition rates, the writing area cools down in between two pulses. However, at high repetition rates, the temperature increase is much more pronounced at similar rates of radical generation due to the less pronounced cooling process. Thus, micro-explosions occur already below the threshold for structure formation and hence, DLW is not possible. By adding a photo-initiator, the efficiency of the writing process can be greatly improved and hence, writing is possible at all repetition rates and with lower laser powers.

In summary, we find that two-photon absorption indeed seems to be the radical formation mechanism in many cases. However, when using low-repetition rate writing lasers or unconventional photo-initiator systems, other processes such as photo-ionization or excited-state absorption become dominant. Despite or in some cases also because of their unconventional behavior, these more exotic DLW schemes may be of high interest for special applications that require DLW without the use of a photo-initiator or super-resolution writing schemes such as STED-DLW.

### 5.1.3 Influence on the DLW Process

#### 5.1.3.1 Dynamic Range

While for the determination of the underlying mechanisms the scaling of writing threshold and overexposure threshold are essential, an often more important quantity for applications is the so-called dynamic range. It is defined as the relative difference of the thresholds for overexposure and polymerization ( $E_{p, \text{overexposure}}/E_{p, \text{polymerization}} - 1$ ). In practice, it indicates the size of the “operational window” where structuring is possible. As can be seen in **Figure 5.3**, the dynamic range for PETA is relatively small at low repetition rates ( $\approx 20\%$ ) and goes to zero for higher repetition rates (no structuring possible). For the Irgacure photo-initiators, we find values in the order of 100 – 150% at low repetition rates, while towards high repetition rates, the dynamic range is drastically increased to almost 500% with a local minimum at around 1 MHz.



**Figure 5.3:** Dynamic range (relative difference of overexposure and polymerization threshold) for the examined set of photo-resists.

For DETC and ITX, the behavior is qualitatively similar. In principle, one might expect that a high photo-initiator concentration goes along with a large dynamic range, as the writing threshold is connected to the photo-initiator while the overexposure threshold is not. However, the initiation efficiency may differ for the different photo-initiator species. In the experiment, we observe that, even though the concentration of DETC is smallest within the examined set of photo-resists, this photo-resist is the most efficient one and offers the largest dynamic range (200 % – 350 %). For ITX, writing is challenging or even impossible at medium repetition rates in the 1 MHz regime due to the vanishing dynamic range at the given concentration.

### 5.1.3.2 3D-Resolution

While the threshold pulse energies for polymerization and overexposure allow to draw conclusions on the underlying mechanisms, it is also highly interesting to see whether the observed different mechanisms actually do influence not only the writing threshold, but also the achievable structure quality, or more precisely, the achievable resolution. From theory, one expects that the resolution scales with the process nonlinearity  $N$  according to  $a_{\min} \propto \frac{1}{\sqrt{N}}$  (Section 3.3.2). For the writing of woodpile photonic crystals which are often used as benchmark structures, the critical distance with respect to writing resolution is the axial rod separation corresponds to  $3c/4$ , where  $c$  is the axial extent of the tetragonal unit cell, which includes 4 single layers of rods [17]. Comparing this value to the

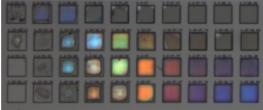
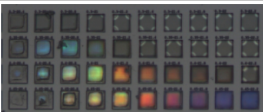

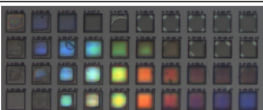
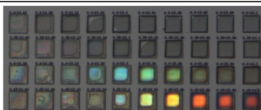



above-mentioned condition for  $a_z$ , we can calculate the expected minimal rod spacing for which DLW still yields open and fully resolved woodpile structures:

$$a_{\min} = \frac{2}{3} \frac{\lambda r_{\text{aspect}}}{s \text{NA} \sqrt{2N}}. \quad (5.1)$$

In this equation,  $r_{\text{aspect}} = \text{FWHM}_z / \text{FWHM}_{xy}$  is the aspect ratio of the writing volume, which is given by the relevant iso-intensity surface of the writing laser focus (typically,  $r_{\text{aspect}} = 2.5$  for high-NA objective lenses), and  $s = 1.28$  is an empirically determined factor that is introduced to pre-compensate for structure shrinkage during the sample development step. The question whether the effective process nonlinearity is indeed connected to the writing resolution in this way can be answered by writing woodpile photonic crystals with different rod spacings under different writing conditions. Namely, we wrote woodpiles with rod distances from 300 nm to 450 nm with varying writing power into the four previously examined photo-resists at three selected repetition rates (4 kHz, 1 MHz, 80 MHz) in order to cover the different writing regimes. All samples are written into different droplets on the exact same substrate in order to avoid accidental differences in sample treatment.

Real-color dark-field mode optical micrographs of all structures can be found in **Figure 5.4**. In this measurement configuration, the woodpile structures appear colorful due to Bragg-reflections through their layered structure (or, equivalently, the existence of a photonic stop-band). As the rod diameter and hence, the overall filling fraction of polymer compared to air increases with increasing power, the corresponding vacuum wavelength of this stop-band also increases and hence, the observed color spectrum changes. As Bragg-reflections only occur for open structures that feature a certain periodicity, the appearance of colors and the accessible color range for a certain rod distance can be used as indicators whether the corresponding structures are still fully resolved.

While structuring works well both, at low (4 kHz) and high (80 MHz) repetition rates for the sensitized resists, DLW at medium repetition rates (1 MHz) is more difficult. While writing small features is still possible (**Figure 5.2**), compact, three-dimensional structures are not feasible due to the occasional occurrence of micro-explosions except for DETC, leading to sample deterioration. At low repetition rates, the pure monomer and the commercial photo-initiator Irgacure 819 yield similar and very good results. DETC should be preferred at high repetition rates.

		4 kHz	1 MHz	80 MHz
<b>pure PETA</b>	300 nm		(no structuring)	(no structuring)
	350 nm			
	400 nm			
	450 nm			
<b>2% Irg. 369</b>	300 nm		(no structuring)	
	350 nm			
	400 nm			
	450 nm			
<b>2% Irg. 819</b>	300 nm		(no structuring)	
	350 nm			
	400 nm			
	450 nm			
<b>0.25% DETC</b>	300 nm			
	350 nm			
	400 nm			
	450 nm			

**Figure 5.4:** Dark-field mode optical micrographs (real color) of photonic woodpile structures written into the different photo-resists (footprint:  $20\ \mu\text{m} \times 20\ \mu\text{m}$ , height: 24 single layers or, equivalently, 6 tetragonal unit cells). From left to right, the relative writing power changes in steps of 1%. The actual power variation range is larger than depicted with a base value that was selected relative to the writing threshold for each set of parameters. The colorful appearance is caused by Bragg-reflections and hence, indicates “open” and fully resolved structures.

In order to quantify the general trends, we calculated the expected minimum rod distance according to Equation (5.1) for the different cases (different  $N$ ) and compared it to the experimental result (Table 5.2). Even though the experimental data do not represent a one-to-one correspondence of the expected values, the general trend is maintained. Namely, processes with high nonlinearity  $N$  in general also feature better writing resolution. As our setup is relatively well characterized in terms of the employed optics (deviations of the measured focus diameter compared to the numerically computed values are less than 10%), we believe these differences to originate in the photo-chemistry of the process. More precisely, the theoretical formula is based on a threshold model, where a fully digital (and local) transition from liquid to solid photo-resist is assumed.

In practice, the threshold power is probably more a “smeared-out” power range. Also, effects as molecular diffusion of reacting species may deteriorate the observed writing resolution.

**Table 5.2:** Comparison of the expected resolution  $a_{\min}$  (rod distance) according to the extended multi-photon resolution criterion (Equation (5.1)) and experimental values  $a_{\exp}$  (**Figure 5.4**).

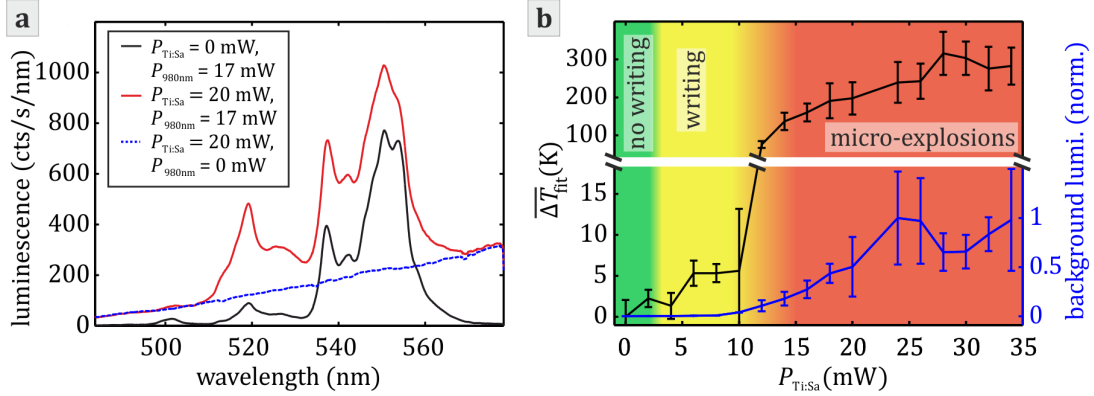
	4 kHz			1 MHz			80 MHz		
	$N$	$a_{\min}$ (nm)	$a_{\exp}$ (nm)	$N$	$a_{\min}$ (nm)	$a_{\exp}$ (nm)	$N$	$a_{\min}$ (nm)	$a_{\exp}$ (nm)
<b>pure PETA</b>	7	200	350	-	-	-	-	-	-
<b>2% Irg. 369</b>	5	235	350	2	370	-	2	370	400
<b>2% Irg. 819</b>	6	215	300	3	305	-	2	370	400
<b>0.25% DETC</b>	3	305	350	3	305	350	3	305	350

## 5.2 Local Heating

While the scaling of the writing threshold with the repetition rate can be well explained by the above-mentioned mechanisms, we find that it is difficult to construct models that quantitatively predict the scaling of the writing threshold with the writing velocity or the photo-initiator content [39] (see also Section 7.1 and Section 7.2). It has been speculated that local heating could influence the writing process, even if the radical generation itself is not a thermal process as indicated by the results presented in the previous chapter. In addition, as described in the last section, there are hints that it is a thermal process that leads to micro-explosions in the overexposure regime. A more detailed analysis of the thermal effects during DLW seems highly desirable.

However, as already mentioned, it is hard to estimate the magnitude of local heating effects as the relevant heat sources are largely unknown. Furthermore, most experimental techniques for thermo-probing are not applicable as they would either interfere with the writing process or not be able to yield the spatial resolution necessary to resolve temperature distributions with dimensions on the sub-micron scale. We therefore developed and applied an unconventional approach that is based on the detection of the luminescence of upconverting nanoparticles.<sup>3</sup> The experimental setup is described in detail in Section 4.1 and offers the possibility to detect temperature changes in the 1 K-range with diffraction limited spatial resolution without influencing the DLW process.

<sup>3</sup> Experiments partly published in [94].



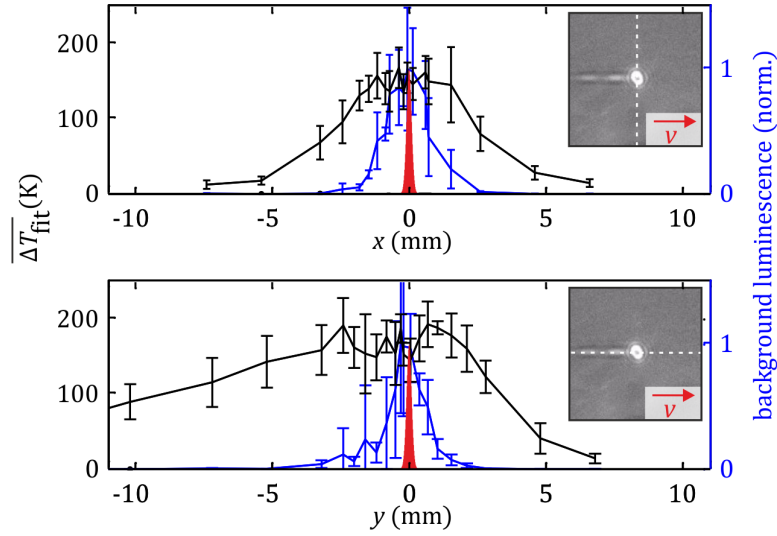
**Figure 5.5:** **a)** Measured spectra of the photo-resist with the dispersed nanoparticles for selected laser powers. A writing laser power of 20 mW is chosen, which is well above the damage threshold of the photo-resist. However, spectra taken at a laser power below the damage threshold cannot be distinguished from the reference spectrum in this representation due to the small temperature difference in that case. As for the calibration measurement, the relative peak height of the nanoparticle spectrum changes. However, a broadband background luminescence is observed in addition. As the latter is not linked to the nanoparticle excitation, it can be subtracted by reference measurements without nanoparticle excitation. (For comparison:  $P_{\text{Ti:Sa}} = 20$  mW correspond to  $E_p = 0.25$  nJ at 80 MHz). **b)** Measured average temperature according to the calibration curve Equation (4.1) and integrated broadband background luminescence (integration time: 10 s) as a function of the writing laser power for one selected repetition rate (80 MHz). While in the polymerization regime, a temperature increase of only 5 K or even less is observed, micro-explosions in the overexposure regime go along with a strong temperature increase and a broadband background luminescence. Reproduced from [94]. ©2013, AIP Publishing LLC.

Experimentally, we find that the local heating is small for a standard DLW scheme (80 MHz) with a typical photo-resist (PETA with 1% (mol) of Ir-gacure 819). I.e., relative temperature changes of below 5 K are observed in this case unless the photo-resist is overexposed (**Figure 5.5**). In the latter case, a pronounced temperature increase by several hundred Kelvin goes along with bubble formation and bad structure quality, indicating that the peak temperature is higher than the vaporization temperature of the monomer ( $T_{\text{boil}} = 428 \pm 45^\circ\text{C}$ , [112]). Please note that the calibration curve for extracting the actual temperature from the measured spectra only covers the range from room temperature to 80 K for technical reasons. As the corresponding calibration curve can be fitted by a Boltzmann factor, we believe that it can also be applied at temperatures outside the original calibration range. However, systematic errors may not be excluded for the measured high temperatures.

Furthermore, the measured temperature only represents a time-averaged value with an integration time of ten seconds. While for the polymerization (which is a highly deterministic process), the obtained value is assumed to be the actual (constant) temperature of the voxel, the observed micro-explosions occur only occasionally (although with increasing rate for higher writing powers). Hence, the actual peak temperatures within the sample may be by far higher.

Apart from the UCNP signal, broadband background luminescence is observed in the overexposure regime. The spectral shape of the observed background signal is consistent with thermal (Planck) radiation from a hot plasma with plasma temperatures in the range of a few thousand Kelvin and is in some cases even visible by the bare eye as a faint, orange flickering. As this signal also occurs without any particles inside the photo-resist, it might indeed originate from an electron plasma which is triggered by multi-photon ionization, followed by avalanche ionization and enforced by further heating through the writing laser or the UCNP excitation laser. This background is broad and flat compared to the particle luminescence, and hence, it can be subtracted with a pre-factor chosen such that the corrected luminescence signal goes down to zero where no particle luminescence is expected from the reference experiments.

In order to show that the source of this background signal indeed is different from the nanoparticle luminescence (and thereby, the temperature signal), we performed a similar temperature probe measurement with the writing laser focus being shifted with respect to the thermal probing region, i.e., the co-aligned particle excitation laser and luminescence detection spot. Once again, the alignment was done through the gold bead scanning technique.



**Figure 5.6:** Spatial profile of the measured average temperature and integrated broadband background luminescence. The writing laser spot (red) is shifted with respect to the detection region perpendicular and parallel to the writing direction as indicated by the dashed lines in the insets (top and bottom panel, respectively; inset images acquired by the microscope camera of the DLW setup). The writing power is chosen above the over-exposure threshold ( $P_{\text{Ti:Sa}} = 20 \text{ mW}$ ) in order to see a pronounced thermal effect (otherwise same parameters as for **Figure 5.5**). Reproduced from [94]. ©2013, AIP Publishing LLC.

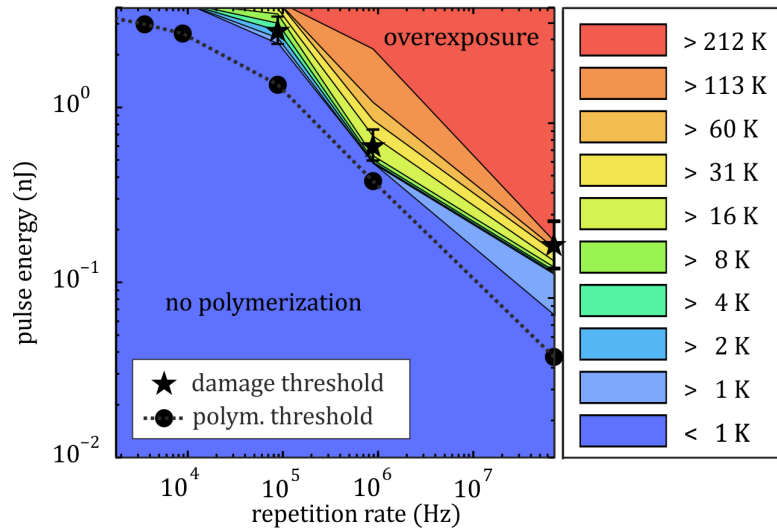
The resulting temperature profiles are depicted in **Figure 5.6**. The writing power is chosen above the threshold for overexposure, as below that threshold, no thermal effect is visible. The thermally affected zone has a diameter of around  $5 \mu\text{m}$  (FWHM) in the direction perpendicular to the writing direction, while in writing direction, the writing laser leaves a “hot trace” which extends over more than  $10 \mu\text{m}$ . In contrast, the region where the overexposure-related background is detected is fairly symmetric and has a diameter of approximately  $2 \mu\text{m}$ , which clearly hints that the source of the background luminescence is distinct from the particle luminescence, even though both are related through thermal effects.

Through the used MaiTai-Setup, the experiment is restricted to high repetition rates and non-fluorescent photo-resists (such as the commercial Irgacure photo-initiators). Therefore, a second set of similar experiments is performed to



measure the temperature also at lower repetition rates using the Chameleon-Setup. In order to reduce the sensitivity to cooling effects at repetition rates with pulse-to-pulse periods larger than the characteristic cooling time scale (Section 3.3.4), the temperature is measured in a time-gated scheme for all repetition rates lower than 80 MHz. I.e., the detection channel is chopped by an additional acousto-optic modulator and only opened for a period of 0.5  $\mu\text{s}$ , starting 0.1  $\mu\text{s}$  after each laser pulse. The effective integration period is kept constant by increasing the absolute integration time correspondingly when lower repetition rates are applied. Even at low repetition rates and therefore at high pulse energies, substantial temperature changes are only observed alongside the formation of micro-explosions, while close to the writing threshold, no local heating can be detected (**Figure 5.7**).

From these findings, we conclude that the dominant mechanism for radical formation is purely photo-chemical at all investigated repetition rates, while a (at least partly) photo-thermal process is connected to the sample damage in the overexposure regime. This observation is in perfect agreement with the behavior of the photo-resist with respect to the laser repetition rate as described in the previous section.



**Figure 5.7:** Temperature increase at different writing laser repetition rates. Within the writing regime, no significant temperature increase can be measured at any repetition rate. Please note that only at high repetition rates (80 MHz), a small, but reproducible and significant temperature increase of approximately  $2 \pm 1$  Kelvin is observed already at pulse energies where no explosions occur. The physical origin of this effect is not completely clear. At low repetition rates, the effect may be suppressed by heat conduction and hence, not be detectable in this experiment (Section 4.1). In sharp contrast, substantial temperature changes occur in all cases for pulse energies higher than the damage threshold.

### 5.2.1 Local Heating of Fluorescent Photo-Resists

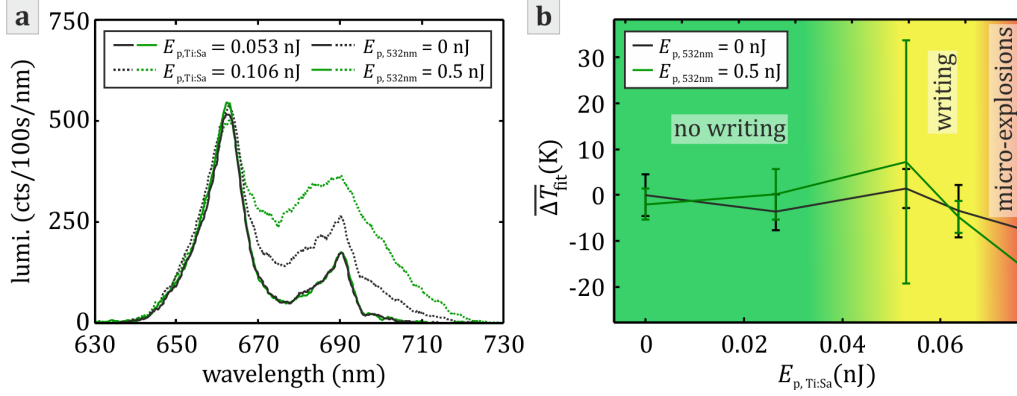
In the Section 5.2, the investigation of the local sample heating for one specific photo-resist based on the commercial photo-initiator Irgacure 819 was described. As argued before, we believe that these results also hold for other commercial photo-initiators. However, one especially active field within the research area of multi-photon polymerization is the research on STED-DLW and related super-resolution approaches [12, 16, 50, 51, 56] (Section 2.3). For this research field, commercial photo-initiators are often not suitable as they lack an efficient channel for de-excitation. Hence, the photo-sensitizer DETC is of special interest for these approaches as it offers the opportunity to use “true” (and hence, ultra-

fast) stimulated emission depletion (STED) as depletion mechanism [18]. This approach has been investigated by several groups and has proven to be able to break the diffraction limit and yield a so far unreachable resolution for the writing of free-standing three-dimensional structures [17, 19–21].

However, DETC has certain advantages as compared to other photo-initiators also for standard DLW. For example, it is relatively efficient and yields a writing threshold similar to the commercial Irgacure photo-initiators, although at concentrations which are almost one order of magnitude smaller (**Figure 5.2**). Also, DETC photo-resists are quite insensitive to UV-irradiation and therefore easier to handle in standard laboratory environments (no yellow-light environment required).

For the reasons described above, we aimed at acquiring a better understanding of the underlying mechanisms especially for this specific photo-initiator. However, for the measurement of the local temperature increase due to the DLW process, this turned out to be rather challenging from the experimental side due to the DETC fluorescence, which is by far more intense than the UCNP luminescence. Hence, several experimental changes were made in order to improve the temperature measurement procedure (Section 4.1.1). Typical UCNP spectra as well as the best temperature measurement so far are displayed in Figure 5.8. Unfortunately, this result is not very satisfactory for two reasons. First, the measurement precision is relatively poor (approx.  $\pm 5$  K) due to the heavily reduced luminescence count-rate caused mainly by the use of particles with silica shell to avoid Förster resonant energy transfer (FRET) to the DETC. Second, we find that in the overexposure regime, the UCNP spectrum is altered by non-thermal effects as compared to the reference spectrum. Namely, we find that in this case, the 690 nm-peak is increased (and broadened) with respect to its 670 nm counterpart, while when increasing the sample temperature, the opposite is the case. Hence, this method is clearly inappropriate in this regime.

Below the writing threshold, no significant heating can be detected, no matter whether the depletion laser is switched on or not. However, keeping in mind that the local peak temperature may be higher by a factor of 10 or more when compared to the (displayed) average temperature, a clear-cut interpretation of these results seems inappropriate and further experiments will be required to yield a conclusive result.



**Figure 5.8:** **a)** Measured spectra of the photo-resist with the dispersed silica shell nanoparticles for selected writing laser powers ( $P_{980\text{ nm}} = 20\text{ mW}$  in all cases) at a repetition rate of 1 MHz and with time-gated detection. The chosen writing laser pulse energy of 0.053 nJ corresponds to the writing threshold (for a switched off depletion laser), micro-explosions occur at 0.106 nJ. The depletion laser pulse energy (0.5 nJ) with a pulse offset of 0.2 ns as compared to the writing laser corresponds to the situation with optimal depletion behavior [23]. Please note that the spectral detection window is restricted to wavelengths from 650 nm to 725 nm by chromatic beam splitters and the acousto-optic modulator in the detection channel. Hence, a spectrally flat sensitivity is not given due to the finite sized band edges ( $\approx \pm 20\text{ nm}$ ). Still, the temperature measurement should not be altered as it only relies on the relative peak height. Also, the particles used for these measurements originate from a different batch than the particles used for **Figure 4.5**. Therefore, the absolute height of the different peaks may be altered due to slightly different doping concentrations. **b)** Measured average temperatures both with and without the depletion laser (calibration according to **Figure 4.5**). In the polymerization regime, no significant heating can be observed. However, the statistical errorbars already indicate a precision of only approximately  $\pm 5\text{ K}$  for the average temperature. Additionally, at this repetition rate, the peak temperature may exceed the average temperature by roughly a factor of ten due to cooling effects (Section 4.1.1), so that this statement is rather weak. In the regime of micro-explosions (not displayed), non-thermal effects disturb the temperature measurement as the observed increase of the 690 nm-peak would correspond to a negative temperature change by several tens or hundreds of Kelvin.

## 5.3 Radical Generation

Common commercial photo-initiators such as Irgacure 819 which is used extensively throughout this thesis are relatively well investigated and their reaction pathway for radical generation through photo-cleavage has been investigated in great detail. In the case of Irgacure 819 (Phenylbis(2,4,6-trimethylbenzoyl)phosphine oxide), the photo-initiator molecule is excited to the first singlet state, from where it undergoes intersystem-crossing to the lowest triplet state and then dissociates into a 2,4,6-trimethylbenzoyl and a diphenylphosphinoyl radical [66]. The reported lifetimes of the intermediate states (singlet and triplet) are both in the order of nanoseconds or even less, so that the quantum yield for radical generation is large and the radical generation process is very efficient. These findings are in very good agreement with the results for DLW which have been presented in the previous sections.

However, for the photo-initiators such as DETC and ITX, which can be used for STED-DLW, this is not the case. As described in Section 3.1.3, DETC is commonly classified as a Norrish type II photo-initiator, i.e., it is expected to require a co-initiating species in order to efficiently generate radicals [113]. However, as indicated in Section 5.1, this mechanism does not explain the experimental results for multi-photon polymerization. Here, one observes an effective three-photon absorption behavior - which is highly surprising, as the fundamental electronic transition ( $S_0$ - $S_1$ ) could be excited by two photons of around 800 nm wavelength from simple energy conservation considerations.

From these experiments, it is therefore unclear what the excitation pathway for radical generation in the case of DETC looks like. More precisely, it could for example be that DETC is excited through a direct (quantum-mechanically resonant) three-photon absorption (i.e.,  $S_0$ - $S_n$ , most likely if  $S_0$ - $S_1$  would be suppressed for symmetry reasons). The three-photon behavior could also originate from a first two-photon excitation step, followed by additional (quantum-mechanically non-resonant) excited-state absorption (e.g.,  $T_1$ - $T_n$ ). In order to bring some more light into this issue, we performed several experiments which will be described within the following sections.<sup>4</sup>

---

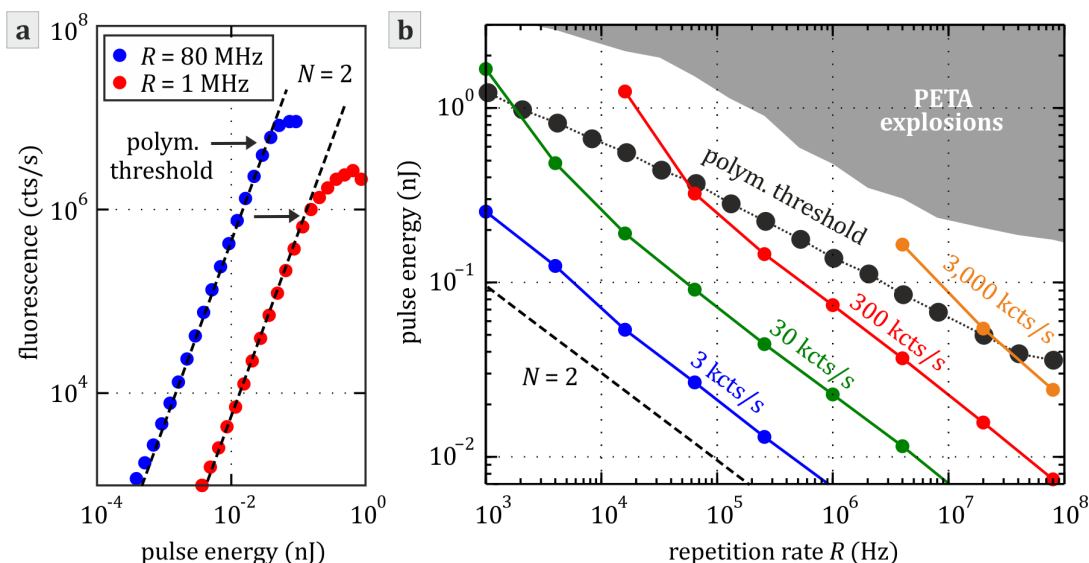
<sup>4</sup> Experiments published in [23].

### 5.3.1 Intermediate State Fluorescence

For the first experiment on the excitation pathway of DETC, namely examination through optical fluorescence spectroscopy, we used the same experimental setup as described in the previous Section to measure the fluorescence of the photo-resist itself in a confocal scheme during the writing process (instead of the fluorescence from additionally added nanoparticles). Hence, the pulse duration, wavelength and the photo-resist are exactly the same as for the above-mentioned DLW experiments. As the polymerization process leads to changes in the optical environment of the fluorescing molecules above the polymerization threshold (e.g., change in refractive index, change in solvent viscosity etc.), the data points in that regime should be interpreted with caution. From the results presented in **Figure 5.9**, it is obvious that the luminescence is excited by a two-photon channel, in contrast to the polymerization which clearly follows a different scaling behavior. Above the polymerization threshold, the scaling behavior changes in that the fluorescence saturates. However, from the data, it is not evident whether this effect is caused by depletion of the photo-initiator ground state through radical generation or by fluorescence quenching due to the polymerization itself.

In order to clarify the nature of the third absorption process, one can rely on the different lifetime of the intermediate states. Pump-probe experiments on the triplet-state absorption have been performed for DETC and indicate that indeed, triplet absorption is likely to occur at the excitation laser wavelength [22]. While for Norrish type I photo-initiators, the lifetime of the triplet state is as short as that of the singlet ( $\tau_{\text{singlet}} \approx \tau_{\text{triplet}} \approx 0.1$  ns [66], Irgacure 819 in acetonitrile), this is not the case for Norrish type II photo-initiators. Here, lifetimes of  $\tau_{\text{singlet}} \approx 1$  ns [18] and  $\tau_{\text{triplet}} \approx 2.3$   $\mu$ s [20] have been reported for the singlet and the triplet state, respectively (DETC in PETA, no co-initiator added).

Under typical DLW conditions (excitation with high repetition rate), it has been observed that the effective triplet lifetime is reduced from the microsecond regime down to  $\tau_{\text{triplet, effective}} \lesssim 100$  ns [19]. For these reasons, we believe that triplet state absorption is a more promising candidate for the  $N = 3$  excitation pathway of DETC, even though resonant three-photon absorption cannot be entirely excluded at the current stage.

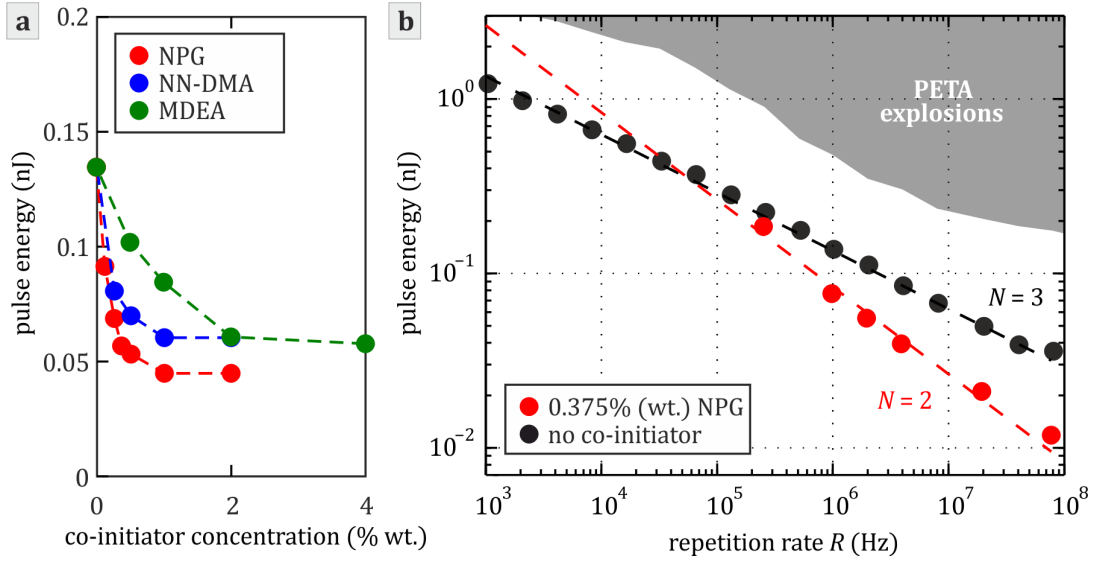


**Figure 5.9:** **a)** Spectrally integrated DETC fluorescence signal as a function of the excitation laser pulse energy at two selected repetition rates. For comparison, the expected scaling for two-photon absorption is indicated in both panels ( $I_{\text{fluorescence}} \propto E_p^N$  with  $N = 2$ ). **b)** Iso-fluorescence lines as a function of pulse energy and repetition rate. Below the polymerization threshold, the measured fluorescence intensity clearly scales according to  $N = 2$  throughout the investigated regime. Noticeably, the polymerization threshold corresponds to fluorescence intensities that differ by more than two orders of magnitude when comparing high (80 MHz) and low (1 kHz) repetition rates. This clearly indicates that “pure” two-photon absorption cannot explain the radical formation pathway by DETC. Above the polymerization threshold, fluorescence saturation can be observed at all repetition rates.

### 5.3.2 Charge Transfer with Co-initiators

Even though Norrish type II photo-initiators such as DETC can be used without co-initiator, the use of co-initiator may be of interest. It allows to draw conclusions on the excitation pathway, and it reduces the polymerization threshold pulse energy, which sometimes is relevant for applications. Also, co-initiators may provide some advantages with respect to STED-DLW approaches.

A set of different co-initiators was investigated under DLW conditions, including the commonly used co-initiators N-phenylglycine (NPG), N,N-dimethylaniline (NNDMA) and N-methyl diethanolamine (MDEA), which all show very similar



**Figure 5.10:** Polymerization threshold pulse energy as a function of **a)** the co-initiator concentration for different photo-resists (PETA + 0.25% (wt.) DETC + co-initiator) ( $R = 2$  MHz) and **b)** the repetition rate for two selected photo-resists with and without co-initiator (PETA + 0.25% (wt.) DETC (+) 0.375% (wt.) NPG). The straight lines correspond to the expected scaling behavior for absorption processes with different nonlinearities ( $N = 2$  and  $N = 3$ ).

sensitizing behavior (**Figure 5.10 a**).<sup>5</sup> More precisely, the polymerization threshold is reduced by roughly a factor two at the investigated repetition rate (2 MHz) and saturates for high co-initiator concentrations. The sensitizing efficiency (or in other words, the co-initiator reactivity) and, hence, the optimal concentrations for the different species differ slightly. However, the similar saturation levels indicate that the underlying mechanism is the same and yields the same result if a concentration close to the saturation value is selected (e.g., 0.375% (wt.) for NPG, 0.5% (wt.) for NNDMA, and 2% (wt.) for MDEA). NDMA and MDEA are volatile substances and, hence, evaporate from the photo-resist droplet at room temperature, so that the concentration changes over time and the polymerization threshold shifts. In order to avoid this effect, we encapsulated the corresponding samples through a sandwich structure consisting of two glass cover slips, separated by a ring made of Polydimethylsiloxane.

<sup>5</sup> Experiments primarily conducted by J. Fischer and published in [23].



In order to examine the initiation mechanism, we tested the photo-resist with 0.375 % (wt.) of NPG at different repetition rates (**Figure 5.10 b**). Clearly, the behavior corresponds to an effective two-photon scaling at high repetition rates. At low repetition rates, the three-photon pathway is once again dominant. This is consistent with our interpretation of the excitation mechanism in terms of a primary two-photon absorption step followed by radical generation either through an additional triplet-absorption process ( $N = 3$ ) or through charge transfer to a co-initiator molecule if the latter is available ( $N = 2$ ).

Judged by these findings, NPG seems to be the co-initiator of choice for DLW with DETC. However, NPG starts absorbing at wavelengths below 400 nm with a long spectral tail towards the visible region, which may lead to problems for STED-DLW approaches as absorption through the co-initiator may occur at the depletion wavelength. We furthermore tested 2,4,6-Tris(trichloromethyl)-1,3,5-triazine, Ethyl 4-dimethylaminobenzoate and Triphenylamine as co-initiators. While the latter substance has been shown to quench the triplet state of DETC similarly to NN-DMA [114], it only leads to marginal sensitizing as compared to the co-initiators from **Figure 5.10** at comparable concentrations. The other two substances lead to no sensitizing effect at all.



# 6 Chapter 6

---

## Polymerization Mechanisms

In the previous chapter, experiments that give hints on the reaction pathway for radical generation by multi-photon absorption were discussed. After this first reaction step, the actual solidification of the (previously liquid) photo-resist occurs by polymerization of the monomer. This chapter therefore includes a second set of experiments concerning the reaction conditions during this second polymerization step. More precisely, as discussed in Chapter 3, possible chemical reaction pathways for these polymerization reactions are well investigated. However, most experiments presented in literature have been performed for very different reaction conditions as compared to DLW, namely, polymerization in films or within macroscopic containers that is initiated by (oftentimes relatively weak) UV-radiation.

While in principle, generic reaction properties such as reaction rate coefficients can be deduced from these experiments and allow for a numerical modeling of the chemical reaction, such modeling often leads to insufficient results for DLW. The reason is that in this case, the large change of the reaction parameters during the reaction must be considered and, more importantly, the spatially inhomogeneous polymerization enables local effects such as diffusion, which must be included in such a model as well. Furthermore, the use of multifunctional acrylates leads to highly cross-linked networks instead of polymer chains, which complicates the quantitative description of the reaction. For these reasons, experiments within this chapter aim at a quantitative description of the reaction conditions, the determination of the dominant reaction steps and thereby, in an ideal case, the ability to predict the outcome when changing the DLW process.

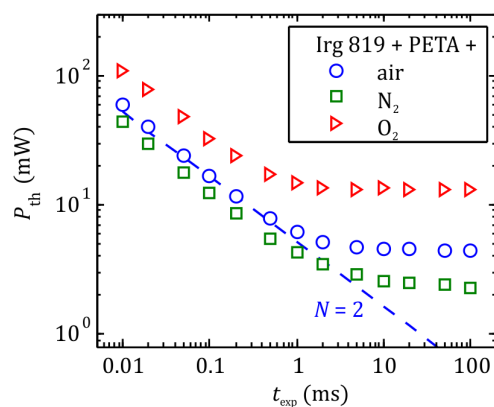
## 6.1 Termination Reactions

While the initiation of the polymerization reaction for DLW has been given a lot of attention, the actual polymerization reaction has hardly been examined for DLW. The chemistry of the chain propagation along the lines of Section 3.2.1 is relatively clear for a given monomer, however, the dominant termination mechanism is not. While radical-radical termination is often dominant for polymerization within the bulk [69], this may not be the case for DLW. Here, the influence of inhibiting species such as atmospheric oxygen and additives, which have been added to the photo-resist to prevent accidental polymerization, should be considered as well. More precisely, Monomethyl ether hydroquinone (MEHQ) is mostly present in commercial monomers for storage stability (and usually not removed prior to DLW). Furthermore, one should keep in mind that the overall conversion is likely limited by the reduced mobility of the functional groups already at moderate conversions due to the high degree of cross-linking (Section 3.3.3).

### 6.1.1 Quenching by Oxygen

As already discussed in Section 3.2.1, oxygen inhibition is known to disturb photo-polymerization in many cases [68,77,115]. For the special case of DLW, the magnitude of this effect has not been clear for a long time. Therefore, we investigated the DLW process when photo-resists are used that are either oxygen-enriched or oxygen-depleted through bubbling of the photo-resist with oxygen and nitrogen, respectively. In order to get the oxygen concentration close to the saturation level (or in the other case, suppress the oxygen inhibition substantially), sealed samples were prepared as sandwich structures of two glass cover slides with a ring of silicone in between after bubbling of the photo-resist with the corresponding gas for at least 60 minutes.

Experimentally, we found that the initial writing threshold and thereby the initial oxygen concentration only recovers over roughly a day. Hence, this configuration allows for reproducible measurements within the first few hours after sample preparation. However, as the preparation of the sealed substrates does not occur under oxygen or nitrogen atmosphere for practical reasons, sample contamination may occur and the absolute oxygen concentration for these experiments cannot be given.

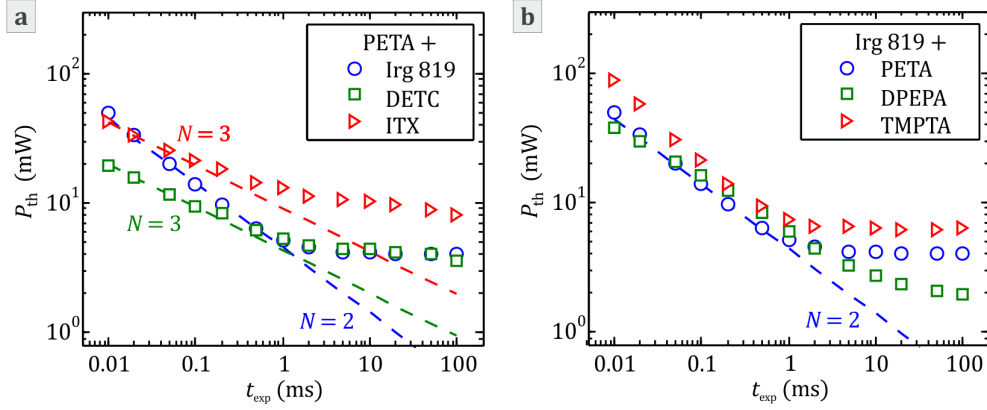


**Figure 6.1:** Writing threshold power as a function of the exposure period under normal atmosphere and under oxygen-depleted and oxygen-enriched conditions. For illustration, a straight line with the slope corresponding to  $N = 2$  is depicted as well, illustrating the expected behavior according to Equation (3.5). The presence of oxygen increases the writing threshold in all cases. While for exposure periods shorter than approximately a millisecond, the polymerization threshold scales consistently with two-photon absorption, a saturation regime is observed for longer exposures. Here, the threshold power is constant and does not depend on the exposure period while inhibition by oxygen leads to an even more pronounced threshold shift. Reproduced from [110]. ©2014 Wiley VCH.

In order to allow for a quantitative analysis, single dots are written close to the interface of photo-resist and substrate by the exposure with high-repetition rate (80 MHz) pulse-trains of different durations (**Figure 6.1**).

For short exposure periods, we find that atmospheric oxygen is responsible for a shift of the polymerization threshold by factors of around four, where the post-polymerization assumption is justified as described in Section 6.2. Moreover, it even completely prevents polymerization if the laser power is chosen too low, no matter how long the photo-resist is exposed, as can be evidenced by the plateau on the right side. In that regime, the threshold laser intensity for polymerization is independent from the exposure period.

In the case of photography, this effect is known for more than a century as the Schwarzschild effect [116]. For DLW, it can only be understood when considering oxygen quenching in combination with oxygen diffusion: If the writing laser power is chosen low, the rate of quenching through oxygen



**Figure 6.2:** Writing threshold power as a function of the exposure period under normal atmosphere for different photo-resists. As for the reference photo-resist in **Figure 6.1**, a clear deviation from the behavior expected according to Equation (3.5) can be seen at long exposure periods, corresponding to the lithography analogon to above-mentioned Schwarzschild effect. Reproduced from [110]. ©2014 Wiley VCH.

diffusion from the surrounding exceeds the rate of radical generation, and hence, no polymerization occurs at all, no matter how long the photo-resist is exposed. Polymerization will only start if the radical generation rate is high enough to overcome the rate of termination by oxygen diffusion. However, also in this case, the reaction will be stopped by oxygen quenching as the radical generation rate quickly decreases when the photo-initiator is consumed. Hence, the writing threshold does not depend on the exposure period in this regime. These observations are fully consistent with the mentioned results from Raman micro-spectroscopy, where a writing velocity of less than  $50 \mu\text{m/s}$  ( $t_{\text{exp}} \leq 7 \text{ ms}$ ) leads to saturation effects (Section 3.3.3) [91].

A very similar, Schwarzschild-like behavior is found for a larger set of different photo-initiators and monomers (**Figure 6.2**). More precisely, photo-resists containing the monomer PETA with either 1.0% (mol) of Irgacure 819, 3.7% (mol) of Irgacure 369, 1.3% (mol) of Darocur TPO, 0.26% (mol) of DETC, or 1.0% (mol) of ITX as photo-initiators are tested. As we find very similar results for the first three compositions, data for Irgacure 369 and Darocur TPO are not depicted. From Equation (3.5), we expect that the writing threshold scales according to  $P_{\text{th}} \propto t_{\text{exp}}^{-\frac{1}{N}}$ , with  $N = 2$  for the Norrish type I photo-initiator Irgacure 819 and  $N = 3$  for the Norrish type II

photo-initiators DETC and ITX (Section 5.1). Corresponding straight lines are displayed in the double- logarithmic plots in **Figure 6.1** and **Figure 6.2**.

To investigate the influence of different monomers, we examined Pentaerythritol triacrylate (PETA), Trimethylolpropane triacrylate (TMPTA), Pentaerythritol tetraacrylate (PETTA), and Dipentaerythritol pentaacrylate (DPEPA), all sensitized with 1.00% (mol) of Irgacure 819. The formulation with PETTA shows very similar behavior as the formulation with PETA and is therefore not included in **Figure 6.2**.

As the qualitative behavior is very similar for all of these compositions, we ascribe the inhibition mainly to a radical quenching mechanism that hinders the acrylate polymerization and not to triplet quenching, which in principle provides a possible mechanism for oxygen inhibition as well (Section 3.2.4).

However, the quantitative behavior is different for the different photo-resists regarding the size of the transition regime, the saturation level etc., which is not very surprising as the relative concentrations of photo-initiator and oxygen and the underlying reaction rates for oxygen quenching are different as well. For example, the formation of the threshold plateau is less pronounced for the very viscous monomer DPEPA, resulting from a reduced oxygen diffusion rate.

In addition, we include photo-resist compositions with the monomers Trimethylolpropane trimethacrylate (TMPTMA), Poly(ethylene glycol) diacrylate (PEG-DA, average molar weight  $M_n$  700) and Butyl acrylate (BA, all sensitized as above) into our studies. However, no writing is possible with these formulations in the case of short exposures below approximately 10 ms. The reason of the observed behavior is not perfectly clear. As the structuring result is not comparable to the photo-resists based on multi-functional acrylates in terms of resolution, an in-depth investigation of these resists seems not very promising.

Furthermore, a bi-radical termination mechanism as discussed in Section 3.2.3 can be excluded to play an essential role on the basis of the results presented in this section. Namely, bi-radical termination goes along with a square-root dependence of the polymerization rate on the radical concentration (Section 3.2.3). The polymerization threshold then would scale according to  $P_{th} \propto t_{exp}^{-2/N} = t_{exp}^{-1}$  for  $N = 2$ , with the factor 2 in the exponent originating from the bi-molecular termination. However, such behavior is not found for any of the investigated photo-resists in **Figure 6.1** and **Figure 6.2**.

### 6.1.1.1 Influence on the 3D-Resolution

In the context of super-resolution DLW, the addition of quenching species to the photo-resist has mainly been discussed in the context of an improvement of the achieved lithographic resolution [56,57]. It can be argued that the presence of quencher molecules leads to a more pronounced threshold behavior, resulting in a more pronounced polymerization suppression especially in the tails of the writing laser focus. More precisely, the authors of [57] argue that radicals generated by the laser exposure may diffuse out of the exposure volume and thereby reduce the achievable writing resolution. This effect can be prevented by adding quenching moieties, which are, in their case, photo-activated by an additional “depletion” laser beam. Apparently, this is also the working mechanism for the resolution enhancement reported by an earlier publication of the same group [50].

A different approach reported in literature is supposed to lead to enhanced resolution through quencher diffusion [117–119]. As shown by the authors of [119] also on the basis of numerical calculations, quencher diffusion can lead to smaller feature sizes as it mostly prevents polymerization in the outer regions of the writing focus, while quencher depletion only occurs in a central part (which may obviously be smaller than the original exposure region). Thereby, the action of the quenching molecule can not any longer be described as a local response of the photo-resist, and the resolution limit can be circumvented. Indeed, a moderate improvement in terms of feature size (100 nm instead of 120 nm) is reported within the early works based on 2,6-Di-tert-butyl-4-methylphenol as a radical quenching species [118].

However, this improvement comes along with a decrease in structural stability, so that for compact 3D structures, the overall resolution improvement is even less pronounced. In [119], 2-(Dimethylamino)ethyl methacrylate is used as a quenching moiety, which – to the best of our understanding – actually represents a monomer (yielding presumably less reactive radicals) rather than a quenching species. Furthermore, from the given data, it is not clear whether the experimental effect could also be explained by a mere threshold shift leading to smaller feature sizes at an identical exposure dose.

Another issue with the mentioned approaches is the fact that, in principle, diffusion of all involved chemical species may occur, not only including radicals and quencher molecules, but also growing monomer chains, unreacted photo-initiator molecules, or molecular oxygen. Which of these diffusion processes turn out to be crucial for the overall process in the end will not only

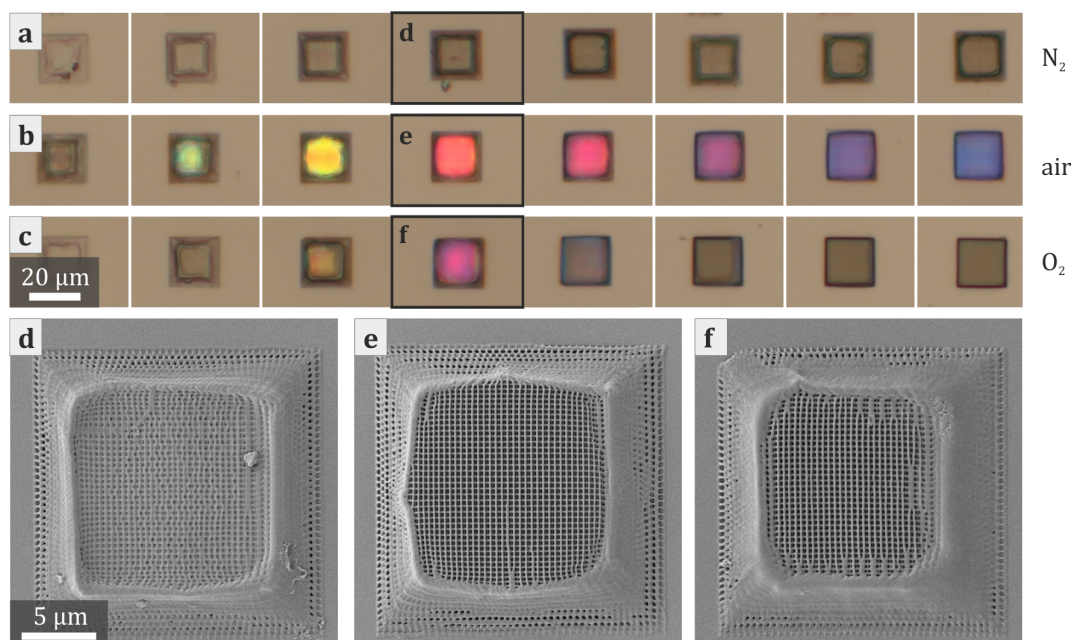


depend on the hydrodynamic radius of the given molecule species, which may be estimated on the basis of the geometrical size of the molecule (Section 3.3.5), but also on the molecule lifetime under the given reaction conditions, which in many cases is not very well investigated.

In the context of this section, the situation seems clearer, as molecular oxygen represents the smallest of all involved molecules, and as it is stable in the photo-resist when no radicals are generated. Hence, it is very likely that oxygen diffusion from the surrounding photo-resist to the reaction region represents the dominant diffusion effect. This seems even more plausible as, along the lines of the above-mentioned explanation for the Schwarzschild effect, a suppression of the polymerization through oxygen diffusion is seemingly responsible for the largely increased polymerization threshold in the case of long exposure periods. Therefore, we expect that the resolution is increased with increasing oxygen concentration following the argumentation of [119] whenever oxygen is present in the photo-resist (which obviously is the case for most standard configurations of conventional and STED-enhanced DLW).

Experimentally, we find, however, that adding additional oxygen to the photo-resist will not help to yield improved writing resolutions if a certain oxygen concentration is exceeded (**Figure 6.3**). More precisely, the resolution is decreased in both cases with higher and lower oxygen concentrations than those at ambient conditions. This finding seems surprising at first glance, however, the results are fully reproducible. Furthermore, as an additional test, the experiment was exerted with an oxygen or nitrogen enriched resist which was subsequently kept at standard atmosphere in an open container for some hours to yield the initial oxygen concentration again. In this case, the same behavior is observed as for the reference photo-resist, excluding most systematic experimental errors.

For the oxygen-reduced case, the lack of oxygen diffusion may lead to a decline of the resolution, as the resolution is improved in the presence of oxygen along the lines of the above-mentioned argumentation. In the opposite case, the interpretation of the results not trivial. One possible explanation is based on the depletion of photo-initiator molecules. Namely, in order to overcome oxygen quenching at higher oxygen concentration, a larger number of initial radicals is required, or in other words, the overall initiator efficiency is decreased. The overall radical number is limited by the finite number of photo-initiator molecules available in the focal volume, and hence, may not be sufficient to yield the required amount of radical molecules



**Figure 6.3:** Real color optical micrographs (illumination in reflection mode) of woodpile photonic crystals written as benchmark structures **a)** in the nitrogen enriched photo-resist, **b)** under atmospheric conditions, and **c)** in an oxygen enriched photo-resist. In this configuration, the structures appear colored if they are fully resolved in axial direction. A high resolution therefore corresponds to a relatively large laser power regime for which stable and fully resolved structures can be fabricated at one specific rod distance. Hence, a broad range of colored structures indicates that smaller rod distances would be feasible as well under similar conditions. The structures are written using pulse bursts at a duty cycle of 3% (burst repetition rate 4 kHz) and with a writing velocity of  $v = 100 \mu\text{m/s}$ . The average writing power during the pulse burst is 4.2 mW(**a**), 5.8 mW (**b**), and 10.1 mW(**c**), respectively, for the structures in the very left column, and is increased from left to right in steps of 1% per column. **d-f)** Scanning electron micrographs of selected structures. The nominal lateral distance of adjacent rods is 450 nm in all cases. Reproduced from [110]. ©2014 Wiley VCH.

in that case anymore. If the excitation laser power is further increased beyond this saturation point, the overall number of initiating radicals will be increased as more radicals are formed in the boundary areas of the focal volume. In the center, however, no additional radicals can be generated as the photo-initiator ground state is depleted already. Hence, the overall diameter (e.g. FWHM) of the radical distribution will be enlarged with respect to the optical focus, and its shape changes from the Gaussian profile to a broadened and smeared-out flat-top profile. Therefore, the minimal feature size increases and the resolution is deteriorated. While in principle, this behavior could be overcome by simply increasing the photo-initiator concentration, the latter is limited by the photo-initiator solubility in the monomer.

## 6.1.2 Quenching by Photo-Resist Additives

### Mono Methyl Ether Hydroquinone (MEHQ)

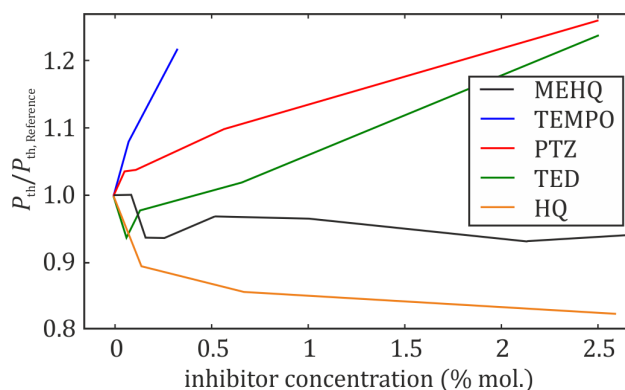
In addition to quenching by oxygen, other inhibitors may play a role for DLW. One other photo-inhibitor which is often present in photo-resists is Mono methyl ether hydroquinone (MEHQ), as this molecule is often contained to commercially available monomers in concentrations of approximately 0.01 – 0.05 % (mol.) (100 – 500 ppm) to prevent accidental polymerization. Hence, it seems obvious that the influence of MEHQ on the DLW process should be studied in further detail. However, we find that MEHQ has no significant influence on the DLW process. For example, photo-resists mixed from purified PETA<sup>1</sup>, 0.25 % (mol.) of DETC and different concentrations of MEHQ do not show a significant change of the polymerization threshold (**Figure 6.4**).<sup>2</sup>

Further literature study reveals that the most efficient radical termination mechanism in the case of MEHQ is a two-step reaction including oxygen. More precisely, as a first step, the propagating radical reacts with molecular oxygen. The radical oxygen product of this reaction can then be quenched by MEHQ [120–122]. In the absence of oxygen, only a weak inhibition effect is attributed to MEHQ [120,123], whereas oxygen is reported to inhibit polymerization reactions without MEHQ as well [121, 124]. According to literature, typical oxygen concentrations for acrylate monomers are in the order of 0.006-0.025 % (mol.) (or 60-250 ppm) [70, 82, 122]. It has been reported that in the presence of

---

<sup>1</sup> The initial MEHQ content is removed by column chromatography.

<sup>2</sup> Experiments conducted by F. Mayer under supervision of the author. The results for MEHQ are included in the Bachelor thesis of F. Mayer.



**Figure 6.4:** Relative threshold shift for photo-resists containing different concentrations of photo-inhibitors. The basic photo-resist is based on PETA with 0.25 % (mol.) of DETC as photo-initiator. In order to experimentally access low inhibitor concentrations, the monomer is purified by column chromatography prior to usage. Only TEMPO, PTZ and TED act as photo-inhibitors as intended, whereas MEHQ and HQ show no effect or even act as co-initiators, respectively.

MEHQ and oxygen, statistically six oxygen molecules are required to quench one radical, while if the MEHQ is consumed, this number increases up to 32 [120]. Hence, MEHQ acts as a catalyst for oxygen inhibition rather than as a polymerization inhibitor by itself. Therefore, the oxygen concentration (and not the MEHQ concentration) is the delimiting factor for this process in many experimental situations.

While for bulk polymerization during storage, the oxygen concentration may not be crucial with atmospheric oxygen being constantly available, certainly is the case for DLW. Here, the rate of radical generation is large, and hence, oxygen depletion may occur in the reaction volume. As the polymerization threshold does not change with the MEHQ concentration, it is not very surprising that the structuring resolution does not depend on the MEHQ concentration as well. Written benchmark structures along the lines of **Figure 6.3** with both, higher and lower MEHQ concentration with the unpurified monomer show no significant difference as compared to the reference photo-resist. Hence, the common practice of using the monomers as obtained by commercial suppliers does not seem to have a detrimental effect on the DLW process.

### Other Polymerization Inhibitors

As MEHQ does not show the intended inhibition effect, a larger set of substances known as direct radical quenchers were included into this study as well. These include (2,2,6,6-Tetramethylpiperidin-1-yl)oxidanyl (TEMPO), Phenothiazine (PTZ), and Tetraethylthiuramdisulfid (TED), which are found to increase the polymerization threshold (**Figure 6.4**). In contrast, hydroquinone (HQ) not only shows no inhibition effect, it even acts as a co-initiator. For PTZ and TEMPO, the dominating inhibition mechanisms are well investigated and do not involve oxygen ([120] and [69,125], respectively). As these substances are partly volatile, all experiments are performed with encapsulated samples as described in Section 6.1.1.

As in the case of oxygen, it seemed promising to check whether any of these photo-inhibitors can be used to improve the structuring resolution. However, this is not the case. More precisely, the resolution is largely similar when TEMPO (the most efficient of the investigated inhibitors) is added to the photo-resist, and even decreases for PTZ and TED. Unfortunately, TEMPO is not transparent in the optical spectrum and hence, cannot be used for STED-DLW.

All in all, it is not directly evident whether or not adding additional inhibitor molecules to a photo-resist leads to improved writing results in terms of resolution. As described for the special case of oxygen, both effects – resolution enhancement through inhibitor diffusion and resolution deterioration through photo-initiator depletion – do actually occur in practice. However, from the experiments performed in the context of this thesis, it seems that this route is not very promising to improve the DLW process, at least for the investigated class of photo-resists based on multifunctional acrylates.

## 6.2 Duration of the Polymerization Reaction

Apart from the reaction mechanisms, it is essential to know under which conditions the polymerization reaction occurs. For many effects such as diffusion of molecules or heat conduction, the reaction progress as a function of time and in particular the overall reaction duration are important parameters (Section 3.3.4 and Section 3.3.5). Unfortunately, it has been very unclear in the past what the reaction duration would typically be for DLW, as the reaction conditions differ from film polymerization experiments as the exposure

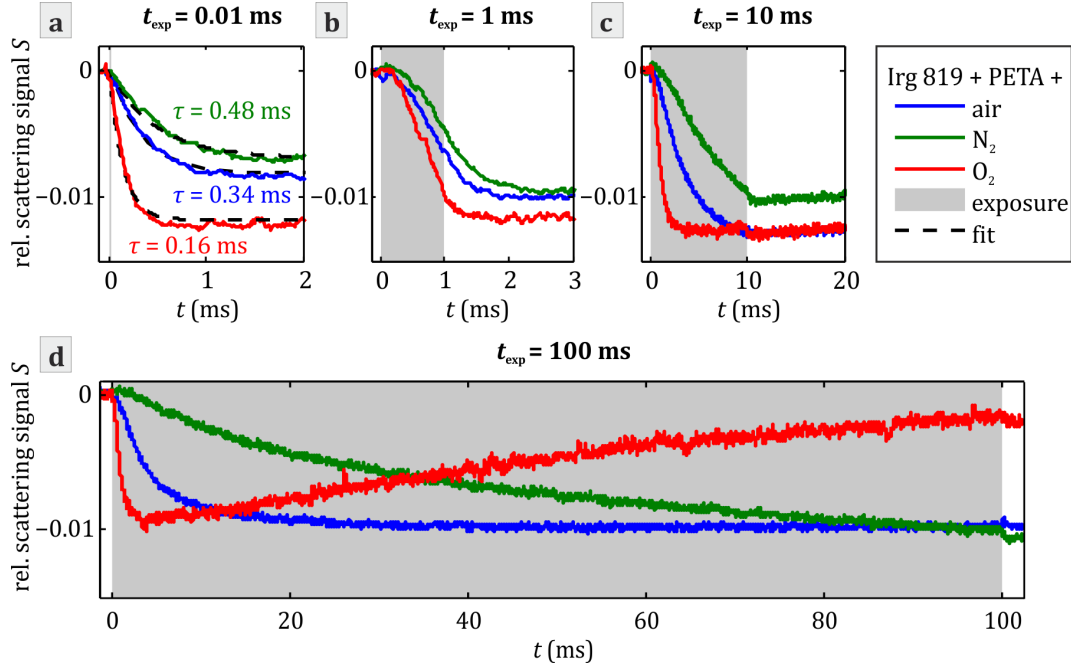
is short, but intense and highly localized, allowing for non-local effects such as diffusion to occur. In the case of film polymerization, a typical post-polymerization duration (Section 3.3.6) of hundreds of milliseconds has been observed [70], which is by far longer than typical exposure periods for DLW. Hence, it has been argued by different authors that the assumption of the polymerization to occur mainly after the end of the exposure (Section 3.3.6) would be satisfied [16, 57, 94]. For thin films, it has also been observed that polymerization only starts after a certain onset period which is required for the available oxygen to be consumed [70, 72].

Unfortunately, conventional methods for the detection of the polymerization progress are either not applicable for DLW or do not provide the required temporal resolution (Section 3.3.3). We therefore used a newly developed technique to detect the formation of polymer features by their scattering of a probe laser beam due to the different refractive indices of monomer and polymer, which is described in detail in Section 4.2.

The probe laser is detected with a relatively small solid angle in a “transmission”-type configuration, so that scattering by the forming polymer voxel leads to a decrease of the detector signal. As the magnitude of the detected signal change depends on both, the size of the feature and the magnitude of the refractive index change (which is expected to be related to the monomer conversion), the resulting signal change cannot be taken as a one-to-one measure for the monomer conversion at one specific point in space. Still, its temporal evolution can be interpreted as an indicator for the overall progress of the reaction within the volume of the voxel.

### 6.2.1 Polymerization Regimes for Different Exposure Periods

In order to facilitate the interpretation of the data, single dots (instead of lines) were written into the volume through exposure by one train of fs-pulses (80 MHz pulse repetition rate) with an overall exposure period  $t_{\text{exp}}$ . The signal-to-noise ratio is improved by averaging the signal over 400 events in all cases. In the experiment, we observed a decrease of the scattering signal by approximately 1% (corresponding to  $S = -0.01$  in our nomenclature) for a typical photo-resist (**Figure 6.5**). After a certain period, the scattering signal again reaches a steady state, corresponding to the end of the polymerization reaction. Typically,



**Figure 6.5:** Time dependent relative scattering signal  $S$  during the writing of single dots in the volume for different exposure periods. The oxygen content of the photo-resist is varied by bubbling with oxygen and nitrogen and sample sealing as described in the previous section. The writing laser power is chosen to be 10% above the writing threshold ( $P = 1.1 P_{\text{th}}$ ) in all cases. The “intrinsic” polymerization time constant  $\tau_{\text{p,intrinsic}}$  in the case of short exposure ( $t_{\text{exp}} = 0.01$  ms) is determined by fitting the signal with a function  $S_{\text{fit}} = \Delta S_{\text{max}} (1 - e^{-t/\tau_{\text{p,intrinsic}}})$ .

this is the case after a fraction of a millisecond with the precise value depending on the photo-resist composition and the exposure period. After the end of the exposure, the signal partly recovers on a much longer timescale (several tens of milliseconds, **Figure 6.5 c**, effect more pronounced in **Figure 6.7 c** and **Figure 6.8**). This effect is attributed to a movement of the written polymer features out of the probe beam focus due to thermal (Brownian) or convective motion as the features are not attached to the substrate. In the case of the oxygen-enriched photo-resist, a similar effect is even observed during the exposure for very long exposure periods (100 ms, **Figure 6.5 d**).

Please note that all measurements are taken at a writing power which is by 10% higher than the polymerization threshold for each specific resist (**Figure 6.1**) in order to compare situations with similar outcome in terms of the generated

polymer feature size. Accordingly, the writing laser power and hence, the radical generation rate largely varies for the different photo-resists and exposure periods.

When comparing the photo-resists with different oxygen content, it is obvious that the reaction duration decreases with increasing oxygen concentration for all examined exposure periods – most prominently in the cases with long exposure period.

For short exposures, the time span between the exposure and the settlement of the steady state can be measured by fitting the experimental data to a limited-growth model, i.e.  $S_{\text{fit}} = \Delta S_{\text{max}} (1 - e^{-t/\tau_{\text{p, intrinsic}}})$ . The polymerization duration in this case is independent from the exposure period  $t_{\text{exp}}$  if shorter exposure is compensated by a higher laser intensity to yield similar polymer structures (data not shown). In this sense, the duration of the polymerization can be interpreted as an “intrinsic” property of a certain photo-resist composition. Typical values of less than one millisecond are found ( $\tau_{\text{p, intrinsic}} = 0.16$  ms to 0.48 ms, **Figure 6.5 a**).

The exposure dose and, hence, also the starting radical concentration is matched to compensate for the difference in oxygen concentration of the different samples. Therefore, the fact that  $\tau_{\text{p, intrinsic}}$  still depends on the oxygen concentration indicates that even in this short-exposure regime, oxygen diffusion (and not bi-radical termination) finally terminates the polymerization reaction.

In Section 3.3.5, it is argued that for molecular oxygen one expects diffusion on a time scale of  $\tau_{\text{D}} \approx 2$  ms for a diffusion length of  $l_{\text{D}} = 150$  nm (a typical focus radius). The observed intrinsic polymerization duration is smaller by one order of magnitude roughly, corresponding to a diffusion length of around 50 nm. In practice, a minimum lateral feature diameter (not resolution) of around 100 nm–150 nm can typically be observed (e.g., 130 nm linewidth in **Figure 6.3 e**), so that this interpretation still is consistent with the experimental results.

If the exposure period is larger than the “intrinsic” polymerization duration  $\tau_{\text{p, intrinsic}}$ , the polymerization only starts after an onset time in the order of 100  $\mu\text{s}$  and continues after the exposure with a time constant similar to  $\tau_{\text{p, intrinsic}}$  (**Figure 6.5 b**). This onset period is being caused by the oxygen initially available in the reaction volume which has to be consumed by oxygen quenching before the polymerization can start. A yet different behavior is observed for long exposures of a few milliseconds or more (**Figure 6.5 c and d**). Here, the polymerization reaction already stops during the exposure. Obviously, light that hits the voxel after the end of the polymerization does not contribute to the initiation of the reaction and, hence, the overall reaction initiation becomes less efficient in terms of the required exposure dose. This behavior corresponds to

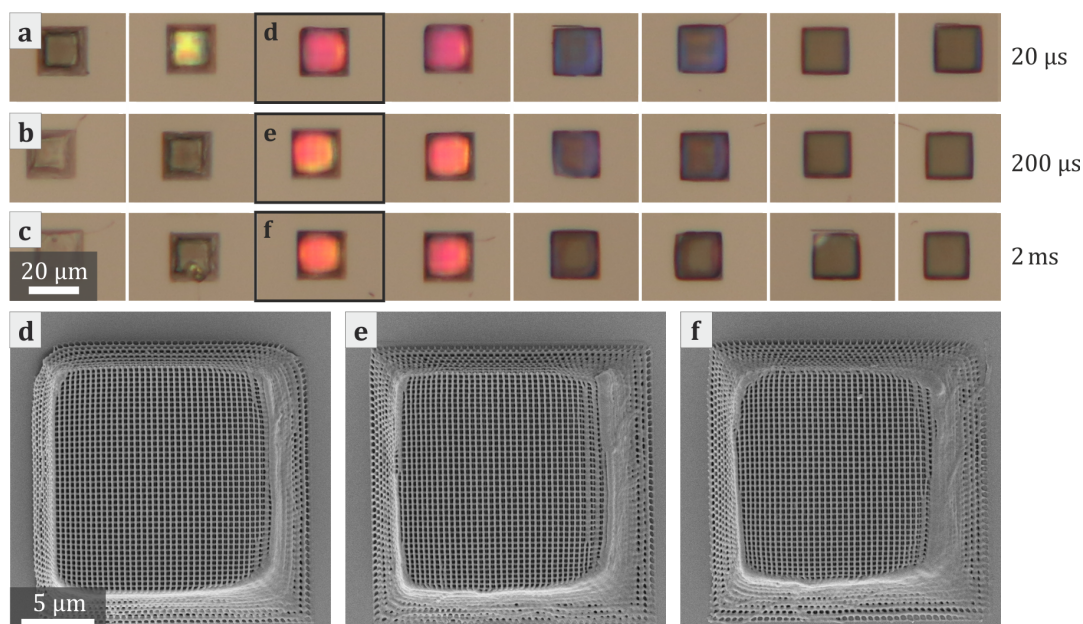


the Schwarzschild-regime, where oxygen diffusion dominates the overall process as described in the previous section. Namely, if the oxygen concentration is high, a large radical generation rate is required to overcome oxygen diffusion and therefore, the photo-initiator molecules within the reaction volume will be consumed relatively quickly. On the other hand, if there is only a small amount of oxygen in the system, a much smaller radical generation rate is sufficient to keep the polymerization going and hence, the photo-initiator will suffice for a much longer polymerization period.

### 6.2.1.1 Influence on the 3D-Resolution

While so far, the polymerization dynamics were only discussed with respect to the underlying mechanisms, it also is of interest how the structure quality correlates with the exposure period (or, equivalently, the writing velocity) and the polymerization duration. While the latter cannot be varied easily without changing a whole set of other experimental parameters (i.e., by using different chemicals), we can examine the writing resolution as a function of the exposure period for one given photo-resist. Therefore, once again woodpile photonic crystals were written as benchmark structures while varying the effective exposure period through the impressing of a duty-cycle onto the writing laser power (**Figure 6.6**).

Clearly, a short exposure period is favorable for the writing process, corresponding to writing in the regime where oxygen diffusion is not yet a limiting factor. Interestingly, this finding is in contradiction to the arguments given in the literature [117–119] (see also Section 6.1.1), namely, that quencher diffusion leads to a resolution improvement through a more pronounced quenching effect in the boundary area of the exposure region, and quencher diffusion is more pronounced for long polymerization durations. Apparently, some other effects including the already discussed photo-initiator saturation in the case of long exposures overcome the above-mentioned effect. Furthermore, the scanning electron micrographs in **Figure 6.6 d-f** indicate that structures written at low velocities suffer from more pronounced shrinkage, indicating a lower conversion in this case as well. These experimental results hence indicate that the achievable writing resolution for 3D structures also depends on parameters like structural stability (and not only on the actual “resolution” of the process in the sense of microscopy). From the applications’ side of view, however, this finding is a highly positive one, showing that high resolution structuring is not



**Figure 6.6:** Real color optical micrographs (illumination in reflection mode) of woodpile photonic crystals written as benchmark structures as in **Figure 6.3** into the standard photo-resist composition (PETA with 1% of Irgacure 819). In order to emulate the variation of the exposure period for a single dot exposure while still writing continuous lines, these structures are fabricated with a duty cycle of **a)** 1%, **b)** 10%, and **c)** 100%. The duty cycle is set through varying the duration of pulse trains at a pulse train repetition rate of 2 kHz. This way, the writing velocity can be kept constant (100 μm/s), which corresponds to an effective exposure period of approximately 0.02 ms (**a**), 0.2 ms (**b**), and 2 ms (**c**). The average writing power during the pulse burst is 2.0 mW (**a**), 4.3 mW (**b**), and 8.6 mW (**a**), respectively, for the structures in the very left column, and is increased from left to right steps of 1% per column. Scanning electron micrographs of selected structures are depicted in **d)**-**f)**. The nominal lateral distance of adjacent rods is 450 nm. Reproduced from [110]. ©2014 Wiley VCH.

in contradiction to high writing velocities or, in other words, that the overall sample throughput can in principle be increased without sacrificing structuring quality.

### 6.2.2 Comparison of Different Photo-Resist Compositions

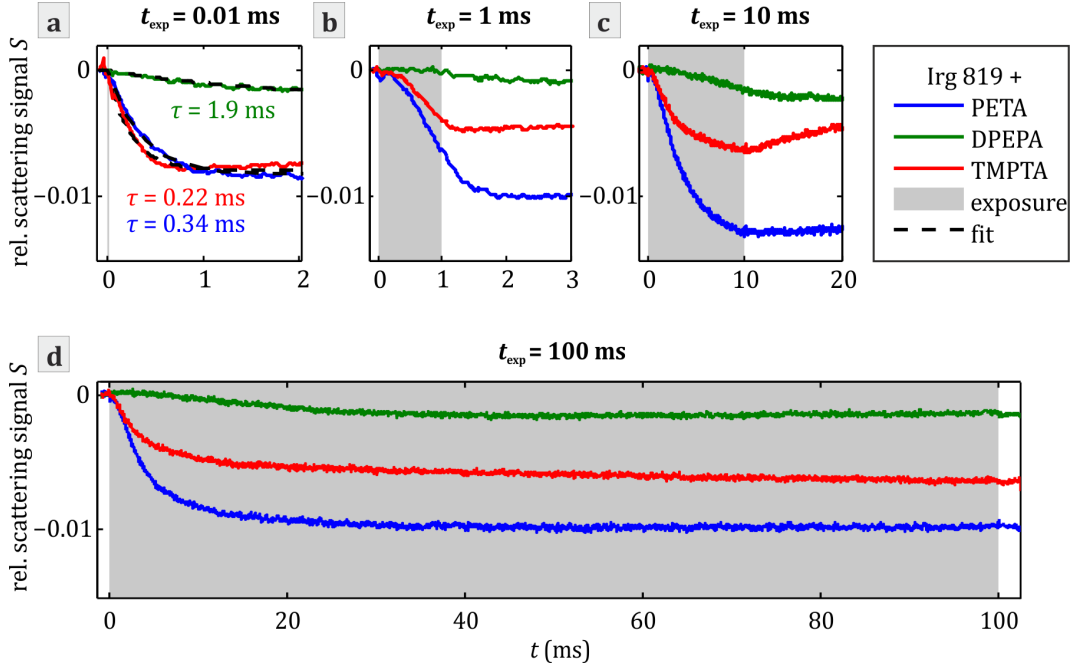
In order to see whether this behavior would also apply for other photo-resist compositions, a larger set of different photo-resist compositions with either exchanged monomer or exchanged photo-initiator was investigated in a similar way. For the investigation of the monomer influence, PETA was compared to the multifunctional acrylates TMPTA, PETTA, and DPEPA, as well as the diacrylates BA and PEG-DA (average molar weight  $M_n$ 700) and the methacrylate TMPTMA, all sensitized by 1.00% (mol.) of Irgacure 819 (**Figure 6.7**).

As the formulation with PETTA shows very similar behavior compared to PETA, the corresponding data are not depicted. Furthermore, no writing is possible at exposure periods of less than approximately 10 ms in the cases of TMPTMA, PEG-DA and BA. Therefore, these also are not included. Please note that for DPEPA, the presented data correspond to a writing laser power which is 50% larger than the polymerization threshold (compared to 10% for all other photo-resists), as otherwise no signal change can be detected due to the small refractive index change during the polymerization reaction in this monomer.

While the basic mechanisms as described above (i.e., onset behavior, intrinsic polymerization time and photo-initiator saturation) can be found in all cases, the timescales of these effects vary. This is not very surprising, as also the viscosity of the different monomers changes by roughly one order of magnitude going from TMPTA to PETA and from PETA to DPEPA.<sup>3</sup> As the above-mentioned effects and also the reaction rates for chain propagation and termination are diffusion-dependent, it is not very surprising that not only the intrinsic polymerization duration (**Figure 6.7 a**), but also the length of the onset period (e.g. **Figure 6.7 c**) is increased if the viscosity is larger.

---

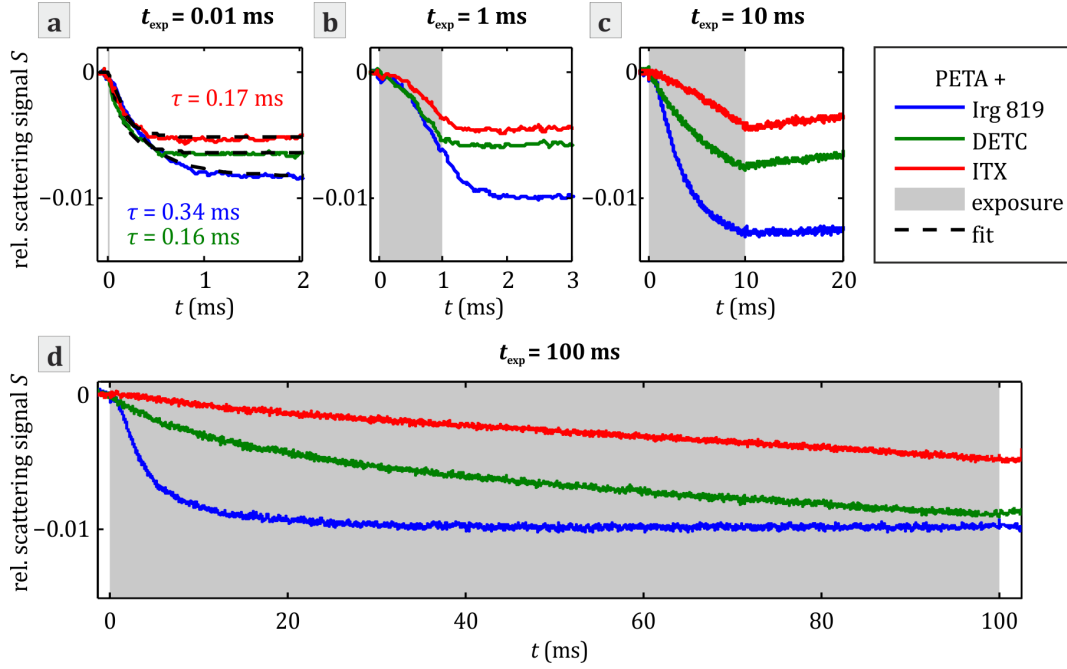
<sup>3</sup> Dynamic viscosity (25° C) of TMPTA: 0.08 – 0.12 Pa s, PETA: 0.6 – 1.0 Pa s, and Dipentaerythritol hexaacrylate (a close relative of DPEPA): 7 – 12 Pa s. Viscosity data taken from <http://www.union-pigment.com/china/radiation-curable.html>, retrieved on March 25, 2015.



**Figure 6.7:** Time dependent relative scattering signal  $S$  during the writing of single dots in the volume for different exposure periods for photo-resists with different monomers. The writing laser power is chosen to be 10 % above the writing threshold ( $P = 1.1P_{\text{th}}$ ) in all cases except for the monomer DPEPA with  $P = 1.5P_{\text{th}}$ , as in this case, the refractive index change is so small that no signal change could be observed otherwise. The “intrinsic” polymerization time constant  $\tau_{\text{p,intrinsic}}$  in the case of short exposure (0.01 ms) is determined by fitting the signal with a function  $S_{\text{fit}} = \Delta S_{\text{max}} (1 - e^{-t/\tau_{\text{p,intrinsic}}})$ . The curves for PETA and Irgacure 819 from **Figure 6.5** are included for comparison.

To investigate the influence of the photo-initiator, we compare the reference composition containing 1.0 % (mol.) of Irgacure 819 to photo-resists with 3.7 % (mol.) of Irgacure 369, 1.3 % (mol.) of Darocur TPO, 0.26 % (mol.) of DETC, and 1.0 % (mol.) of ITX, respectively (all based on PETA, **Figure 6.8**). The formulations with the commercial Irgacure and Darocur photo-initiators show very similar behavior, so that only Irgacure 819 is included in the graph.

For the unconventional Norrish type II photo-initiators DETC and ITX, we find that the intrinsic polymerization time is shorter compared to Irgacure 819, while photo-initiator saturation effects are less pronounced. The reason for this



**Figure 6.8:** Time dependent relative scattering signal  $S$  during the writing of single dots in the volume for different exposure periods for photo-resists with different photo-initiators. The writing laser power is chosen to be 10% above the writing threshold ( $P = 1.1 P_{\text{th}}$ ) in all cases. The “intrinsic” polymerization time constant  $\tau_{\text{p,intrinsic}}$  in the case of short exposure (0.01 ms) is determined by fitting the signal with a function  $S_{\text{fit}} = \Delta S_{\text{max}} (1 - e^{-t/\tau_{\text{p,intrinsic}}})$ . The curves for PETA and Irgacure 819 from **Figure 6.5** are included for comparison.

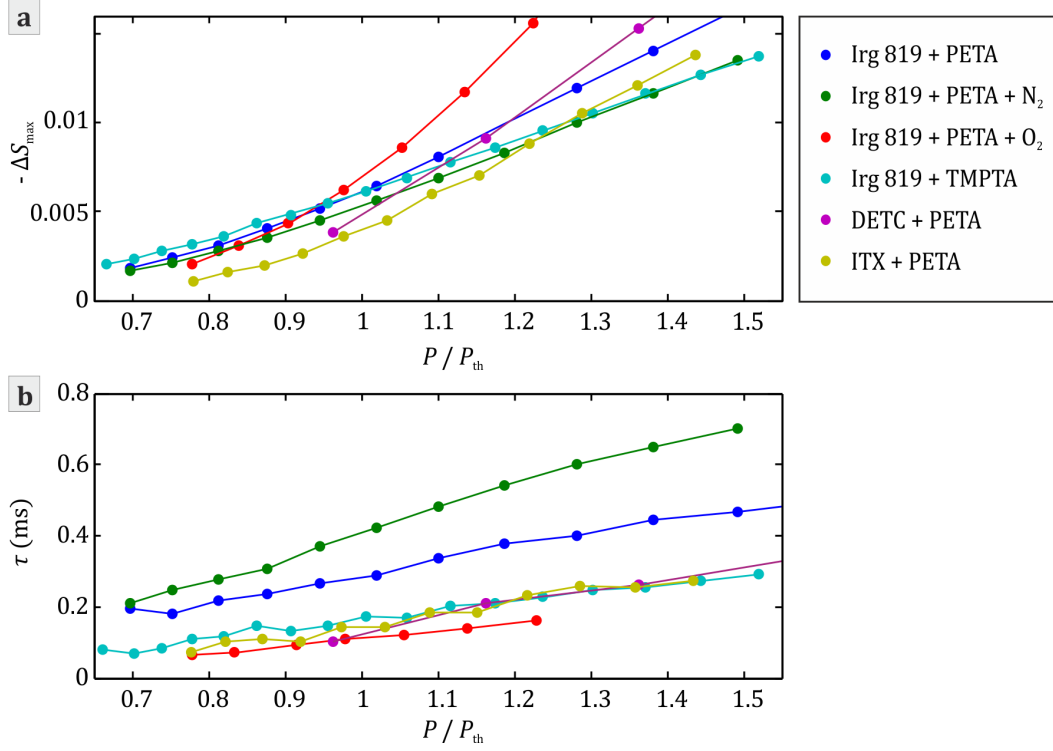
behavior is not perfectly clear as both, the different relative concentrations of photo-initiator and oxygen as well as the quenching efficiencies are different for the different photo-initiators. In this context, one should also have in mind that two distinct quenching mechanisms have been proposed for oxygen, namely radical inhibition and triplet quenching (Section 3.2.4). These may influence the overall reaction differently for the different photo-initiators. For example, the triplet lifetime of DETC and ITX is supposed to be much larger than for Irgacure 819 (Section 3.1.3), so that triplet quenching is expected to yield a larger contribution in these cases. In addition, the higher effective nonlinearity of the absorption process ( $N = 3$  compared to  $N = 2$ ) may lead to smaller dimensions of the polymer features and hence, quantitatively different reaction dynamics. Moreover, we find that the saturation behavior (**Figure 6.8 d**)

for DETC and especially for ITX is less pronounced than for Irgacure. This is consistent with the less distinct plateau formation for the polymerization threshold at long exposures (**Figure 6.2 a**), indicating that saturation effects through oxygen diffusion are less pronounced for these photo-initiators.

So far, all displayed curves correspond to similar exposure doses in terms of the structuring result. However, the relative laser power  $P/P_{\text{th}}$  can easily be varied in order to study the threshold behavior of the polymerization reaction. Experimentally, we find very similar qualitative results for all investigated photo-resists. In order to yield a quantitative and compact analysis, the fitting parameters  $\Delta S_{\text{max}}$  and  $\tau_{\text{p, intrinsic}}$  from the limited growth model for short exposure periods are displayed as a function of the laser power (**Figure 6.9**). These quantities correspond to the signal change at the end of the polymerization reaction and the corresponding time constant, respectively, in the case of very short exposures.

As expected, the amplitude of the signal change is increased with increasing laser power, corresponding to an increase in conversion and/or feature size (**Figure 6.9 a**). The slope of this curve seems to correlate with the nonlinearity of the absorption process, i.e., for the Norrish type II initiators DETC and ITX, the curve is steeper as compared to the Irgacure photo-resists. The oxygen-enriched photo-resist represents an exception, as it yields a similarly steep slope, even though a normal two-photon behavior is expected. However, systematic errors for the measurement of the polymerization threshold may not be excluded in this case, caused by a potentially imperfect sealing of the sample, which leads to a decrease in oxygen concentration and hence, a drastic shift of the polymerization reaction during the experiment through leaking oxygen.

Interestingly, a signal change can already be observed well below the writing threshold ( $P \approx 0.7 P_{\text{th}}$ ) for all photo-resists, while after washing of such a sample, no polymer structures remain. This very clearly indicates that the polymerization reaction itself is a continuous process, while the rather sharp threshold formation behavior stems from the rather abrupt change in solubility when a certain degree of cross-linking is exceeded. As described in Section 3.3.1, such behavior can be explained on the basis of a percolation model, where the cluster size increases disruptively at a critical percolation probability, or, in other words, a critical monomer conversion.



**Figure 6.9:** Fitted polymerization parameters as a function of the relative writing laser power  $P/P_{th}$  for different photo-resist compositions in the case of short exposure periods ( $t_{exp} = 0.01$  ms) according to the limited growth model.: **a)** Amplitude of the maximum signal change  $-\Delta S_{max}$ . **b)** Intrinsic polymerization duration  $\tau_{p, intrinsic}$ . The threshold power is taken from the data displayed in **Figure 6.1** and **Figure 6.2**. The values for the photo-resist based on DPEPA are not displayed as they lie outside the plotting area for the most part. Please note that a quantitative analysis of the slope of the curves in panel **a** according to Equation (3.5) is not possible as the signal change depends not only on the monomer conversion, but also on the feature size of the written voxel.

The intrinsic polymerization duration is also elevated with increasing writing power, indicating that the size of the oxygen depletion region is larger if more starting radicals are supplied and, hence, the polymerization reaction is supported for a longer time (**Figure 6.9 b**). This once more supports the interpretation that the termination of the polymerization reaction is dominated by oxygen quenching, as if the polymerization was stopped due to bi-radical termination reactions at high monomer conversion, the reaction would slow down faster if the radical concentration was increased.

### 6.3 Numerical Modeling of the Reaction Kinetics

Extensive effort on the quantitative numerical modeling of the reaction kinetics of photo-polymerization has been reported in literature, including thermal effects, conversion dependent reaction rates, chain transfer-mediated termination, reaction quenching by inhibiting species such as atmospheric oxygen and molecular diffusion [73, 75, 76, 81]. For the experimental retrieval of reaction parameters to feed these models (such as reaction rates for the different partial reactions), an enormous set of experimental data is required, typically including time-dependent measurements of the monomer conversion and concentrations of the reagents as well as parameter studies. While elaborate kinetic models for 3D-DLW have been developed as well [34, 83, 95], their predictive power is still limited for two main reasons. First, the underlying database from experiments is relatively small, as many analysis techniques which are applied for photo-polymerization on larger scales cannot be applied. Second, and more importantly, the reaction kinetics of DLW can only be described properly when the inhomogeneous nature of the process is being accounted for, so that effects such as diffusion can be included properly. This drastically increases the complexity and, hence, the number of degrees of freedom for such models. Furthermore, the rate equations now must be solved in time and also in space.

In order to still provide the qualitative process description presented in the previous sections on a more quantitative basis, we chose a slightly different approach than these previous works [83, 95]. Namely, we try to find the “simplest working model” that allows to quantitatively reproduce the experimental results at least for one specific photo-resist. Obviously, the reaction model will be (over-) simplified in such a case and hence, the resulting parameters cannot necessarily be compared to other, more elaborate studies.



However, from the given basis of experimental data, a more complex model would most likely lead to over-fitting and is therefore not considered to be very insightful.

The developed model is based on the time-dependent solution of the rate equations of polymerization described in Section 3.2.1. While originally other partial reactions such as different termination pathways were included as well, it is found that radical generation, conversion, oxygen quenching, and oxygen diffusion suffice to explain the underlying set of experimental results. The corresponding species and initial concentrations as well as the reaction equations and rate coefficients are given in Table 6.1 and Table 6.2, respectively. Furthermore, the reaction is assumed to occur homogeneously within the reaction volume, with oxygen diffusion being accounted for through the exchange with an infinite reservoir (i.e. with a constant oxygen concentration  $[\text{O}_2]_0$ ).

The model is fitted to the experimental data displayed in **Figure 6.1** and **Figure 6.5**. More precisely, the polymerization threshold  $P_{\text{th}}(t_{\text{exp}})$  for three selected exposure periods (0.01 ms, 1 ms, and 10 ms) and the overall duration of the polymerization in the case of short and long exposure periods (0.01 ms and 10 ms) are selected as numerical input parameters. The fitting is then done on the basis of five degrees of freedom, namely the initial oxygen concentration (Table 6.1) and the four reaction rate coefficients (Table 6.2). In order to account for the fact that the effective chain length changes drastically with the increasing monomer conversion, a correction factor for the monomer conversion is extrapolated from literature data (**Figure 6.10**) [74].

We find that such a model is able to numerically reproduce the results from Section 6.1 and Section 6.2 with good qualitative and quantitative agreement. All previously discussed effects can be found and confirmed in the numerical model, such as the Schwarzschild behavior (**Figure 6.11**) at long exposure periods, or the time-dependence of the monomer conversion (**Figure 6.12**). As discussed in the previous section, at short exposure periods (**Figure 6.12 a**), a certain fraction of the photo-initiator molecules is excited to radicals very quickly, leading to the fast depletion of oxygen in the reaction volume. During this first period ( $\approx 0.03$  ms), the radical concentration decays to roughly 80 % of the peak value. Polymerization then propagates until all radicals are consumed

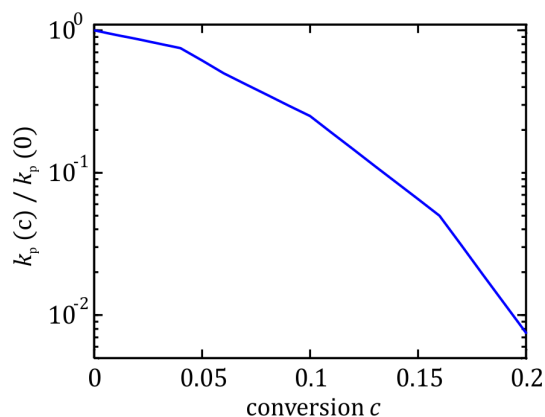
For the sake of simplicity, the polymerization is not modeled as a chain growth reaction. Instead, a bi-molecular reaction of a single monomer unit with initiator radicals serving as catalyzers is assumed. Hence, the formation of connected chains, clusters and networks is not incorporated in this model, however, so that the output of the model is the monomer conversion rather than an average chain length.

**Table 6.1:** Chemical species considered for the simple numerical kinetic model. X denotes an (arbitrary) chemically inert species that does not take part in any further reaction steps. Where applicable, initial concentrations are given. While for the photo-initiator and the monomer, these are based on the photo-resist used in the experiments, the initial oxygen concentration serves as one of the degrees of freedom in the numerical model.

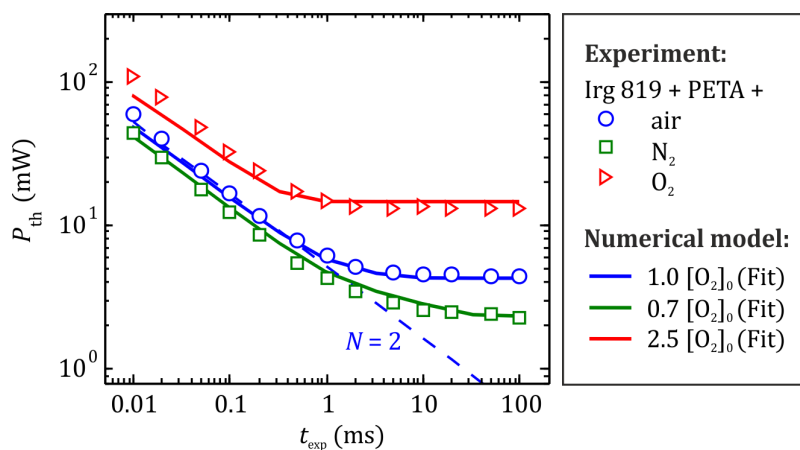
Chemical Species	Symbol	Initial Concentration
Photo-initiator	I	$[I]_0 = 4 \cdot 10^{-2}$ mol/l
Radical	R·	–
Monomer	M	$[M]_0 = 4$ mol/l
Polymer	P	–
Oxygen	O <sub>2</sub>	$[O_2]_0 = 6 \cdot 10^{-3}$ mol/l
Inert species	X	–

**Table 6.2:** Simplified rate equations for the polymerization reaction in the numerical model. The reaction rates are obtained from the model as free fit parameters. As the polymerization cannot be described by linear chain growth in the case of highly cross-linking monomers, the monomer and polymer concentrations are considered as concentrations of unbound and bound functional groups, respectively. In order to reproduce the resulting effects, the changing propagation rate due to the increasing chain-length is accounted for by assuming the time-dependent conversion dependence from **Figure 6.10**. In this case, the starting value at zero conversion  $k_{p,0}$  serves as a fit parameter.

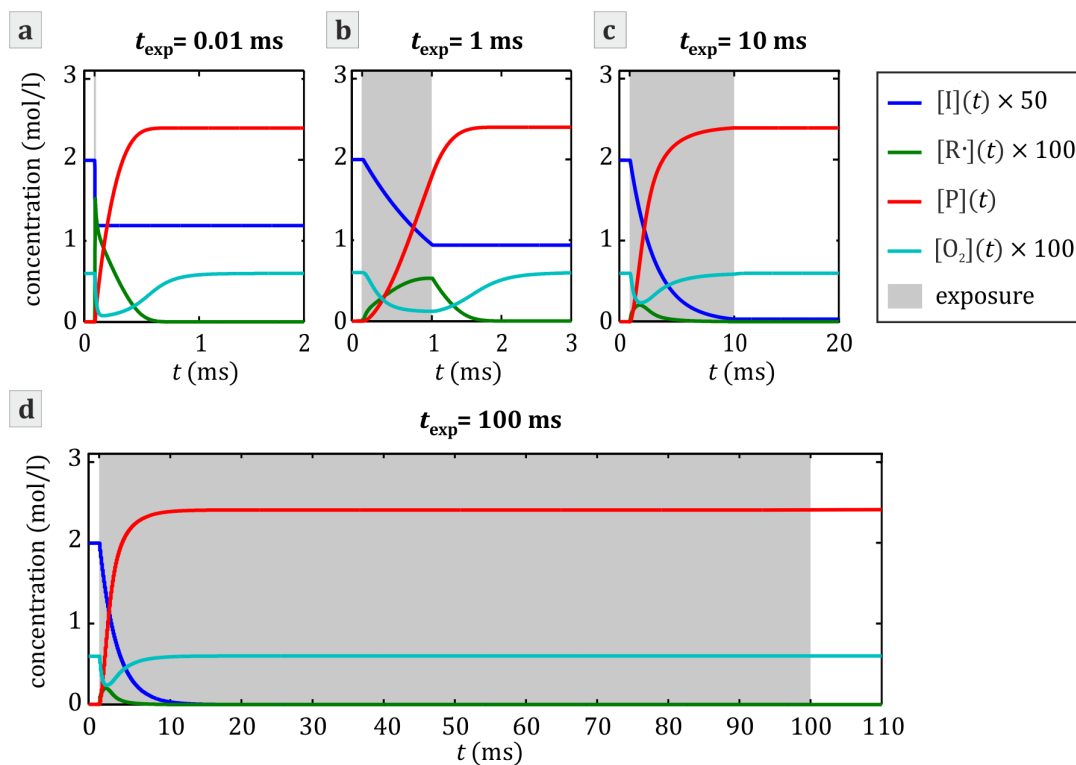
Reaction	Chemical Equation	Reaction Rate
Radical generation by 2PA	$I + 2\gamma \rightarrow R\cdot$	$k_i = \alpha P^2$ with $\alpha = 0.007$ l/(s mW <sup>2</sup> )
Propagation	$R\cdot + M \rightarrow R\cdot + P$	$k_{p,0} = 4.3 \cdot 10^4$ l/(mol s)
Oxygen quenching	$R\cdot + O_2 \rightarrow X + O_2$	$k_q = 2.6 \cdot 10^6$ l/(mol s)
Oxygen diffusion	$O_{2, \text{surrounding}} \leftrightarrow O_2$	$k_d = 3 \cdot 10^3$ l/s



**Figure 6.10:** Conversion dependence of the propagation rate  $k_p$ , data points extrapolated from [74]. The initial value  $k_{p,0}$  is obtained as one of the fit parameters for the numerical model. Reproduced from [110]. ©2014 Wiley VCH.



**Figure 6.11:** Experimental data from **Figure 6.1** as well as calculated polymerization threshold for three selected oxygen concentrations with otherwise unchanged reaction parameters. The oxygen-related threshold shift and the Schwarzschild-effect can both be reproduced from the model. Reproduced from [110]. ©2014 Wiley VCH.



**Figure 6.12:** Calculated time-dependent concentrations of the reagents for the fitted oxygen concentration (corresponding to the photo-resist with PETA and Irgacure 819 under standard atmosphere). Except for the polymer, the curves are scaled for the relatively small concentrations of initiator, radicals and oxygen to be visible. The polymer formation (red curve) shows both qualitatively and quantitatively a very similar behavior to the scattering signal change in **Figure 6.2**. Reproduced from [110]. ©2014 Wiley VCH.

by oxygen quenching after roughly 0.5 ms, although with decreasing velocity due to the ongoing radical consumption.

For a medium exposure period (**Figure 6.12 b**), the onset period (build-up of the oxygen-depleted zone) takes longer ( $\approx 0.1$  ms), as the radical generation rate is lower due to the decreased laser power. In the previous section, this effect was described as the onset time of the polymerization. In the cases of long exposure (**Figure 6.12 c and d**), the photo-initiator molecules are totally consumed after a period of roughly 10 ms. Hence, the writing laser power which is necessary to overcome the polymerization threshold does not change when the exposure period is further increased as there are no photo-initiator molecules left to generate radicals.

When comparing the numerical results to literature data, we only find a very rough coincidence. For example, for TMPTA,  $k_q \approx 10^9$  l/(mol s),  $k_p \approx 10^3$  l/(mol s), and  $[O_2]_0 \approx 10^{-3}$  mol/l have been reported [70]. However, our model is simplified in many ways (e.g., by neglecting the different reactivities of different radicals and the conversion dependence of most other reaction rates, among others) and refers to a highly different experimental situation, so that the results most likely cannot be compared directly.

All in all, the presented model is able to reproduce the experimental result qualitatively and quantitatively as intended. To our understanding, this indicates that all other than the discussed mechanisms (e.g., bi-radical termination) can indeed be neglected in the investigated regime.



# 7 Chapter 7

---

## Parameter Studies Revisited

This last chapter is to some degree out of the main line of this thesis. Namely, it does contain no or only little “new” insights into the polymerization mechanism. Instead, experimental results from the early phase of this thesis are presented and discussed in the lights of the experiments described within the previous section (which, from a chronological perspective, are more recent). For this reason, the experiments within this chapter are not fully consistent with the ones presented previously in that the investigated experimental parameters and photo-resists differ partly.

At the time, we did not understand where the effects shown in the following emerged from: However, they can nowadays be explained at least qualitatively on the basis of the “state-of-the-art” polymerization model developed in the previous chapters. From a historical perspective, the main reason is that, at the time, a deeper understanding of the polymerization dynamics was lacking and hence, only explanations on the basis of the initiation mechanism were considered. Obviously, these attempts failed whenever the effective dynamics of the polymerization reaction altered the results when compared to the simple threshold model. The given examples are intended to show exemplarily how the discussed polymerization mechanisms influences the DLW procedure. At the same time, examples are given for experiments that – taken by themselves – did not turn out insightful for a better understanding of DLW.

For the presented experiments within this chapter, we used a slightly different set of photo-resists than for the experiments presented before for historical reasons.

Namely, these photo-resists are based on PETTA instead of PETA,<sup>1</sup> and contain 1 % (mol.) of either of the photo-initiators Irgacure 369, Irgacure 819, DETC, and ITX.<sup>2</sup>

## 7.1 Photo-Initiator Concentration

While screenings of the photo-resist composition with respect to additives such as co-initiators and inhibitors are part of the previous chapters (Section 5.3.2 and Section 6.1.2, respectively), a seemingly more obvious investigation of the photo-initiator concentration was not presented there. The reason is quite simple: The corresponding results are found to be not very helpful to understand the polymerization mechanisms. In this section, a part of these results will be presented by discussing the writing threshold for the two photo-initiators DETC and ITX, as for these, the range of concentrations where DLW is possible is the largest. This range in general is limited by two effects. Towards low concentrations, the dynamic range decreases until finally micro-explosions prohibit structuring at all. On the other side, the maximum concentration is limited by the finite solubility of the photo-initiator in the monomer.

If one includes the photo-initiator concentration  $c_{\text{init}}$  in the threshold model from Section 3.3.1 in order to find the corresponding scaling behavior, Equation (3.4) and Equation (3.5) can be adapted to

$$c_{\text{rad}} \propto c_{\text{init}} D \propto c_{\text{init}} \tau R E_{\text{p}}^N \quad (7.1)$$

and

$$\log(E_{\text{p, threshold}}) = -N \log(c_{\text{init}} \tau R / c_{\text{rad}}) + c, \quad (7.2)$$

respectively, with  $c_{\text{rad}}$  being the concentration of radicals that are generated. As discussed in Section 5.1,  $N = 3$  seems valid for both, DETC and ITX.

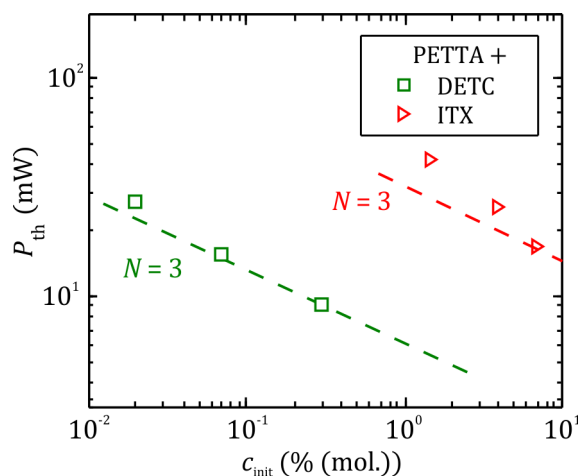
As can be seen from the results presented in **Figure 7.1**, the writing threshold indeed decreases with increasing photo-initiator content. However, the

---

<sup>1</sup> PETTA tends crystallize faster if kept at room temperature (with otherwise very similar properties with respect to DLW), and was therefore replaced by PETA for later experiments.

<sup>2</sup> Irgacure 819 was preferred to Irgacure 369 later on as it offers a reduced auto-fluorescence, which is preferential for some applications. For DETC, a smaller concentration (0.25 % (mol.)) turned out to yield better results for STED-DLW.





**Figure 7.1:** Writing threshold power as a function of the photo-initiator concentration. Straight lines (dashed) indicate the expected behavior according to Equation (7.2) for both photo-initiators. For experimental reasons (Section 7.3), the experiments were performed with an air objective (63 x, NA = 0.75) on the (otherwise unchanged) MaiTai-Setup by writing lines with a velocity of 100  $\mu\text{m/s}$ .

experimental data deviate from the expectation in both cases, indicating a comparatively higher threshold power at lower concentration. In other words, the reaction is less efficient if the initiator concentration is low. The reason is that, due to the oxygen within the photo-resist, photo-initiator depletion must be considered as well (Section 6.3). More precisely, Equation (7.2) only holds if the amount of radicals generated is small compared to the available initiator concentration and the photo-initiator consumption can be neglected, which apparently is not the case. The on-set of this saturation effect not only depends on the relative concentrations, but also on the relative efficiency for the initiation of chain-growth and oxygen quenching for the specific photo-initiator species.

From an applications point-of-view, it therefore seems obvious that a high photo-initiator concentration is desirable. However, it is found in practice that the photo-initiator then tends to fall out after some time even if it was initially soluble (usually within days or weeks), leading to “solid dirt” on the samples. Ideal photo-initiator concentrations for new initiator species therefore have to be determined through experiments and usually represent a compromise with respect to the above-mentioned effects.

## 7.2 Writing Velocity

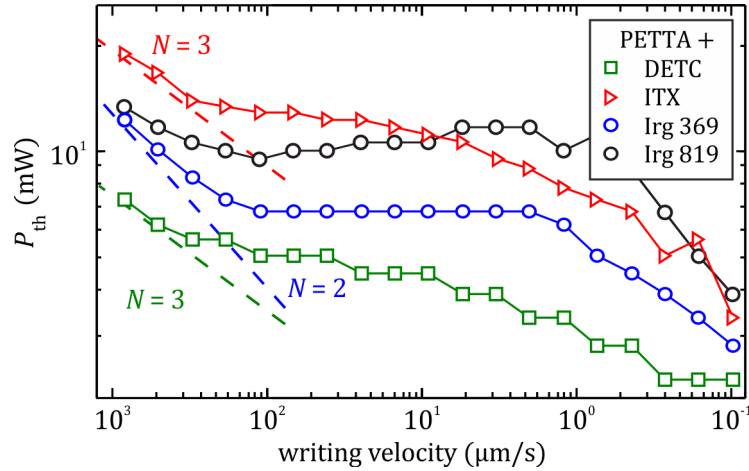
Another writing parameter that can easily be varied is the writing velocity (sometimes also referred to as scan speed). Intuitively, one would think that a variation of the writing speed is very similar to the variation of the exposure period. A typical size of the writing laser focus is  $d_{\text{voxel}} = 330 \text{ nm}$  (FWHM), hence, writing with a certain velocity (e.g.  $100 \mu\text{m/s}$ ) should correspond to an exposure period of  $t_{\text{exp}} = d_{\text{voxel}}/v$  (here  $3.3 \text{ ms}$ ). In that case, a scaling behavior according to Equation (3.5) would explain the experimental results. However, this is not the case in many situations for DLW. For example, for commercial *IP-L* photo-resist (*Nanoscribe*), neither one- nor two-photon absorption can explain the dependence of writing threshold and line thickness on the writing velocity [39]. Moreover, even an extended model introduced by these authors, including two-photon absorption and an additional fixed writing threshold (as it would be caused by oxygen quenching if diffusion was neglected) could not explain the results satisfactorily.

Within this thesis, a similar experiment was performed for non-commercial photo-resists, including a wider span of writing velocities and the above-mentioned set of different photo-resists. Typical results are given in **Figure 7.2**. A double-logarithmic representation with inverted horizontal axis is chosen in order to provide comparability with **Figure 6.1** and **Figure 6.2**. Since the available setups at the time were not equipped with galvanometric scanning mirrors, the writing velocity is limited to a maximum value of approximately  $1000 \mu\text{m/s}$ . On the other side, the measurement range extends down to  $0.1 \mu\text{m/s}$ , corresponding to  $t_{\text{exp}} = 0.4 \text{ ms}$  and  $t_{\text{exp}} = 40 \text{ s}$ , respectively. Hence, the data set is “shifted” for longer exposures by approximately 1.5 decades as compared to **Figure 6.1** and does not cover the case where the effective exposure period is clearly shorter than the polymerization duration.

Still, it can be seen that the curves converge towards the expected scaling behavior towards high writing velocities. For velocities in the range of  $100 \mu\text{m/s}$  to  $1 \mu\text{m/s}$  (which are typically applied for DLW with piezo-electric stages), the “Schwarzschild”-effect described in Section 6.1.1 can be reproduced. At very low writing velocities however ( $v \lesssim 1 \mu\text{m/s}$ ),<sup>3</sup> the writing threshold once again decreases. In the case of Irgacure 819, it can even be seen that the threshold power is increased slightly when decreasing the writing speed from  $100 \mu\text{m/s}$  to  $5 \mu\text{m/s}$ .

---

<sup>3</sup> In Chapter 6, this regime was not investigated as it is of little interest for applications due to the long overall structuring durations for most structures of interest.



**Figure 7.2:** Polymerization threshold as a function of the writing velocity. When dashed lines are written close to the substrate with varying writing laser power, the threshold is associated with the lowest writing laser power that is visible when judged by a light microscope image. While for the Irgacure photo-initiators, a scaling with  $N = 2$  is expected from Equation (3.5),  $N = 3$  seems plausible for DETC and ITX (dashed lines). However, all curves heavily deviate from the expected behavior due to oxygen quenching and diffusion effects. Experiments were performed on the MaiTai-Setup.

While this behavior seems highly dubious at first sight, we find that it goes along with pronounced proximity effects. I.e., the writing threshold does depend on exposure events that occurred previously in the vicinity of the written dot. As such effects often lead to problems for the writing more complex structures, they will be discussed in a separate section on the basis of the same experimental data set.

### 7.2.1 Proximity Effects

So-called proximity effects are known for many lithography systems, where the writing threshold is either reduced or increased in the vicinity of already written features. As these effects are mostly reproducible but not easy to predict, systems with little or even no proximity effects are highly preferred for applications. For DLW, such effects have also been observed, especially at low

writing velocities.<sup>4</sup> In this chapter, two examples will be discussed on the basis of the same experiments as presented in the previous section. While the focus of the previous section was on the quantitative analysis, the more qualitative discussion in terms of structure quality will be in the foreground here.

Scanning electron micrographs are given for two exemplarily chosen photo-resist compositions (**Figure 7.3**). In the case of the DETC-based photo-resist, little or no self-interaction effects can be seen. Even at low writing powers, lines look smooth and homogeneous. Furthermore, no significant change in the line thickness is observed when comparing different writing velocities, as long as the writing power is adapted accordingly.

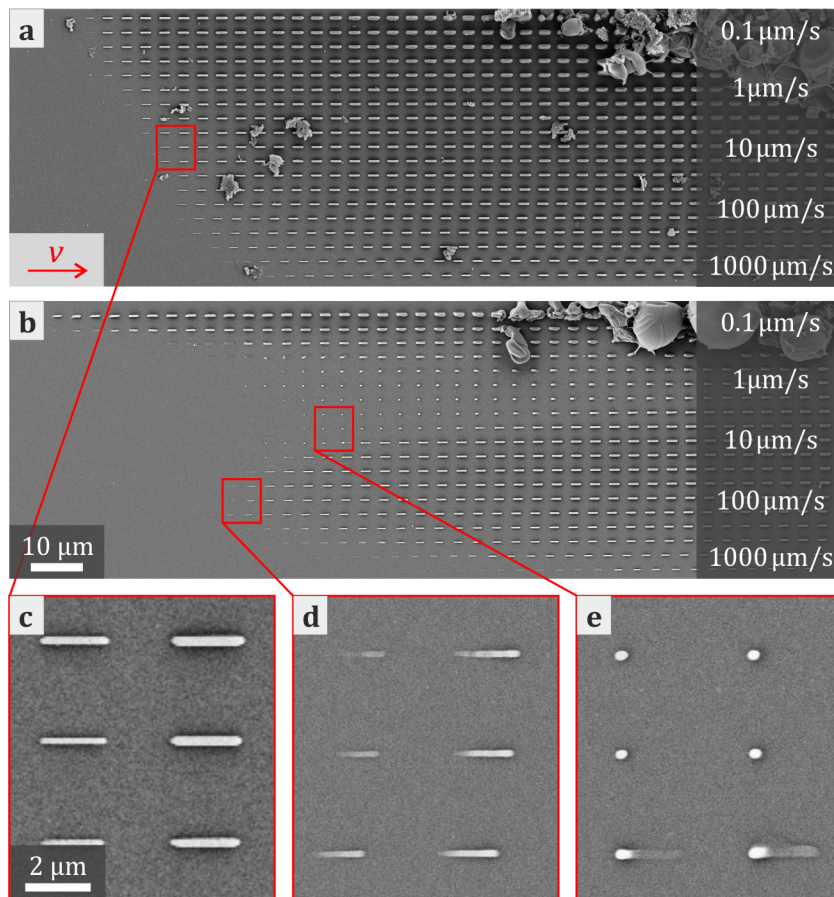
In sharp contrast, we see a pronounced effect in the case of Irgacure 819 as photo-initiator. Interestingly, “positive” and “negative” proximity effects can both be seen, albeit at different writing velocities. This effect is most prominent at velocities between  $0.5 \mu\text{m/s}$  and  $10 \mu\text{m/s}$ , where at low laser powers, only a single dot is written where the line should start. If the writing power is increased, the line follows to the dot like a weaker “tail”.

At higher writing velocities around  $100 \mu\text{m/s}$ , we find the opposite behavior. Namely, the lines are quite thin at the starting point and reaches some kind of “steady-state” in thickness after a fraction of a micrometer. The latter effect can be explained once again by oxygen diffusion. Namely, with the start of the line writing, an oxygen depletion zone is created through oxygen consumption by radical quenching. As polymerization is dominated by oxygen diffusion in this case, the extent of this (almost) oxygen-free zone is larger than the writing laser focus. At the same time, as the line is written continuously, it will be drawn along the writing laser focus as it proceeds through the sample. Hence, the line-start effect corresponds to the build-up time of this oxygen depletion region and will lead to an increased writing threshold until it reaches its (quasi-)steady-state.

In the first case, however, where only a single dot is observed at the start of the line, the mechanism appears more complex. One possible explanation would be that in this case, the writing of features is only enabled by diffusion of the photo-initiator. As discussed in Section 3.3.5, we expect the initiator diffusion

---

<sup>4</sup> Traditionally, the term proximity effect mostly refers to interaction effects for two adjacent, but distinct features. For DLW, such effects are more prominent as “self-interaction effects”, i.e., the writing of different parts of the same feature (in this case, a line) interacts. As the origin and nature of these effects is very similar, we will not distinguish between these effects in the following



**Figure 7.3:** Scanning electron micrographs of the writing velocity test patterns from Section 7.2 for **a,c)** DETC and **b,d,e)** Irgacure 819. The writing power for the dashed lines is increased linearly from the left to the right, while the writing velocity is increased logarithmically as indicated. While no proximity effects can be observed for DETC (**c**), a delayed line-start (**d**) or even a self-depletion effect (**e**) can be observed for Irgacure 819 at different writing velocities.

to only play a role on the time-scale of  $\tau_d \approx 20$  ms or more, which corresponds to a velocity of  $v \approx 16 \mu\text{m/s}$  by the argument given above ( $\tau_d \approx 2$  ms or  $v \approx 160 \mu\text{m/s}$  for oxygen). Therefore, one might expect that, if the initial photo-initiator concentration is not sufficient to start the polymerization due to oxygen diffusion, a sufficient amount of radicals can only be generated through photo-initiator diffusion (all within the oxygen-depleted zone). In such a situation, a photo-initiator depleted zone would be built-up and drawn along the writing laser spot just as argued before, leading to a sign-switched line-start effect by the same arguments. Obviously, as the oxygen-quenching also occurs at these velocities, a larger oxygen-free region will surround the inner initiator-depletion zone in this case. This initiator-diffusion dominated behavior might also go along with the formation of thicker lines due to radical diffusion (in combination with long polymerization durations in such a situation), which can indeed be observed at very low writing velocities (**Figure 7.3 b**, uppermost lines). However, the fact that the absolute writing threshold power increases compared to faster velocities as soon as this effect sets in cannot be explained by this hypothesis and hence, an the interplay of the different diffusion and reaction mechanisms seems to be even more complex in this case.

From a practical point-of-view, it should be noted that this is a very extreme case of proximity effects, and that such effects can be largely reduced by targeting high writing velocities or short exposure periods and by a proper choice of the photo-initiator species. E.g., from the investigated set, DETC and ITX seem to show no or only little proximity effects and should hence be preferred for any “slow writing” applications.

### 7.3 Sample Temperature

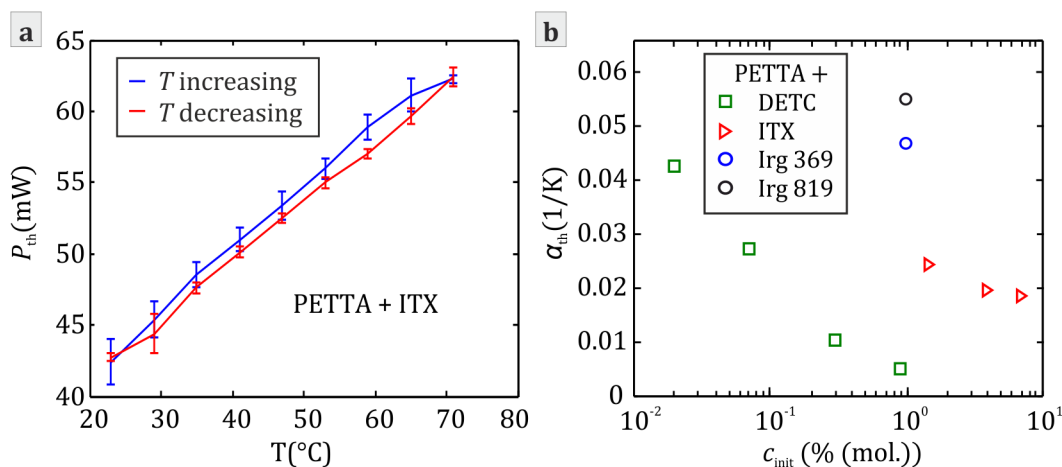
As it has been discussed in Section 5.2, even though local sample heating might in principle influence the DLW process, this effect was not found to occur in actual experiments. However, one may still look at the influence of the overall sample temperature when the photo-resist is heated by an external heat source. Historically, these experiments were intended to yield a better “feeling” with respect to the sensitivity of the DLW process to temperature before the experiments from Section 5.2 were performed. Even though from the experiments there, it is quite clear that thermal effects play no or only a minor role for DLW, one may still take the results of the experiments presented in this section in order to test the understanding of the overall process.

The experiments have been performed at the MaiTai-Setup in a similar configuration to the temperature calibration curve for the local temperature measurement (Section 4.1). In order to minimize the thermal gradients within the sample through heat conduction, the oil-immersion objective lens was replaced by an air-objective lens (63x, NA = 0.75, working distance 1.7 mm) in order to avoid heat conduction through the immersion medium. Therefore, the resulting focus is larger than for the standard configuration, so that also the required writing laser power is increased. However, we expect at least qualitatively a good agreement with respect to the relative change of the writing threshold as a function of the sample temperature.

In order to measure the writing threshold, we write dashed lines with varying power in a similar way to the previous experiments (e.g., Section 7.2). This test was repeated several times at different sample temperatures, with the sample temperature being set using an active control loop based on a resistance temperature detector. Typically, it takes several minutes until a set point is reached with deviations of less than approximately 0.5 K. Hence, the overall process of heating the sample to the maximum temperature (80° C) and cooling it down again takes several hours. Please note that the photo-resist is in direct contact with the temperature-controlled metal block so that it is almost completely sealed from the external atmosphere. Another experimental hurdle is the fact that the sample heating induced a shift of the sample in axial direction of approximately 30  $\mu\text{m}$  when going from room temperature to the maximum. In order to compensate for this shift, a piezoelectric stage with sufficient traveling distance in axial direction was used.

A typical measurement is depicted in **Figure 7.4 a**). The measurement was repeated several times in order to get a measure for the typical statistical errors. For all cases, it is found that the polymerization threshold is increased with increasing temperature by typically a few percent per Kelvin. The slope of linear fits for similar measurements to **Figure 7.4 a**), but for different photo-resists is displayed in **Figure 7.4 b** as a function of the photo-initiator concentration. As an example, a typical relative change of  $\alpha_{\text{th}} = 0.02$  corresponds to an increase of the writing threshold by two percent if the sample temperature is increased by one Kelvin. Once again, the concentration is varied for DETC and ITX, with for both the same general trend that the temperature dependence is most pronounced for low photo-initiator concentrations.

At first glance, this trend seems quite surprising. From the polymer chemistry side, one would expect to see an increase in the polymerization velocity for higher temperatures due to the higher mobility of the reagents [126], leading to



**Figure 7.4:** **a)** Temperature dependence of the polymerization threshold power for one selected (and typical) photo-resist composition. The error bars indicate the standard deviation over ten individual measurements. Lines are written with a velocity of  $100 \mu\text{m/s}$ . **b)** Relative shift of the writing threshold per Kelvin for similar measurements to for different photo-resists from a linear fit ( $P_{th}(T) = \alpha_{th} P_{th}(23^\circ K)$ ). For DETC and ITX, different concentrations were investigated as indicated.

a reduced threshold. However, this increase in mobility would affect not only the chain-growth mechanism, but also the quenching reaction (oxygen) in a similar way, so that at first order, the overall effect could be expected to cancel out.

However, with the experimental results of the previous chapter in mind, it is relatively clear that the reaction pathway cannot be explained satisfactorily without including oxygen diffusion into the discussion. Therefore, even if the changes of the diffusion-dominated reaction rates of propagation and oxygen quenching cancel each other, the rate of oxygen diffusion will increase with the decrease in viscosity at higher temperatures. Obviously, this will lead to an increase in the writing threshold.

By this explanation, we can also explain the general concentration dependence of the temperature effect and the relative differences for the different initiators at least qualitatively. Namely, as argued in Section 7.1, the resulting writing threshold is always the result of an interplay of the relative concentrations of photo-initiator and oxygen and it also depends on the specific quenching efficiency for a certain initiator species. Loosely speaking, at low initiator concentrations and for the Irgacure initiators, the overall influence of oxygen is



larger due to initiator saturation effects as discussed in the previous sections and hence, also the thermal effect can be expected to be more pronounced. We also find some kind of hysteresis behavior, i.e., the writing threshold is lower when the sample has been at higher temperatures before (e.g., **Figure 7.4 a**). This effect can be observed for all photo-resist, although with different magnitudes. A systematic error due to a delayed heating of the sample as compared to the temperature probe seems unlikely (given the waiting times of several minutes) and would point into the other direction: Temperatures would still be higher than the measured value for the cooling branch, leading to an increased threshold. One effect that could possibly explain the behavior is the change in oxygen solubility in the monomer with temperature. If at high temperatures, less oxygen could be dissolved in the monomer, this would lead to a decreased writing threshold. As the sample is almost completely sealed, the settling of the equilibrium concentration with the air atmosphere will require some time. Hence, the reduced oxygen concentration would lack behind the actual temperature curve, leading to a reduced writing threshold during cool-down. Indeed, a reduced oxygen solubility has been reported for a diacrylate monomer (tripropylene glycol diacrylate) [127], which is consistent with the observed behavior. Notably, this effect would be counteracting the increased oxygen diffusivity discussed before, which still seems to dominate the overall behavior (i.e., an increase of the writing threshold with temperature).

Even though all of the explanations given in this last chapter are very qualitative, they at least point into the right directions. As oxygen can be responsible for threshold shifts of some orders of magnitude (Section 6.1.1), also the overall magnitude of the observed effects seems consistent with the given arguments. All in all, we find that oxygen quenching and oxygen diffusion can indeed explain the dependence of the writing threshold laser power on a wide variety of experimental parameters such as the photo-initiator concentration, the writing velocity and the sample temperature, even though, at first glance, a direct relation of these parameters with oxygen is not evident. It is therefore considered very likely that similar explanations can be found for many other experimental situations.



# 8

## Chapter 8

---

# Conclusions

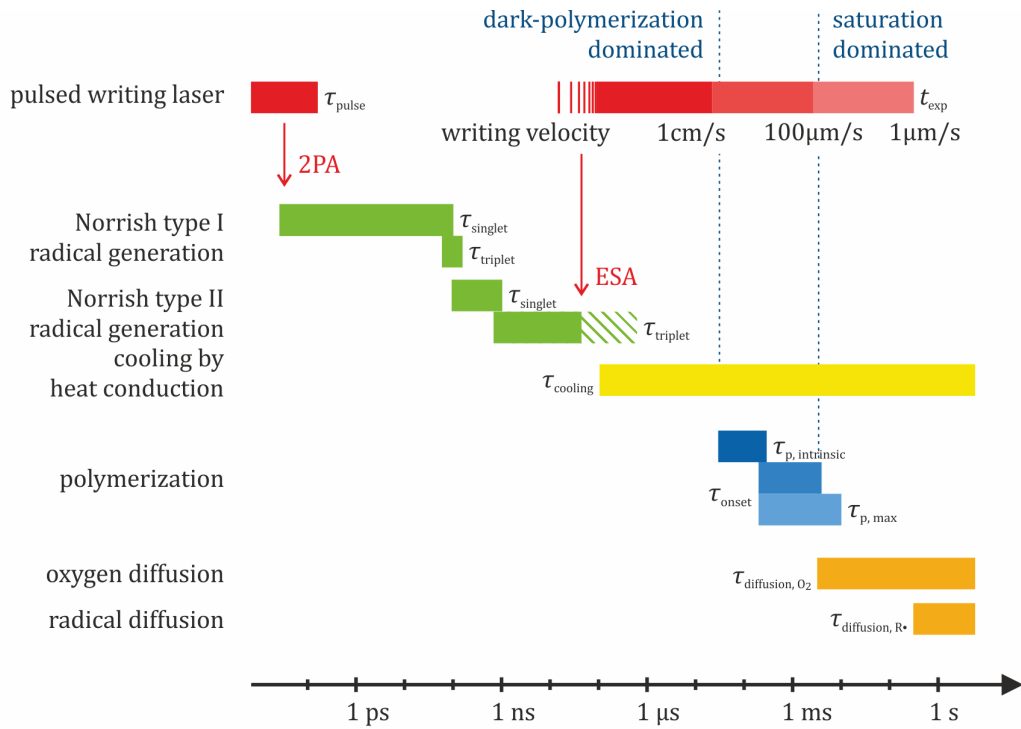
In this thesis, the state-of-the-art knowledge on the microscopic mechanisms of direct laser writing (DLW) by multi-photon polymerization as well as the performed underlying experiments were presented. The results will be resumed very briefly within this chapter. In order to conclude, examples are given for situations where the acquired knowledge concerning the DLW mechanisms may be of use for applications.

Due to the small reaction volume and the high exposure intensity, the reaction conditions are very specific in the case of DLW as compared to other applications in the broader fields of laser materials processing and photo-polymerization. Within this thesis, a focus is therefore set on experiments that show how the common photo-physical and photo-chemical reaction models from these other fields must be adapted. These include the experimental discrimination of the excitation mechanism through variation of the laser repetition rate, the measurement of the local heating during the writing process based on luminescent nanoparticles, the investigation of the influence of oxygen quenching and oxygen diffusion, and the experimental determination of the duration of the polymerization reaction.

In order to resume the results of these experiments, the overall reaction pathway of the photo-polymerization will be recapitulated following the time-line which is given by the lifetimes of the involved intermediate states and the typical timescales for the single reaction steps (**Figure 8.1**). When using a high-repetition-rate laser system, each voxel is exposed by many laser pulses ( $10^4 - 10^7$ ) in all cases of practical relevance.<sup>1</sup> The photo-initiator is excited

---

<sup>1</sup> All technical parameters within this chapter refer to the reference scheme for DLW, which is the basis for all experiments within this thesis (Section 2).



**Figure 8.1:** Schematic representation of the discussed process mechanisms on a logarithmic time scale for the reference DLW scheme. The exposure by the writing laser as well as typical lifetimes of intermediate states and typical timescales for the polymerization reaction, molecular diffusion and conductive cooling are indicated. The colored bars indicate the time period in which the corresponding process is expected to occur. The differently shaded bars for the exposure time and the polymerization duration correspond to different writing velocities and exposure times as indicated.

---

by a train of 100 fs-pulses with a typical exposure period of 0.2 ms – 200 ms, corresponding to writing velocities of 1 cm/s – 1  $\mu\text{m/s}$ . As the fundamental wavelength of the writing laser is not absorbed by the photo-initiator, multi-photon absorption is dominant as an initial excitation step. The nonlinearity of this absorption process was measured under different conditions by varying the laser repetition rate (Section 5.1), which allows distinguishing the different initiation pathways which are outlined in the following.

In the “classical” case of two-photon absorption, excitation to the first excited singlet state of the photo-initiator ( $S_0 - S_1$ ) is followed by inter-system crossing to the triplet state ( $S_1 - T_1$ ). In the case of commercial Norrish type I photo-initiators, starting radicals may be formed directly from this triplet state by  $\alpha$ -scission. Typically, the lifetimes of the excited states are very short in this case ( $\tau_{\text{singlet}} \approx \tau_{\text{triplet}} \approx 0.1$  ns [66], Irgacure 819 in acetonitrile). For Norrish type II photo-initiators, in particular the lifetime of the triplet state is substantially longer ( $\tau_{\text{singlet}} \approx 1$  ns [18] and  $\tau_{\text{triplet}} \approx 2.3$   $\mu\text{s}$  [20], DETC in PETA), as photo-dissociation and radical substantially cannot occur directly from the triplet. Moreover, the triplet lifetime is longer than the period between two pulses (12.5 ns), so that the effective lifetime is largely reduced due to excited state absorption of subsequent writing laser pulses ( $\tau_{\text{triplet, effective}} \lesssim 100$  ns [19], DETC in PETA), and radicals are generated in an effective three-photon absorption process (Section 5.1). In principle, this nonlinearity could also originate from a direct (i.e., quantum-mechanically resonant) three-photon excitation. However, we found two-photon scaling behavior for both, the excitation of the DETC luminescence under the very same experimental conditions as for DLW, and for photo-polymerization with DETC in cases when an additional co-initiator is added (Section 5.3). These findings strongly hint that two-photon excitation is the initial excitation step for all investigated photo-initiators, and that radicals are generated by excited state absorption in the case of Norrish type II photo-initiators if no co-initiator is present.

If no photo-initiator is added or at low repetition rates, the polymerization may also be triggered by a multi-photon ionization pathway. I.e., radicals are generated by the direct excitation of the monomer (or, if present, the photo-initiator) to an unbound electronic state (Section 5.1). Eventually, this step may be followed by plasma formation due to the large absorptivity of the charged intermediate states. This process also seems to be the trigger micro-explosions, which occur as a thermal overexposure effect. In literature, plasma lifetimes of a few nanoseconds have been reported in liquids, albeit under very different conditions ( $\lambda = 1064$  nm,  $d_{\text{voxel}} = 11$   $\mu\text{m}$ , in water) [128]. However, the intermediate state lifetimes of the photo-dissociated molecules

after the end of the exposure are unclear. For DLW, the experiments indicate some kind of “intermediate state lifetime” of around 100 ns, which is consistent with conductive cooling (Section 5.1): Heat conduction is expected to lead to cooling of the focal volume in between two laser pulses if the pulse separation exceeds  $\tau_c \approx 100$  ns, resulting in an increased (thermal) damage threshold (Section 3.3). Yet, for the polymerization reaction itself, we did not find any indication that thermal effects play a role independent from the writing laser repetition rate, and also for Norrish type II photo-initiators such as DETC (Section 5.2).<sup>2</sup>

The actual polymerization reaction takes place on a 100  $\mu\text{s}$ –10 ms timescale, depending on the exposure period and the writing laser power (Section 6.2). After this period, the polymerization reaction is terminated by oxygen diffusion (Section 6.1). Large writing velocities above 100  $\mu\text{m/s}$  are therefore required for the polymerization to primarily occur after the end of the exposure (Section 6.2). In this case, the polymerization does not coincide temporarily with the initiation process, and the polymerization threshold can indeed be described by a relatively simple analytical model (Section 3.3). These conditions are ideal for any experiment that aims at a qualitative or quantitative investigation of the radical formation mechanism. For lower writing velocities, oxygen diffusion comes into play (Section 6.1). In these cases, the overall behavior is dominated by photo-initiator depletion effects, i.e., the overall reaction only yields polymer structures if the exposure intensity (and hence, the radical generation rate) is large enough to overcome oxygen diffusion. At low intensities, this is not the case, so that the photo-initiator is consumed without polymer formation, yielding similar behavior to the Schwarzschild effect in photography. Furthermore, unexpected (and hence, mostly undesired) effects such as line-start effects or self-depletion of the polymerization may occur in this regime (Section 7).

Apart from the academic interest, the presented results may help users of the DLW technique and, maybe more importantly, its future developers. Hence, a few examples will be given in the following that show in which contexts the obtained results may be of interest. For example, it is shown that Norrish type II photo-initiators generate radicals in an effective three-photon process. Therefore, the corresponding photo-resists are not UV-sensitive, and hence, no yellow-light environment is required for their processing. Or, as a different example, the above-mentioned diffusion mechanisms which are related to “slow

---

<sup>2</sup> For DETC, the precision of the temperature detection ( $\pm 50$  K) unfortunately is not yet satisfactory to definitely exclude thermal processes.

---

writing” ( $v < 100 \mu\text{m/s}$ ) are clearly undesired. These “feedback” effects can be avoided in the post-polymerization regime, i.e., for writing velocities exceeding  $100 \mu\text{m/s}$ . This finding is a highly positive one, as for many applications of DLW, a short overall fabrication time is an important demand. In this context, the observed high nonlinearity of the absorption process (e.g.,  $N = 3$  for type II photo-initiators,  $N = 5 - 7$  at low repetition rates or without photo-initiator) is also considered highly favorable, as it leads to a beneficial scaling of the required writing laser intensity with the writing velocity. For the currently used laser systems for DLW, the writing speed is ultimately limited to the situation where each voxel is exposed by one single pulse, i.e.,  $v = d_{\text{voxel}} \cdot R = 16 \text{ m/s}$  for a repetition rate of 80 MHz. According to Equation (3.5), it is expected that the writing threshold is increased by roughly a factor of  $\sqrt[3]{\frac{16 \text{ m/s}}{100 \mu\text{m/s}}} \approx 110$  for  $N = 3$  as compared to typical values of a few milliwatts at  $100 \mu\text{m/s}$ , which is within the range of typical commercial laser systems. Hence, a tremendous increase in the writing speed in principle is possible on the basis of available technologies, with the main bottleneck so far being the precision of the scanning method and also the data generation and transfer.

In the introductory chapter of this thesis, it was stated that DLW is a “Teravoxel technology” in the sense that structures containing up to  $10^{12}$  voxels may be fabricated using state-of-the-art commercial DLW systems. In the past, many researchers believed that the writing velocity in DLW would be ultimately limited by the availability of high-power laser sources due to the underlying two-photon absorption process. In contrast, as argued (and backed by the results of this thesis), single pulse polymerization is within reach even with high repetition rate writing lasers, yielding a maximum writing velocity of 80 Megavoxels per second for the reference DLW scheme. As a comparison, a technology named “Continuous liquid interface production” (*Carbon3D*) was very recently featured in the magazine *Science* as a new and extremely rapid 3D-printing technology [129]. Here, structure dimensions of 10 Megavoxels are shown, fabricated at velocities in the regime of Kilovoxels per second,<sup>3</sup> which both is less by roughly five orders of magnitude than the limit for DLW. Even though the absolute printing velocity (measured e.g. by the printed volume per time) in this case largely exceeds that of DLW, this example certainly illustrates the enormous potential of DLW, not only as a toy for scientists, but also as a production technology for “real world applications”.

---

<sup>3</sup> Printing volume: roughly  $10 \text{ cm} \times 10 \text{ cm} \times 10 \text{ cm}$  printed within one hour with a minimal feature size of approximately  $500 \mu\text{m}$ .





# Bibliography

- [1] S. Maruo, O. Nakamura, and S. Kawata, *Three-dimensional microfabrication with two-photon-absorbed photopolymerization*, Opt. Lett. **22** (2), 132 (1997).
- [2] S. Kawata, H.-B. Sun, T. Tanaka, and K. Takada, *Finer features for functional microdevices*, Nature **412** (6848), 697 (August 2001).
- [3] C. N. LaFratta, J. T. Fourkas, T. Baldacchini, and R. A. Farrer, *Multiphoton Fabrication*, Angew. Chem. Int. Ed. **46** (33), 6238 (2007).
- [4] K.-S. Lee, R. H. Kim, D.-Y. Yang, and S. H. Park, *Advances in 3D nano/microfabrication using two-photon initiated polymerization*, Prog. Polym. Sci. **33** (6), 631 (2008).
- [5] S. Maruo and J. Fourkas, *Recent progress in multiphoton microfabrication*, Laser Photon. Rev. **2** (1-2), 100 (2008).
- [6] G. von Freymann, A. Ledermann, M. Thiel, I. Staude, S. Essig, K. Busch, and M. Wegener, *Three-Dimensional Nanostructures for Photonics*, Adv. Funct. Mater. **20** (7), 1038 (2010).
- [7] M. Kadic, T. Bückmann, R. Schittny, and M. Wegener, *Metamaterials beyond electromagnetism*, Rep. Prog. Phys. **76** (12), 126501 (2013).
- [8] M. Malinauskas, M. Farsari, A. Piskarskas, and S. Juodkazis, *Ultrafast laser nanostructuring of photopolymers: A decade of advances*, Phys. Rep. **533** (1), 1 (2013).
- [9] X. Zhou, Y. Hou, and J. Lin, *A review on the processing accuracy of two-photon polymerization*, AIP Adv. **5** (3) (2015).
- [10] T. Bückmann, M. Thiel, M. Kadic, R. Schittny, and M. Wegener, *An elasto-mechanical unfeelability cloak made of pentamode metamaterials*, Nat. Commun. **5** (2014).

- [11] J. Fischer and M. Wegener, *Three-dimensional optical laser lithography beyond the diffraction limit*, Laser Photonic Rev. **7** (1), 22 (2013).
- [12] T. A. Klar, R. Wollhofen, and J. Jacak, *Sub-Abbe resolution: from STED microscopy to STED lithography*, Phys. Scr. **2014** (T162), 014049 (2014).
- [13] S. W. Hell and M. Kroug, *Ground-state-depletion fluorescence microscopy: A concept for breaking the diffraction resolution limit*, Appl. Phys. B **60** (5), 495 (1995).
- [14] T. A. Klar and S. W. Hell, *Subdiffraction resolution in far-field fluorescence microscopy*, Opt. Lett. **24** (14), 954 (1999).
- [15] J. Fischer, *Three-dimensional optical lithography beyond the diffraction limit*, Dissertation, Karlsruhe Institute of Technology (KIT) (2012).
- [16] J. Fischer, J. B. Mueller, J. Kaschke, T. J. A. Wolf, A.-N. Unterreiner, and M. Wegener, *Three-dimensional multi-photon direct laser writing with variable repetition rate*, Opt. Express **21** (22), 26244 (2013).
- [17] J. Fischer and M. Wegener, *Three-dimensional direct laser writing inspired by stimulated-emission-depletion microscopy [Invited]*, Opt. Mater. Express **1** (4), 614 (2011).
- [18] J. Fischer and M. Wegener, *Ultrafast Polymerization Inhibition by Stimulated Emission Depletion for Three-dimensional Nanolithography*, Adv. Mater. **24** (10), OP65 (2012).
- [19] B. Harke, P. Bianchini, F. Brandi, and A. Diaspro, *Photopolymerization Inhibition Dynamics for Sub-Diffraction Direct Laser Writing Lithography*, ChemPhysChem **13** (6), 1429 (2012).
- [20] B. Harke, W. Dallari, G. Grancini, D. Fazzi, F. Brandi, A. Petrozza, and A. Diaspro, *Polymerization Inhibition by Triplet State Absorption for Nanoscale Lithography*, Adv. Mater. **25** (6), 904 (2013).
- [21] R. Wollhofen, J. Katzmann, C. Hrelescu, J. Jacak, and T. A. Klar, *120 nm resolution and 55 nm structure size in STED-lithography*, Opt. Express **21** (9), 10831 (2013).
- [22] T. J. A. Wolf, J. Fischer, M. Wegener, and A.-N. Unterreiner, *Pump-probe spectroscopy on photoinitiators for stimulated-emission-depletion optical lithography*, Opt. Lett. **36** (16), 3188 (2011).

- 
- [23] J. Fischer, J. B. Mueller, A. S. Quick, J. Kaschke, C. Barner-Kowollik, and M. Wegener, *Exploring the Mechanisms in STED-Enhanced Direct Laser Writing*, *Adv. Opt. Mater.* (2014).
- [24] J. Serbin, A. Egbert, A. Ostendorf, B. N. Chichkov, R. Houbertz, G. Domann, J. Schulz, C. Cronauer, L. Fröhlich, and M. Popall, *Femtosecond laser-induced two-photon polymerization of inorganic organic hybrid materials for applications in photonics*, *Opt. Lett.* **28** (5), 301 (Mar 2003).
- [25] A. Ovsianikov, J. Viertl, B. Chichkov, M. Oubaha, B. MacCraith, I. Sakellari, A. Giakoumaki, D. Gray, M. Vamvakaki, M. Farsari, and C. Fotakis, *Ultra-Low Shrinkage Hybrid Photosensitive Material for Two-Photon Polymerization Microfabrication*, *ACS Nano* **2** (11), 2257 (2008).
- [26] A. S. Quick, J. Fischer, B. Richter, T. Pauloehrl, V. Trouillet, M. Wegener, and C. Barner-Kowollik, *Preparation of Reactive Three-Dimensional Microstructures via Direct Laser Writing and Thiol-ene Chemistry*, *Macromol. Rapid Commun.* **34** (4), 335 (2013).
- [27] C. A. Coenjarts and C. K. Ober, *Two-Photon Three-Dimensional Microfabrication of Poly(Dimethylsiloxane) Elastomers*, *Chem. Mater.* **16** (26), 5556 (2004).
- [28] M. Deubel, G. von Freymann, M. Wegener, S. Pereira, K. Busch, and C. M. Soukoulis, *Direct laser writing of three-dimensional photonic-crystal templates for telecommunications*, *Nat. Mater.* **3** (7), 444 (2004).
- [29] J. K. Gansel, M. Thiel, M. S. Rill, M. Decker, K. Bade, V. Saile, G. von Freymann, S. Linden, and M. Wegener, *Gold Helix Photonic Metamaterial as Broadband Circular Polarizer*, *Science* **325** (5947), 1513 (September 2009).
- [30] T. Tanaka, A. Ishikawa, and S. Kawata, *Two-photon-induced reduction of metal ions for fabricating three-dimensional electrically conductive metallic microstructure*, *Appl. Phys. Lett.* **88** (8), (2006).
- [31] M. Malinauskas, A. Žukauskas, G. Bičkauskaitė, R. Gadonas, and S. Juodkazis, *Mechanisms of three-dimensional structuring of photo-polymers by tightly focussed femtosecond laser pulses*, *Opt. Express* **18** (10), 10209 (2010).

- [32] M. Malinauskas, P. Danilevicius, and S. Juodkazis, *Three-dimensional micro-/nano-structuring via direct write polymerization with picosecond laser pulses*, Opt. Express **19** (6), 5602 (2011).
- [33] M. Emons, K. Obata, T. Binhammer, A. Ovsianikov, B. N. Chichkov, and U. Morgner, *Two-photon polymerization technique with sub-50 nm resolution by sub-10 fs laser pulses*, Opt. Mater. Express **2** (7), 942 (Jul 2012).
- [34] L. Nguyen, M. Straub, and M. Gu, *Acrylate-Based Photopolymer for Two-Photon Microfabrication and Photonic Applications*, Adv. Funct. Mater. **15** (2), 209 (2005).
- [35] N. Pucher, A. Rosspeintner, V. Satzinger, V. Schmidt, G. Gescheidt, J. Stampfl, and R. Liska, *Structure-Activity Relationship in D- $\pi$ -A- $\pi$ -D-Based Photoinitiators for the Two-Photon-Induced Photopolymerization Process*, Macromolecules **42** (17), 6519 (2009).
- [36] M. Straub and M. Gu, *Near-infrared photonic crystals with higher-order bandgaps generated by two-photon photopolymerization*, Opt. Lett. **27** (20), 1824 (October 2002).
- [37] I. Wang, M. Bouriau, P. L. Baldeck, C. Martineau, and C. Andraud, *Three-dimensional microfabrication by two-photon-initiated polymerization with a low-cost microlaser*, Opt. Lett. **27** (15), 1348 (2002).
- [38] W. Haske, V. W. Chen, J. M. Hales, W. Dong, S. Barlow, S. R. Marder, and J. W. Perry, *65 nm feature sizes using visible wavelength 3-D multiphoton lithography*, Opt. Express **15** (6), 3426 (2007).
- [39] M. Thiel, J. Fischer, G. v. Freymann, and M. Wegener, *Direct laser writing of three-dimensional submicron structures using a continuous-wave laser at 532 nm*, Appl. Phys. Lett. **97** (22), 221102 (2010).
- [40] E. T. Ritschdorff and J. B. Shear, *Multiphoton Lithography Using a High-Repetition Rate Microchip Laser*, Anal. Chem. **82** (20), 8733 (2010).
- [41] A. Ovsianikov, A. Deiwick, S. Van Vlierberghe, M. Pflaum, M. Wilhelmi, P. Dubruel, and B. Chichkov, *Laser Fabrication of 3D Gelatin Scaffolds for the Generation of Bioartificial Tissues*, Materials **4** (1), 288 (2011).

- 
- [42] C. De Marco, A. Gaidukeviciute, R. Kiyan, S. M. Eaton, M. Levi, R. Osellame, B. N. Chichkov, and S. Turri, *A New Perfluoropolyether-Based Hydrophobic and Chemically Resistant Photoresist Structured by Two-Photon Polymerization*, *Langmuir* **29** (1), 426 (2013).
- [43] S. Maruo and K. Ikuta, *Three-dimensional microfabrication by use of single-photon-absorbed polymerization*, *Appl. Phys. Lett.* **76** (19), 2656 (2000).
- [44] E. Abbe, *Beiträge zur Theorie des Mikroskops und der mikroskopischen Wahrnehmung*, *Archiv f. mikrosk. Anatomie* **9** (1), 413 (1873).
- [45] C. M. Sparrow, *On spectroscopic resolving power*, *Astro. J.* **44**, 76 (1916).
- [46] S. W. Hell and J. Wichmann, *Breaking the diffraction resolution limit by stimulated emission: stimulated-emission-depletion fluorescence microscopy*, *Opt. Lett.* **19** (11), 780 (1994).
- [47] E. Betzig, *Proposed method for molecular optical imaging*, *Optics letters* **20** (3), 237 (1995).
- [48] R. M. Dickson, A. B. Cubitt, R. Y. Tsien, and W. Moerner, *On/off blinking and switching behaviour of single molecules of green fluorescent protein*, *Nature* **388** (6640), 355 (1997).
- [49] E. Rittweger, K. Y. Han, S. E. Irvine, C. Eggeling, and S. W. Hell, *STED microscopy reveals crystal colour centres with nanometric resolution*, *Nat. Photon.* **3** (3), 144 (2009).
- [50] T. F. Scott, B. A. Kowalski, A. C. Sullivan, C. N. Bowman, and R. R. McLeod, *Two-Color Single-Photon Photoinitiation and Photoinhibition for Subdiffraction Photolithography*, *Science* **324** (5929), 913 (2009).
- [51] L. Li, R. R. Gattass, E. Gershgoren, H. Hwang, and J. T. Fourkas, *Achieving Lambda/20 Resolution by One-Color Initiation and Deactivation of Polymerization*, *Science* **324** (5929), 910 (2009).
- [52] Z. Gan, Y. Cao, R. A. Evans, and M. Gu, *Three-dimensional deep sub-diffraction optical beam lithography with 9 nm feature size*, *Nat. Commun.* **4** (2013).

- [53] J. Fischer, G. von Freymann, and M. Wegener, *The Materials Challenge in Diffraction-Unlimited Direct-Laser-Writing Optical Lithography*, Adv. Mater. **22** (32), 3578 (2010).
- [54] J. Fischer, T. Ergin, and M. Wegener, *Three-dimensional polarization-independent visible-frequency carpet invisibility cloak*, Opt. Lett. **36** (11), 2059 (Jun 2011).
- [55] T. F. Scott, C. J. Kloxin, D. L. Forman, R. R. McLeod, and C. N. Bowman, *Principles of voxel refinement in optical direct write lithography*, J. Mater. Chem. **21** (37), 14150 (2011).
- [56] Y. Cao, Z. Gan, B. Jia, R. A. Evans, and M. Gu, *High-photosensitive resin for super-resolution direct-laser-writing based on photoinhibited polymerization*, Opt. Express **19** (20), 19486 (2011).
- [57] D. L. Forman, M. C. Cole, and R. R. McLeod, *Radical diffusion limits to photoinhibited superresolution lithography*, Phys. Chem. Chem. Phys. **15** (36), 14862 (2013).
- [58] X. Allonas, J. Lalevee, F. Morlet-Savary, and J. P. Fouassier, *Understanding the reactivity of photoinitiating systems for photopolymerization*, Polimery **51** (7-8), 491 (2006).
- [59] M. Göppert-Mayer, *Über Elementarakte mit zwei Quantensprüngen*, Ann. Phys. **401** (3), 273 (1931).
- [60] K. J. Schafer, J. M. Hales, M. Balu, K. D. Belfield, E. W. Van Stryland, and D. J. Hagan, *Two-photon absorption cross-sections of common photoinitiators*, J. Photochem. Photobiol. A **162** (2-3), 497 (2004).
- [61] B. C. Stuart, M. D. Feit, S. Herman, A. M. Rubenchik, B. W. Shore, and M. D. Perry, *Nanosecond-to-femtosecond laser-induced breakdown in dielectrics*, Phys. Rev. B **53** (4), 1749 (1996).
- [62] S. M. Hankin, D. M. Villeneuve, P. B. Corkum, and D. M. Rayner, *Nonlinear Ionization of Organic Molecules in High Intensity Laser Fields*, Phys. Rev. Lett. **84** (22), 5082 (2000).
- [63] F. A. Ilkov, J. E. Decker, and S. L. Chin, *Ionization of atoms in the tunnelling regime with experimental evidence using Hg atoms*, J. Phys. B: At., Mol. Opt. Phys. **25** (19), 4005 (1992).

- 
- [64] L. Keldysh, *Diagram technique for nonequilibrium processes*, Sov. Phys. JETP **20** (4), 1018 (1965).
- [65] P. Lambropoulos, *Mechanisms for Multiple Ionization of Atoms by Strong Pulsed Lasers*, Phys. Rev. Lett. **55** (20), 2141 (1985).
- [66] S. Jockusch, I. V. Koptug, P. F. McGarry, G. W. Sluggett, N. J. Turro, and D. M. Watkins, *A Steady-State and Picosecond Pump-Probe Investigation of the Photophysics of an Acyl and a Bis(acyl)phosphine Oxide*, J. Am. Chem. Soc. **119** (47), 11495 (1997).
- [67] C. S. Colley, D. C. Grills, N. A. Besley, S. Jockusch, P. Matousek, A. W. Parker, M. Towrie, N. J. Turro, P. M. W. Gill, and M. W. George, *Probing the Reactivity of Photoinitiators for Free Radical Polymerization: Time-Resolved Infrared Spectroscopic Study of Benzoyl Radicals*, J. Am. Chem. Soc. **124** (50), 14952 (2002).
- [68] E. Andrzejewska, *Photopolymerization kinetics of multifunctional monomers*, Prog. Polym. Sci. **26** (4), 605 (2001).
- [69] B. Tieke, *Makromolekulare Chemie : eine Einführung* (WILEY-VCH, Weinheim, 2005), second edition.
- [70] C. Decker and A. D. Jenkins, *Kinetic approach of oxygen inhibition in ultraviolet- and laser-induced polymerizations*, Macromolecules **18** (6), 1241 (1985).
- [71] A. K. O'Brien, N. B. Cramer, and C. N. Bowman, *Oxygen inhibition in thiol-acrylate photopolymerizations*, J. Polym. Sci. A **44** (6), 2007 (2006).
- [72] C. Decker and K. Moussa, *Real-time kinetic study of laser-induced polymerization*, Macromolecules **22** (12), 4455 (1989).
- [73] K. S. Anseth and C. N. Bowman, *Reaction Diffusion Enhanced Termination in Polymerizations of Multifunctional Monomers*, Polym. React. Eng. **1** (4), 499 (1993).
- [74] K. S. Anseth, C. N. Bowman, and N. A. Peppas, *Polymerization kinetics and volume relaxation behavior of photopolymerized multifunctional monomers producing highly crosslinked networks*, J. Polym. Sci. A **32** (1), 139 (1994).

- [75] J. Gao and A. Penlidis, *A Comprehensive Simulator/Database Package for Reviewing Free-Radical Homopolymerizations*, J. Macromol. Sci. C **36** (2), 199 (1996).
- [76] M. D. Goodner and C. N. Bowman, *Development of a comprehensive free radical photopolymerization model incorporating heat and mass transfer effects in thick films*, Chem. Eng. Sci. **57** (5), 887 (2002).
- [77] C. Decker, *Kinetic Study and New Applications of UV Radiation Curing*, Macromol. Rapid Commun. **23** (18), 1067 (2002).
- [78] J.-F. Xing, X.-Z. Dong, W.-Q. Chen, X.-M. Duan, N. Takeyasu, T. Tanaka, and S. Kawata, *Improving spatial resolution of two-photon microfabrication by using photoinitiator with high initiating efficiency*, Appl. Phys. Lett. **90** (13), 131106 (2007).
- [79] G. R. Tryson and A. R. Shultz, *A calorimetric study of acrylate photopolymerization*, J. Polym. Sci. Polym. Phys. Ed. **17** (12), 2059 (1979).
- [80] F. R. Wight, *Oxygen inhibition of acrylic photopolymerization*, J. Polym. Sci. B Polym. Lett. Ed. **16** (3), 121 (1978).
- [81] A. K. O'Brien and C. N. Bowman, *Impact of Oxygen on Photopolymerization Kinetics and Polymer Structure*, Macromolecules **39** (7), 2501 (2006).
- [82] S. C. Ligon, B. Husár, H. Wutzel, R. Holman, and R. Liska, *Strategies to Reduce Oxygen Inhibition in Photoinduced Polymerization*, Chem. Rev. **114** (1), 557 (2013).
- [83] A. Pikulin and N. Bityurin, *Spatial resolution in polymerization of sample features at nanoscale*, Phys. Rev. B **75** (19), 195430 (2007).
- [84] M. Campbell, D. N. Sharp, M. T. Harrison, R. G. Denning, and A. J. Turberfield, *Fabrication of photonic crystals for the visible spectrum by holographic lithography*, Nature **404** (6773), 53 (2000).
- [85] D. C. Meisel, M. Wegener, and K. Busch, *Three-dimensional photonic crystals by holographic lithography using the umbrella configuration: Symmetries and complete photonic band gaps*, Phys. Rev. B **70** (16), 165104 (2004).



- [86] A. van de Nes, L. Billy, S. Pereira, and J. Braat, *Calculation of the vectorial field distribution in a stratified focal region of a high numerical aperture imaging system*, Opt. Express **12** (7), 1281 (2004).
- [87] P. Mueller, M. Thiel, and M. Wegener, *3D direct laser writing using a 405nm diode laser*, Opt. Lett. **39** (24), 6847 (2014).
- [88] T. Baldacchini and R. Zadoyan, *In situ and real time monitoring of two-photon polymerization using broadband coherent anti-Stokes Raman scattering microscopy*, Opt. Express **18** (18), 19219 (2010).
- [89] K. Cicha, Z. Li, K. Stadlmann, A. Ovsianikov, R. Markut-Kohl, R. Liska, and J. Stampfl, *Evaluation of 3D structures fabricated with two-photon-photopolymerization by using FTIR spectroscopy*, J. Appl. Phys. **110** (6), (2011).
- [90] F. Burmeister, S. Steenhusen, R. Houbertz, U. D. Zeitner, S. Nolte, and A. Tünnermann, *Materials and technologies for fabrication of three-dimensional microstructures with sub-100 nm feature sizes by two-photon polymerization*, J. Laser Appl. **24** (4), 042014 (2012).
- [91] L. J. Jiang, Y. S. Zhou, W. Xiong, Y. Gao, X. Huang, L. Jiang, T. Baldacchini, J.-F. Silvain, and Y. F. Lu, *Two-photon polymerization: investigation of chemical and mechanical properties of resins using Raman microspectroscopy*, Opt. Lett. **39** (10), 3034 (2014).
- [92] M. H. Bland and N. A. Peppas, *Photopolymerized multifunctional (meth)acrylates as model polymers for dental applications*, Biomaterials **17** (11), 1109 (1996).
- [93] D. W. Bäuerle, *Laser Processing and Chemistry* (Springer Science & Business Media, 2011).
- [94] J. B. Mueller, J. Fischer, Y. J. Mange, T. Nann, and M. Wegener, *In-situ local temperature measurement during three-dimensional direct laser writing*, Appl. Phys. Lett. **103** (12), 123107 (2013).
- [95] N. Uppal and P. S. Shiakolas, *Modeling of temperature-dependent diffusion and polymerization kinetics and their effects on two-photon polymerization dynamics*, J. Micro/Nanolith. MEMS MOEMS **7** (4), 043002 (2008).

- [96] T. Baldacchini, S. Snider, and R. Zadoyan, *Two-photon polymerization with variable repetition rate bursts of femtosecond laser pulses*, Opt. Express **20** (28), 29890 (2012).
- [97] H. Schäfer, P. Ptacek, K. Kämpe, and M. Haase, *Lanthanide-Doped NaYF<sub>4</sub> Nanocrystals in Aqueous Solution Displaying Strong Up-Conversion Emission*, Chem. Mater. **19** (6), 1396 (2007).
- [98] M. Nyk, R. Kumar, T. Y. Ohulchanskyy, E. J. Bergey, and P. N. Prasad, *High Contrast in Vitro and in Vivo Photoluminescence Bioimaging Using Near Infrared to Near Infrared Up-Conversion in Tm<sup>3+</sup> and Yb<sup>3+</sup> Doped Fluoride Nanophosphors*, Nano Lett. **8** (11), 3834 (2008).
- [99] S. Wu, G. Han, D. J. Milliron, S. Aloni, V. Altoe, D. V. Talapin, B. E. Cohen, and P. J. Schuck, *Non-blinking and photostable upconverted luminescence from single lanthanide-doped nanocrystals*, Proc. Natl. Acad. Sci. U.S.A. **106** (27), 10917 (2009).
- [100] F. Vetrone, R. Naccache, A. Juarranz de la Fuente, F. Sanz-Rodríguez, A. Blazquez-Castro, E. M. Rodriguez, D. Jaque, J. G. Solé, and J. A. Capobianco, *Intracellular imaging of HeLa cells by non-functionalized NaYF<sub>4</sub> : Er<sup>3+</sup>, Yb<sup>3+</sup> upconverting nanoparticles*, Nanoscale **2** (4), 495 (2010).
- [101] R. B. Liebherr, T. Soukka, O. S. Wolfbeis, and H. H. Gorris, *Maleimide activation of photon upconverting nanoparticles for bioconjugation*, Nanotechnology **23** (48), 485103 (2012).
- [102] G. Chen, H. Qiu, P. N. Prasad, and X. Chen, *Upconversion Nanoparticles: Design, Nanochemistry, and Applications in Theranostics*, Chem. Rev. **114** (10), 5161 (2014).
- [103] F. Auzel, *Upconversion and Anti-Stokes Processes with f and d Ions in Solids*, Chem. Rev. **104** (1), 139 (2004).
- [104] B. R. Judd, *Optical Absorption Intensities of Rare-Earth Ions*, Phys. Rev. **127** (3), 750 (1962).
- [105] F. Auzel, *Materials and devices using double-pumped-phosphors with energy transfer*, IEE Proceedings. **61** (6), 758 (1973).

- 
- [106] V. Tikhomirov, K. Driesen, V. Rodriguez, P. Gredin, M. Mortier, and V. Moshchalkov, *Optical nanoheater based on the Yb<sup>3+</sup>-Er<sup>3+</sup> co-doped nanoparticles*, Opt. Express **17** (14), 11794 (2009).
- [107] J. E. Roberts, *Lanthanum and Neodymium Salts of Trifluoroacetic Acid*, J. Am. Chem. Soc. **83** (5), 1087 (1961).
- [108] T. Nann and P. Mulvaney, *Single Quantum Dots in Spherical Silica Particles*, Angew. Chem. Int. Ed. **43** (40), 5393 (2004).
- [109] S. Engelhardt, *The voxel onset time as a method for the evaluation of two photon lithography*, J. Laser Micro/Nanoen. **8** (Nr.3), 230 (2013).
- [110] J. B. Mueller, J. Fischer, F. Mayer, M. Kadic, and M. Wegener, *Polymerization Kinetics in Three-Dimensional Direct Laser Writing*, Adv. Mater. **26** (38), 6566 (2014).
- [111] Y. Liu, B. Zhang, Y. Jia, and K. Xu, *Improvement of the diffraction properties in holographic polymer dispersed liquid crystal bragg gratings*, Opt. Commun. **218** (1–3), 27 (2003).
- [112] *Scifinder*, Chemical Abstracts Service: Columbus, OH, 2013; RN 58-08-2, calculated using Advanced Chemistry Development (ACD/Labs) Software V11.02 (1994-2013), accessed 07/26/2013.
- [113] J. L. R. Williams, D. P. Specht, and S. Farid, *Ketocoumarins as photosensitizers and photoinitiators*, Polymer Engineering & Science **23** (18), 1022 (1983).
- [114] J. B. Borak and D. E. Falvey, *Ketocoumarin dyes as electron mediators for visible light induced carboxylate photorelease*, Photochem. Photobiol. Sci. **9** (6), 854 (2010).
- [115] C. Decker, *Photoinitiated crosslinking polymerisation*, Prog. Polym. Sci. **21** (4), 593 (1996).
- [116] K. Schwarzschild, *On The Deviations From The Law of Reciprocity For Bromide Of Silver Gelatine*, Astroph. J. **11**, 89 (1900).
- [117] K. Takada, H.-B. Sun, and S. Kawata, *Improved spatial resolution and surface roughness in photopolymerization-based laser nanowriting*, Appl. Phys. Lett. **86** (7), 071122 (2005).

- [118] S. H. Park, T. W. Lim, D.-Y. Yang, R. H. Kim, and K.-S. Lee, *Improvement of spatial resolution in nano-stereolithography using radical quencher*, *Macromol. Res.* **14** (5), 559 (2006).
- [119] I. Sakellari, E. Kabouraki, D. Gray, V. Purlys, C. Fotakis, A. Pikulin, N. Bityurin, M. Vamvakaki, and M. Farsari, *Diffusion-Assisted High-Resolution Direct Femtosecond Laser Writing*, *ACS Nano* **6** (3), 2302 (2012).
- [120] J. J. Kurland, *Quantitative aspects of synergistic inhibition of oxygen and p-methoxyphenol in acrylic acid polymerization*, *J. Polym. Sci. A* **18** (3), 1139 (1980).
- [121] L. B. Levy, *Inhibitor-oxygen interactions in acrylic acid stabilization*, *Plant/Operations Progress* **6** (4), 188 (1987).
- [122] H. Becker and H. Vogel, *The Role of Hydroquinone Monomethyl Ether in the Stabilization of Acrylic Acid*, *Chem. Eng. Technol.* **29** (10), 1227 (2006).
- [123] L. B. Levy, *Inhibition of acrylic acid polymerization by phenothiazine and p-methoxyphenol*, *J. Polym. Sci. A* **23** (5), 1505 (1985).
- [124] S. Schulze and H. Vogel, *Aspects of the Safe Storage of Acrylic Monomers: Kinetics of the Oxygen Consumption*, *Chem. Eng. Process.* **21** (10), 829 (1998).
- [125] J. Sobek, R. Martschke, and H. Fischer, *Entropy Control of the Cross-Reaction between Carbon-Centered and Nitroxide Radicals*, *J. Am. Chem. Soc.* **123** (12), 2849, PMID: 11456972 (2001).
- [126] T. Scherzer and U. Decker, *The effect of temperature on the kinetics of diacrylate photopolymerizations studied by Real-time FTIR spectroscopy*, *Polymer* **41** (21), 7681 (2000).
- [127] T. Scherzer and H. Langguth, *Temperature Dependence of the Oxygen Solubility in Acrylates and its Effect on the Induction Period in UV Photopolymerization*, *Macromol. Chem. Phys.* **206** (2), 240 (2005).
- [128] F. Docchio, P. Regondi, M. R. C. Capon, and J. Mellerio, *Study of the temporal and spatial dynamics of plasmas induced in liquids by nanosecond Nd:YAG laser pulses. 1: Analysis of the plasma starting times*, *Appl. Opt.* **27** (17), 3661 (1988).

- [129] J. R. Tumbleston, D. Shirvanyants, N. Ermoshkin, R. Januszewicz, A. R. Johnson, D. Kelly, K. Chen, R. Pinschmidt, J. P. Rolland, A. Ermoshkin, E. T. Samulski, and J. M. DeSimone, *Continuous liquid interface production of 3D objects*, *Science* **347** (6228), 1349 (2015).



# Acknowledgments

At this point, it is my pleasure to thank all the people who contributed to this work in the one or the other way. I want to thank Prof. Dr. Martin Wegener for the great opportunity to work into his group and under his supervision. Apart from his valuable scientific advice, he always helped to keep the focus on the essentials, while still giving enough room to develop own ideas. My gratitude further goes to my second reviewer Prof. Dr. Christopher Barner-Kowollik, who contributed with his extensive knowledge on polymer chemistry.

My explicit thanks go to Dr. Joachim Fischer, who initially built the two setups used within this thesis, and who contributed to this work thorough numberless fruitful discussion and his extensive scientific knowledge. Even though he probably couldn't sleep the nights before committing the setups to me and my PhD colleague Johannes, he gave us as much support and liberty as he could. Also, I want to thank my colleagues Johannes Kaschke, Alexander Quick, Eva Blasco, and Patrick Müller with whom I shared the labs and setups. Even though lab time was mostly limited and had to be shared, we always found constructive and uncomplicated solutions, and helping each other was taken as a self-evident virtue. I especially thank Johannes Kaschke and Martin Schumann for help with the scanning electron microscope images.

I thank Johann Westhauser, Michael Hippe, Helmuth Lay, Werner Gilde, Renate Helfen, Claudia Alaya, and Ursula Möhle for their technical, computer-related and administrative support. They always did their best to backup the scientific work and keep the overhead workload for us students minimal.

For help with the proof-reading of this manuscript, I thank Dr. Joachim Fischer, Johannes Kaschke, Frederik Mayer, Patrick Müller, Alexander Quick, Dr. Andrea Scheiwe, Jana Stengler, and Andreas Wickberg.

Furthermore, my thanks go to all past and current members of the Wegener group. I enjoyed the team spirit, the scientific advice, the discussions on scientific and non-scientific topics and most of all the opportunities for spending time together on leisure activities. Last but not least I want to thank my girlfriend Jana and my family for giving me both, the support and the freedom to pursue the studies which resulted into this manuscript.





# Erklärung

Hiermit versichere ich, dass ich die vorliegende Arbeit selbstständig verfasst, noch nicht anderweitig für Prüfungszwecke vorgelegt, keine anderen als die angegebenen Quellen oder erlaubten Hilfsmittel benutzt, sowie wörtliche oder sinngemäße Zitate als solche gekennzeichnet habe.

Jonathan Müller  
Karlsruhe, den 27. April 2015